Micro-PIXE for quantitative mapping of metal concentration in O. glaberrima and O. sativa riceplants

Laboratory of Tandetron

Alassane Alassane

Proposal ID

397

Multi-elemental analysis of roots and leaves from Oryza glaberrima rice plants at vegetative stage of growth by combined PIGE, RBS, PIXE and GC-TDS methods

S. Fernandes[a,*], A. Traoré[b], O. Fleury[b], V. Havránek[a], J. Kučera[a], A. Ndao[b]
[a]Nuclear Physics Institute CAS, v.v.i., 250 68, Husinec - Řež, Czech Republic
[b]Institute for Applied Nuclear Technology, Cheikh Anta Diop University, Dakar, Senegal

This study aims at understanding the bioaccumulation and transport mechanisms of both micro- and macronutrients in the leaves and roots of African rice *Oryza glaberrima* Steud (OG) plants cultivated in Senegal during the wet season at the vegetative stage of growth to determine the translocation factors from roots to leaves and to evaluate the suitability of OG rice plants for phytoremediation. A comparative analysis of the elemental composition of roots and leaves of OG plants, provided information on the bioaccumulation of nutrients necessary for plant growth which can become detrimental if their toxicity level is reached. The elemental analysis of basic nutrients (C, H, O), macronutrients (N, P, K, Ca, Mg and S) and micronutrients (Cl, Fe, Cu, Mn, Ni and Zn) in the OG roots and leaves was made possible by several elemental analytical techniques (PIGE, RBS, PIXE and GC-TDS). All methods were validated by analysis of pure substances and certified reference materials. The high accumulation rate of Cu (5 x), Al (4 x) and Fe (~ 2 x) in the OG rice roots relative to the leaves indicates the existence of low translocation factors for these metals from root to leaves probably due to the existence of plant mechanisms to limit their transport and to preferentially accumulate Si (% mass: 5.2 ± 0.5) in the rice leaves. The high accumulation rates of Mn, Ni, Rb and Cr "heavy" metals in the OG leaves relative to the roots, shows that these can be partially removed from soil through phytoextraction processes by harvesting the shoot tissues.

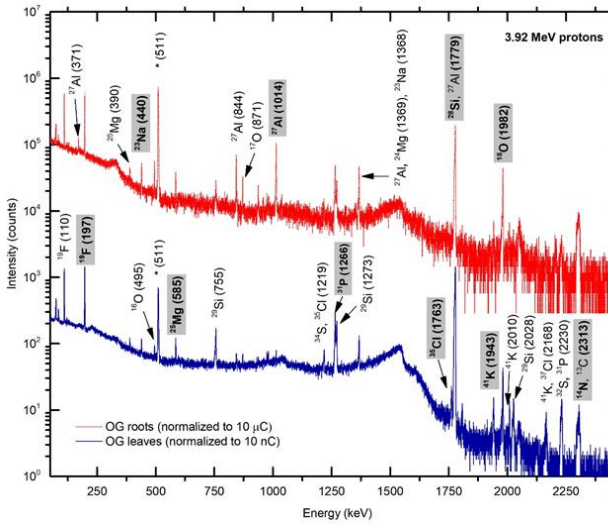

Figure 2 Normalized γ-ray spectrum for OG leaves and roots at 3.92 MeV protons. The γ-energy reference peak used for isotopic quantification is indicated inside grey boxes and highlighted in bold

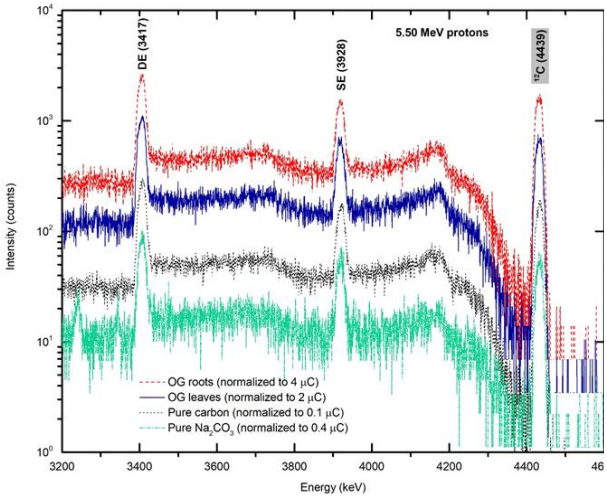

Figure 1 Detail of the normalized γ-ray spectrum of OG leaves and roots, and standard materials C and Na_2CO_3 at 5.5 MeV protons showing the reaction $^{12}C(p,p_1\gamma)^{12}C$ at 4439 keV and its single and double escape peaks.

The determination of the elemental composition of cultivated soil and OG rice stems and grains is necessary to obtain the translocation factors of nutrient and non-nutrient into different plant organs from soil to root and from leaves to grains for characterization of their transport into the plant cells. The analysis of the OG rice grains is needed to testify that all the potential toxic elements identified in this study, and other heavy metals such as As, Sb, Cd, Hg and Pb, known to be absorbed by the plant biomass, were not accumulated to toxic levels for human consumption to ensure food security in West Africa.

[1] S. Bado et al. NIM B 371 (2016) 407 - 412.

Target matrices for high-yield production of selected atomic and molecular ions

Laboratory of Tandetron

Mojmír Nmec

Proposal ID

404

Report regarding proposal: Target matrices for high-yield production of selected atomic and molecular ions

K. Fenclová, M. Bilous, T. Prášek, M. Němec, CTU in Prague – FNSPE, Czech Republic
J. Tecl, M. Klímová, J. Kučera, Nuclear Physics Institute, Řež, Czech Republic

Experiments on Tandetron were focused on fluoride matrices suitable for production of high-yield ion beams and with potential use in accelerator mass spectrometry. After screening of suitable materials, production of aluminium beam and ion forms created in the ion source were of major interest. Analysis was performed using low energy (LE) side of the ion beam line, where LE magnet and adjacent Faraday cup were used as mass spectrometer. Two fundamental materials were used - Na_3AlF_6 for production of fluoride molecular beams and Al_2O_3 as a reference oxide compound. Several crystallographic modifications of these compounds, defined by the way of preparation and subsequent heat treatment, were mixed with various compatible modifiers such as CaF_2, PbF_2, TiO_2, Cu, Ag, W powders in Cu and Ag target holders. In the ion source, two temperatures of Cs reservoir were used during target sputtering – 30 °C for the fluoride samples and 70 °C for the oxides. Selected peaks were additionally analysed using high energy (HE) part of the beam line to resolve possible isobaric interferences.

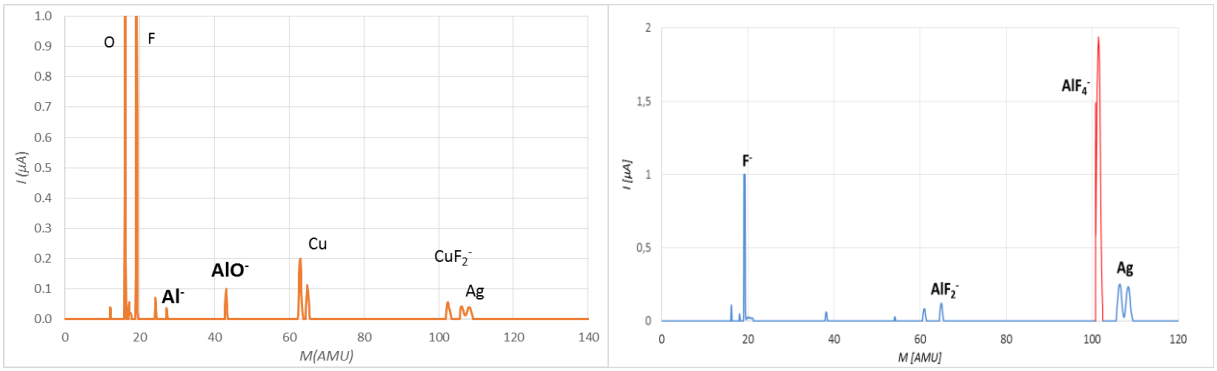

Fig. 1: LE mass spectra of (a) Al_2O_3 mixed with Ag powder in copper target holder at 70 °C of Cs reservoir *(F^- peak is a residuum from previous experiments with fluoride matrices)*, (b) Na_3AlF_6 mixed with PbF_2 in Ag target at 30 °C of Cs reservoir; both at 2 kV target voltage.

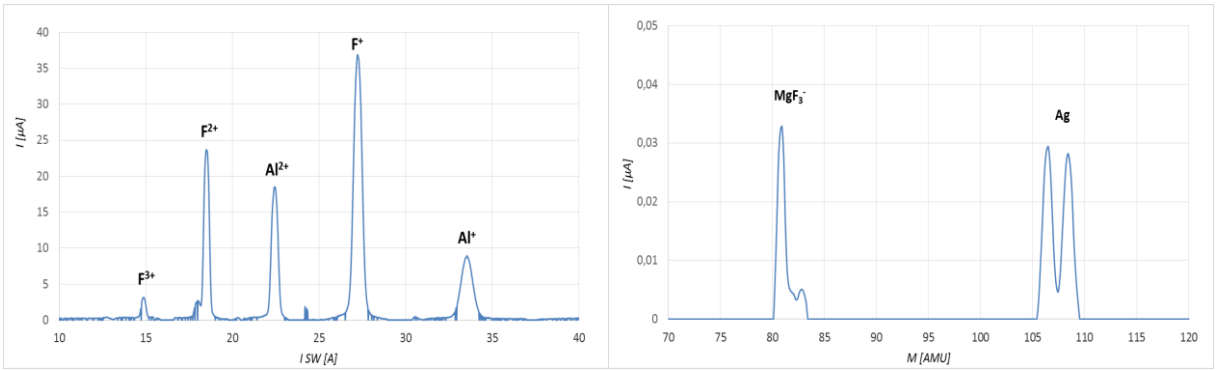

Fig. 2: (a) HE spectrum of Na_3AlF_6 + MgF_2 mixed with PbF_2 and Ag (1:1:1), (b) LE spectrum of MgF_2 in Ag target holder, both at 30°C of Cs reservoir and 2 kV target voltage.

The results show high potential of fluoride matrices for production of aluminium beams – when comparing standard Al^- with newly produced AlF_4^- beams, the latter provides approx. 10 – 40 times higher currents before entering the accelerator. In addition, no isobaric MgF_4^- was detected at both LE and HE side, indicating potential use of $^{26}AlF_4^-$ in AMS analyses and production of high intensity Al ion beam without isobaric contamination. Practically no significant influence of Al_2O_3 preparation procedure on Al^- or AlO^- ion beam intensity was found; in addition $Co(AlO_2)_2$ + Ag (1:2) provided interesting currents of high purity Co^- and Ag^- beams suitable for ion beam applications.

Characterization of Residual Stresses Distribution in Thick Welded Sheets for High-pressure Vessels

Neutron Physics Laboratory - Neutron diffraction

Karel Trojan

Proposal ID

405

Report regarding proposal "Characterization of RS Distribution in Thick Welded Sheets for High-pressure Vessels after LASER Welding"

K. Trojan[1*], Ch. Hervoches[2], A. Vlk[1], J. Čapek[1], N. Ganev[1]

[1]Department of Solid State Engineering, Faculty of Nuclear Sciences and Physical Engineering, Czech Technical University in Prague

[2] Nuclear Physics Institute, ASCR, v.v.i., Department of Neutron Physics, 25068 Řež, Czech Republic

*karel.trojan@fjfi.cvut.cz

It was found from the residual stresses (RSs) determined by neutron diffraction in three different sample orientations and in three different depths under the surface (see Fig. 1), that the greatest gradient of RSs is in the direction parallel to the weld (L – longitudinal direction) for both 8 and 10 mm thick plates. Moreover, the RSs in the longitudinal direction have a tensile character. On the other hand, the character of the RSs in the normal and transversal direction is more or less compressive.

The next step in this research is going to be determination of the RSs, using X-ray diffraction, in the same depths as in the case of the neutron diffraction. Comparison of results of these two methods will be made.

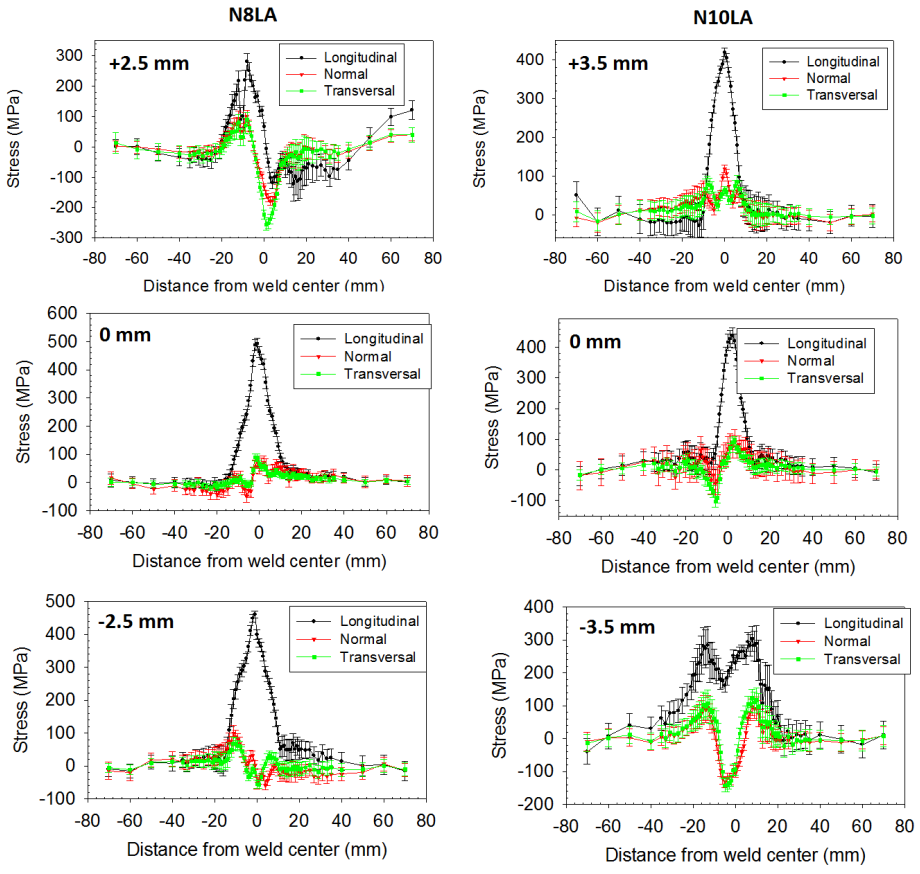

Figure 1: RSs for laser welded samples along three measured lines obtained by neutron diffraction.

Acknowledgement

Measurements were carried out at the CANAM infrastructure of the NPI CAS Řež supported through MEYS project No. LM2015056. This work was supported by the project TH02010664 of the Technology Agency of the Czech Republic and the Grant Agency of the Czech Technical University in Prague, grant No. SGS16/245/OHK4/3T/14.

RBS/ERDA measurements of X-B-C coatings

Laboratory of Tandetron

Petr Vašina

Proposal ID

406

Charakterizace W(TA, Mo)-B-C vrstev metodou RBS

V **Tabulce 1** se nalézají výsledky uvedené v atomárních procentech. V prvním sloupci je nazev zkoumaného vzorku, v ostatních sloupcích jsou koncentrace jednotlivých prvků uvedené v atomárních procentech, v posledním sloupci se nalézá tloušťka v atomech na cm^2.

Sample	Concetration [at.%]							Substrate	Thickness [10^{15}at/cm^2]
	Mo	W	Ta	B	C	O	Ar		
WBC100	-	25	-	19	44	2	10	Si	16900
WBC103	-	24	-	19	45	2	10	Si	14000
WBC106	-	48	-	17	21	2	12	C	19500
WBC107	-	50	-	18	21	2	9	C	21800
WBC108	-	56	-	16	18	2	8	C	17300
WBC109	-	48	-	19	21	2	10	C	24100
WBC116	-	52	-	17	21	2	8	C	21500
WBC117	-	51	-	19	20	2	8	C	21700
WBC118	-	50	-	20	21	2	9	C	22900
WBC119	-	-	-	-	-	-	-	Si	-
WBC120	-	48	-	23	17	2	10	C	47000
WD13	-	49	-	18	22	2	9	C	21500
WD23	-	31	-	34	22	2	11	C	23100
WA2	-	50	-	10	25	3	12	Si	21100
WA8	-	39	-	20	26	3	12	Si	12000
WB5	-	57	-	10	20	3	10	Si	20000
WB15	-	38	-	20	27	3	12	Si	6500
18E	-	-	25	16	31	12	15	C	2150
9cF	-	-	55	12	18	5	10	c	7300
15E(10E)	-	-	38	14	23	12	13	C	2250
13cF	-	-	-	-	-	-	-	C	-
19cF	-	-	56	12	17	5	10	C	6100
15cG	-	-	18	17	40	15	10	C	2480
10cG	-	-	19	13	46	12	9	C	3000
19cG	-	-	21	17	42	14	8	C	2500
10cH	-	-	16	18	42	12	12	C	4480
19cH	-	-	15	21	38	13	13	C	1850
15cH	-	-	17	20	38	13	12	C	3800
Mobc22	50.5	-	-	24	24.5	>1	-		13000
Mobc36	54.5	-	-	25	19.5	>1	-		13400

Tabulka 1: Přehled složení vzorků v atomárních procentech.

Závěr

Metodou RBS byly zjišťovány koncentrace prvků W(TA, Mo), B, C ve vrstvách na různých substátech. Také byla stanovena míra kontaminace prvky Ar a O. Některé vrstvy byly značně poškozené (Tabulka 1 – žlutě) a nebylo možné stanovit složení vrstvy. Část vzorků měla jen slabě poškozenou vrstvu (Tabulka 1 – šedivě) a domníváme se, že složení vrstev je ve zmíněných atomárních procentech.

Functional organic-inorganic nanostructures

Laboratory of Tandetron

Vladimir Cech

Proposal ID

410

Report on the project "Functional organic-inorganic nanostructures"

V. Cech, Inst. Mater. Chem., Brno Univ. Technol., Brno, Czech Republic
A. Romanenko, A. Mackova, Nucl. Physics Inst., Rez, Czech Republic

Hydrogenated amorphous carbon-silicon (a-CSi:H) films and hydrogenated amorphous carbon-silicon oxide (a-CSiO:H) films were deposited from pure tetravinylsilane (TVS) precursor or TVS mixed with argon or oxygen gases on silicon wafers or glassy carbons using plasma-enhance chemical vapor deposition (PECVD) in pulsed regime. The tough a-CSi:H films with lower hydrogen concentration (~ 24 at.%) and higher density (~ 2.0 g cm^{-3}) were deposited from TVS/Ar mixture at higher powers (> 25 W), see Fig. 1.

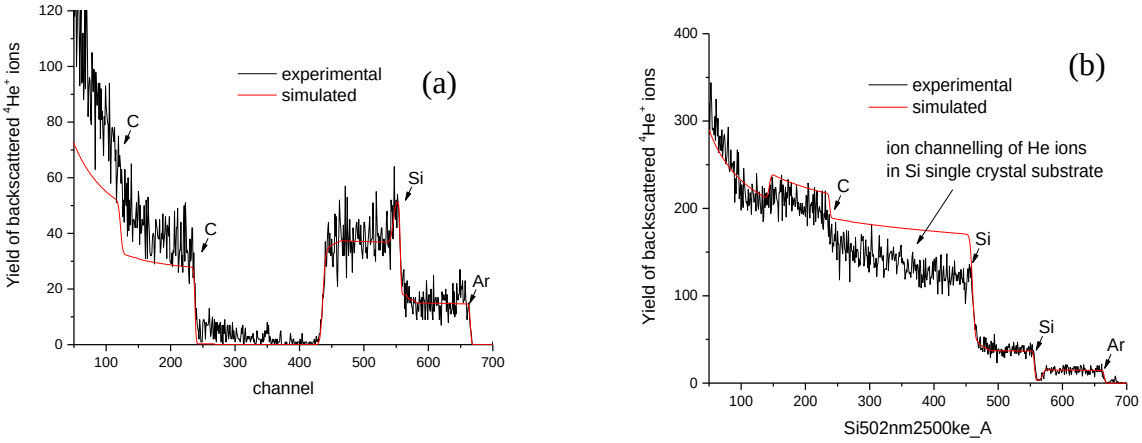

Fig. 1. RBS spectra of tough a-CSi:H films on (a) glassy carbon and (b) silicon wafer.

The RBS/ERDA analysis of polymer-like a-CSi:H films prepared from pure TVS allowed to show a higher hydrogen concentration (~ 58 at.%) and a lower density (~ 1.4 g cm^{-3}) of the material. While, a-CSiO:H films deposited from TVS/O_2 mixture were low hydrogenated materials (~ 7 at.%) with a density of 2.2 g cm^{-3}. The combination of the tough a-CSi:H material with the inorganic a-SiO:H material resulted in a bilayer structure, which was successfully analyzed (Fig. 2), and this type of organic-inorganic structures will continue to be developed and analyzed.

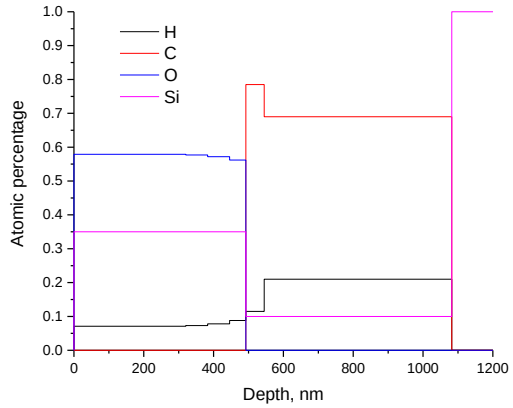

Fig. 2. Depth profile of element composition across the bilayer on silicon wafer.

Trace element fingerprints and chemical discrimination of neolithic stone industry source rocks

Neutron Physics Laboratory - Nuclear analytical methods with neutrons

Kristýna Trnová

Proposal ID

415

Report regarding proposal "Trace element fingerprints and chemical discrimination of neolithic stone industry source rocks"

K. Trnová, L. Veverka, P. Gadas, A. Přichystal, Masaryk University Brno, V. Strunga, Nucl. Physics Inst., Rez, Czech Republic

Partially or fully fabricated tools found in Holasky neolithic settlement with proven source in Želešice amphibolite body in Brno metabasite zone and Isera Mountains have been collected as well as other proven and potential source rocks have been collected. Powdered specimens of each have been prepared, irradiated and analyzed by INAA method.

Geochemical faetures have been studied using elemental ratio plots. The NAA results were also used for corrections and calibrations in XRF studies.

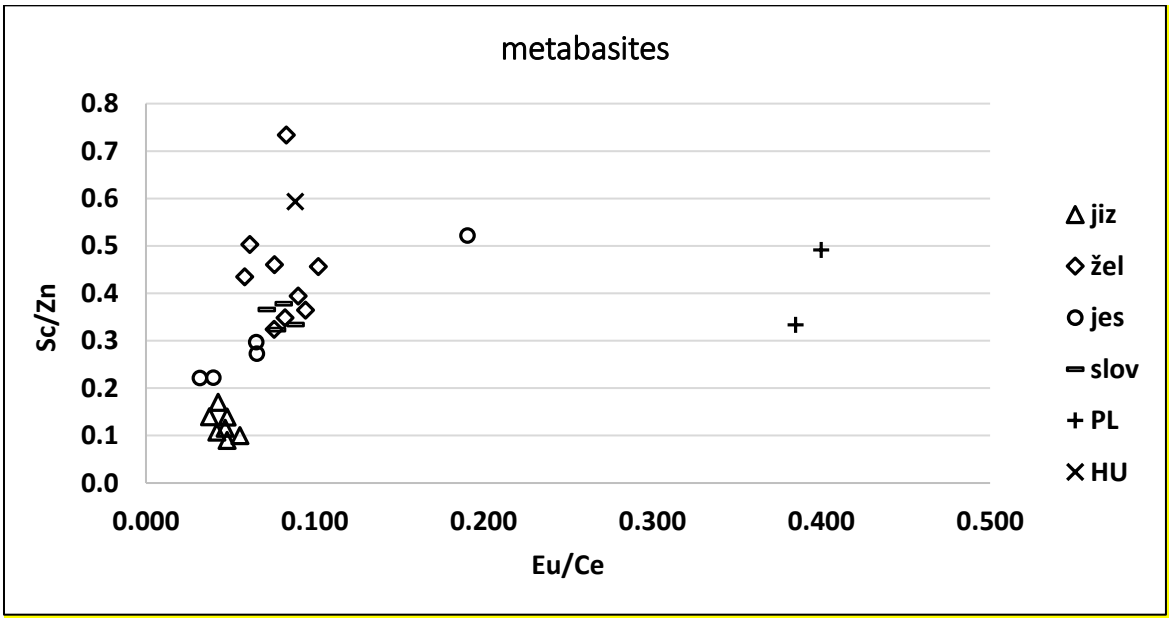

Fig. 1 An example of elemental ratios plot used for discrimination.

Statistical processing of data is performed for further advance in the study and scientific paper on the neutron activation analysis as a tool for discrimination studies of neolithic metabasite industry is in progress.
The results and improved XRF measurements are being used for two doctoral students participating as proposers of the project.

Early results have been presented at the seminar Radioanalytical Methods IAA 2019 on Juny 25th 2019, Faculty of Nuclear Sciences and Physical Engineering, Prague.

Reference

Robert J. Speakman, Nicole C. Little , Darrell Creel, Myles R. Miller , Javier G. Iñañez (2011) Sourcing ceramics with portable XRF spectrometers? A comparison with INAA using Mimbres pottery from the American Southwest. Journal of Archaeological Science, 38, 3483-3496.

197(m)Hg production via the 197Au(d,2n)197Hg reaction

Laboratory of Cyclotron and Fast Neutron Generators

Martin Walther

Proposal ID

293

Report regarding proposal "$^{197(m)}$Hg production via the ^{197}Au(d,2n) reaction"

M. Walther, Helmholtz-Zentrum Dresden-Rossendorf, Institute of Radiopharmaceutical Cancer Research, Germany

O. Lebeda, Nuclear Physics Institute of the CAS, Řež, Czech Republic

The significant larger cross-sections reported for ^{197}Au(d,2n)$^{197(m)}$Hg reaction [1] compared to the proton induced ^{197}Au(p,n)$^{197(m)}$Hg reaction could be unambiguously confirmed. With a deuteron beam energy of 16 MeV more than four times higher yields of the metastable no-carrier-added ^{197m}Hg radionuclide were accessible using comparable beam intensity. Thus it is shown clearly that the limiting factor of the low yield proton based reaction can be overcome using this alternative nuclear reaction. The additional advantage of the higher ratio of the preferable short-lived ^{197m}Hg radionuclide (ratio ^{197m}Hg/^{197}Hg: ~1.7/1) compared to the proton accessible product (~1/1) [2] also increases the attractiveness of this production route for potential theranostic application.

TABLE 1. Hg and Au isotopes after proton or deuteron irradiation of gold in the target solution and product solution after separation using LN resin

	E particle	t_{irr}	I_T	m_{Au}	A_{EOB} [MBq] in target solution				A_{EOB} [MBq] in product				yield
No		[min]	[µA]	[mg]	^{197}Hg	^{197m}Hg	^{196}Au	^{198}Au	^{197}Hg	^{197m}Hg	^{196}Au	^{198}Au	
1	10 MeV p	120	25	185	81	89	0.004	0.099	75	83	<0.001	<0.001	93%
2	12 MeV p	145	20	186	145	160	0.021	0.184	136	150	<0.001	0.002	94%
3	16 MeV d	120	11	186	272	462	7	156	248	420	<0.003	<0.003	91%
4	16 MeV d	150	10	186	332	574	9	193	315	545	<0.006	<0.003	95%

Beside the higher product yield during deuteron irradiation, also the significant formation of gold isotopes as undesired side products must be considered in the workup procedure. Therefore, according to the high requirements, a new resin based Hg/Au separation method was developed. So called LN resin (LaNthanides)[3,4], was successfully tested for this application. The obtained promising results in radionuclide production together with results of labeling - and biological experiments will be published as soon as possible in the current year in peer-reviewed international journals.

References

[1] F. Tárkányi, F. Ditrói, A. Hermanne, S. Takács, B. Király, H. Yamazaki, M. Baba, A. Mohammadi, A.V. Ignatyuk, Nucl. Instrum. Methods Phys. Res., Sect. B 269, pp. 1389–1400, 2011.

[2] M. Walther, S. Preusche, S. Bartel, G. Wunderlich, R. Freudenberg, J. Steinbach, H.-J. Pietzsch: Appl. Radiat. Isot. 97, pp. 177–181, 2015

[3] E. P. Horwitz, C. A. Bloomquist, Journal of Inorganic Nuclear Chemistry, 37, pp. 425–434 1975.

[4] D. McAlister, E. P. Horwitz, Solvent Extraction and Ion Exchange, 25, (6), pp. 757–769 2007.

Investigation of irradiation induced defects in new materials for nuclear reactors: Zr, Ti based al

Laboratory of Tandetron

Jakub Cizek

Proposal ID

423

Investigation of irradiation induced defects in new materials for nuclear reactors: Zr, Ti based al – Final report

Several alloys consisting of refractory metal elements Hf, Nb, Ta, Ti, Zr have been prepared by arc melt casting. The chemical composition and basic properties of samples studied are summarized in Table 1. The alloys were irradiated with 2.9 MeV protons at room temperature using a Tandetron accelerator. Annealing was performed in several steps with fluence gradually increasing from 10^{15} to 10^{16} cm^{-2}. The samples were investigated after each irradiation step in order to study the development of irradiation-induced defects with increasing fluence.

Table 1 *List of refractory metal alloys studied in the present work. The table shows the composition of each alloy; atom misfit parameter (δ) representing a measure of the magnitude of lattice distortions; configurational entropy of random solid solution (S^{SS}); results of tensile test with constant strain rate of 2×10^{-4} s^{-1}: yield strength (YS), ultimate tensile strength (UTS) and elongation-to-failure (A_{max}); Vickers hardness (HV) measured using load of 0.5 kg applied for 10 s; and the average cross-section for absorption of epithermal neutrons (σ).*

composition	δ (%)	S^{SS} (R)	YS (MPa)	UTS (MPa)	A_{max} (%)	HV (GPa)	σ (barn)
NbTaTi	1.05	1.10	620	683	18.5	2.42 ± 0.02	9.3
NbTaTiZr	4.83	1.39	1144	1205	6.4	3.64 ± 0.02	7.0
$Nb_{0.5}TaTiZr_{1.5}$	5.22	1.32	-	843	0	4.80 ±0.03	6.9
HfNbTaTiZr	4.98	1.61	1155	1212	12.3	3.48 ± 0.03	23.3

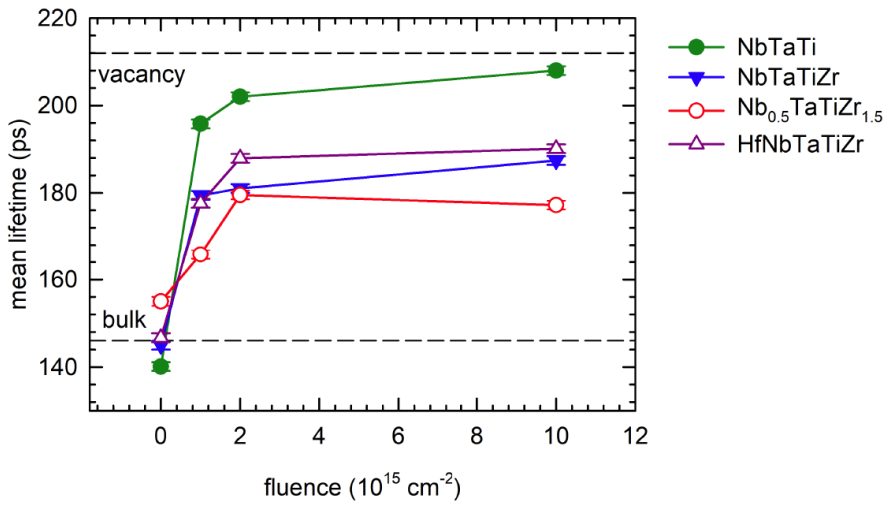

Figure 1 *The development of the mean positron lifetime of NbTaTi, NbTaTiZr, Nb0.5TaTiZr1.5 and HfNbTaTiZr alloy with the irradiation fluence.*

Fig. 1 shows the development of the mean positron lifetime with increasing irradiation fluence. The mean positron lifetime is a robust parameter which is only slightly affected by correlations between the fitting parameters. It is useful for observation of trends occurring during irradiation. The virgin samples exhibit single component LT spectra indicating that positrons are annihilated in single state. Virgin state of the alloys studied is characterized by the lifetime in the range 140-155 ps corresponding to the bulk lifetime, i.e. the lifetime of free positrons not trapped at defects. Hence, the concentration of defects in these alloys is very low and virtually all positrons are annihilated in the free state. Proton irradiation led to an increase of the mean positron lifetime due to formation of radiation-induced defects. The mean lifetime of all alloys increases with increasing fluence indicating that the concentration of irradiation-induced defects increases with increasing fluence. The most pronounced increase of the mean positron lifetime was observed for the NbTaTi alloy. For the highest fluence of 10^{16} cm^{-2} the mean lifetime approaches 210 ps corresponding to lifetime of positrons trapped in monovacancy testifying that majority of positrons is trapped in vacancies. The NbTaTiZr and HfNbTaTiZr alloys exhibit comparable increase of the mean positron lifetime but it is remarkably lower than that for the NbTaTi alloy. The lowest increase of the mean positron lifetime was observed in the $Nb_{0.5}TaTiZr_{1.5}$ alloy where the magnitude of lattice distortions is the highest among the alloys studied as reflected by the highest value of the misfit parameter δ, see Table 1.

Hence, the present investigations of refractory metal alloys irradiated by protons confirmed good radiation resistance of HEAs. It seems that good resistance against radiation damage is common property of 3d transition metal and refractory metal HEAs. Radiation resistance of HEAs is directly related to the effect of lattice distortions representing a typical feature of HEA structure.

Study of the fission process at higher neutron energies

Laboratory of Cyclotron and Fast Neutron Generators

David Hladík

Proposal ID

424

Final report regarding the proposal 'Study of the fission process at higher neutron energies'

Small samples of an ^{238}U were irradiated with quasi-monoenergetic neutrons from the cyclotron U-120M with p+^{7}Li and p+Be converter at several peak neutron energies in the range of 17-33 MeV and delayed neutrons (DN) were measured. BF_3 detectors were chosen for the measurement of time distribution of the DN.

New measurement process was developed and tested during several experiments. The goal was to minimize the effect of saturation of the detectors as well as measure even the shortest decay group below 0.5 s after the end of irradiation. This goal was successfully accomplished.

This result was presented at "Second French-Czech « Barrande » Nuclear Research Workshop" in France.

These results can serve as a proof of concept and the work will continue to acquire better precision. Subsequently, the simulation using General Fission Model (GEF) is in progress for further comparison of acquired data

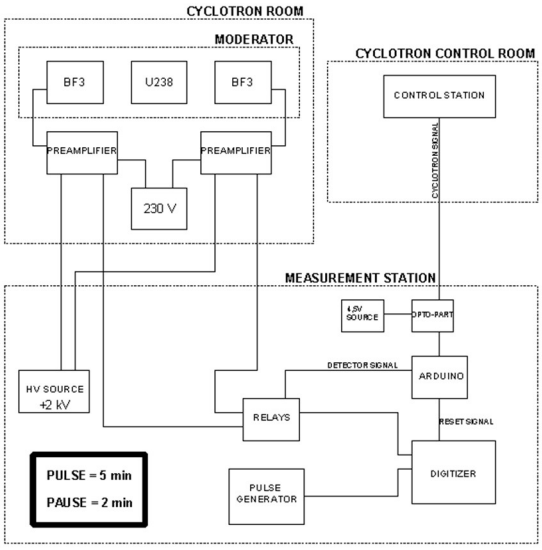

Figure 1. Block scheme of the measurement setting and process

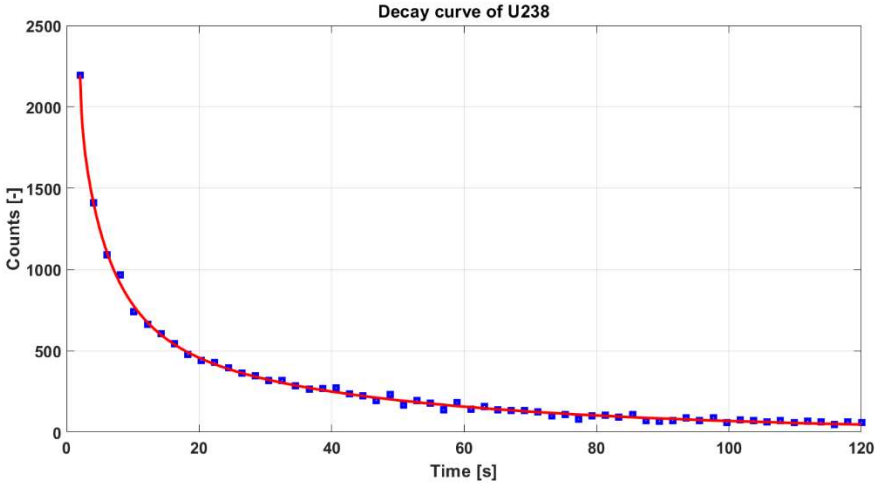

Figure 2. Decay curve obtained from an experiment using p+Be target, En=20 Mev, distance 1 m.

Systematic study on the strain free / independent lattice parameter D0 for multiphase materials subj

Neutron Physics Laboratory - Neutron diffraction

Samuel Pulvermacher

Proposal ID

425

Systematic study on the strain free / independent lattice parameter D_0 for multiphase materials

Samuel Pulvermacher (email: samuel.pulvermacher@kit.edu, Karlsruhe Institute of Technology)
Jan Šaroun (email: saroun@ujf.cas.cz, Ústav jaderné fyziky AV ČR, v. v. i.)
Jens Gibmeier (email: jens.gibmeier@kit.edu, Karlsruhe Institute of Technology)

Introduction:

Aim of the project is to develop a basic understanding on the effect of local phase-specific micro residual stresses on the determination of the strain independent lattice parameter D_0 and providing a basis for the reliable modelling of the surface effects for coarse multiphase materials and for materials states with chemical gradients in the near surface region. Corporately, a measuring and evaluation strategy for non-destructive analysis of near surface residual stress gradients for problematic material states will be developed. In the current research project fundamental investigations on the effect of phase-specific micro residual stresses on the reference value D_0 will be carried out. For this purpose, defined residual stress states will be applied for multiphase materials with variations in the phase contents. In the first approach various fine grained duplex steels will be studied, which clearly differ in the amount of the phase contents. Finally, based on the experimental results and the accompanying numerical simulations, recommendations for appropriate sample preparations for providing appropriate reference samples for multiphase materials will be provided.

Measurement setup:

In this first approach we focused on the investigation of duplex steel type X2CrNiMoN22-5-3 (1.4462) and X3CrNiMoN27-5-2 (1.4460), which hold a phase composition of about 50% ferrite and 50% austenite and 70/30 (for 1.4460) in the as received state.

In preparation of the beamtime defined uniaxial tensile tests were performed, so that total strains between 0 and 9% were realized. From this test series, small pins were sectioned using wire-cut EDM (electro discharge machining) for the loading states with 0, 2 and 9%. The sectioned pins had diameters of 2, 3, 4 and 5 mm to check if the remaining residual stress state is affected by the sample size. The respective orientation of the pin relative to the sample was noted in order to be able to take into account the loading axis and the potential texture influences. Each pin was measured in two directions, i.e. in axial and in radial = transverse direction.

Preliminary results

In both materials, 4 ferrite (α) and 5 austenite (γ) lattice planes were investigated. Peakshift due to sample misorientation were corrected using the program SIMRES. Figures 1 show an example of the phasespecific interplanar spacings for the duplex steel 1.4460 in longitudinal direction. The data allow for the comparison of lattice strain determined in specific sample orientations for pins of the same and varying sizes. The data indicate that the interplanar spacings are affected by micro-residual stresses that result from the uniaxial elasto-plastic deformation. However, rather large data scattering exist, which not least stem for the pin misorientation, which could only be corrected insufficiently. It is planned to re-measure the pins in a modified experimental setup to reduce misorientation effects and increase the stability of the results.
For this purpose, a new sample holder was designed and manufactured at KIT. In parallel, the Meredit experiment was rebuilt, i.e. the sample carousel was replaced by a linearly movable table to improve the sample alignment.

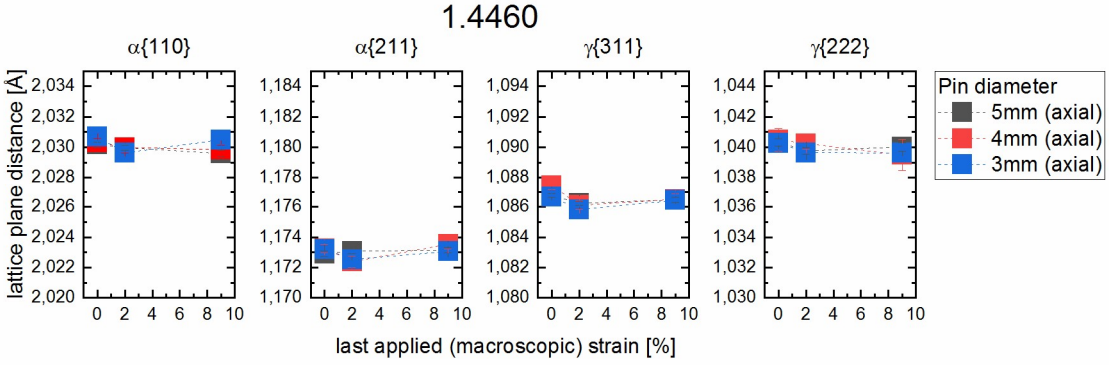

Figure 1: Examplary plot of the change of the phase-specific lattice plane distance with the degree of plastic deformation for the investigated duplex steel 1.4460

Calibration of TimePix detectors and low-energy proton radiography

Laboratory of Tandetron

Václav Olšanský

Proposal ID

426

Report regarding proposal "Calibration of TimePix detector and low-energy proton radiography"

V. Olšanský[1], C. Oancea[2], C. Granja[2], V. Havránek[1], A. Mackova[1], J. Jakůbek[2], Š. Polanský[2], P. Krist[1]

[1] *Nuclear Physics Institute Czech Acad. Sci., Řež, Czech Republic*

[2] *ADVACAM, Prague, Czech Republic*

The goal of these measurements was to perform proton radiography in the air and to characterize the proton and carbon micro-beams in vacuum. Several experimental setups were designed. Firstly, AdvaPix–TimePix3 and MiniPix–TimePix detectors with 300 µm thick Si sensors were calibrated in proton µ-beams and in a wide-area scanning beam. Afterwards, Al and Mylar targets (of various thicknesses from 5 to 30 µm) and more complex target stairs-like (thicknesses of 30, 25, 10, 5 and 0-air) of Al and Mylar, Fig. 1, were used to produce proton radiographies. All targets were placed close to the sensitive Si layer of detector, see Fig.1.

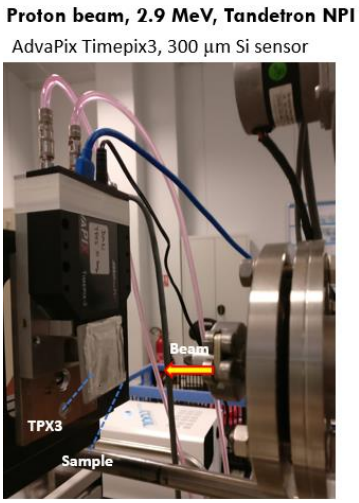

Figure 1 Experimental setup of a proton radiography using Advapix Timepi-3 detector.

The highly integrated signal electronics per-pixel provide fast and dark-current free single particle detection. The hybrid semiconductor pixel detector Timepix-3, Fig. 1, provides high-sensitivity and wide-dynamic range in terms of particle types, fluxes and spectral response. Timepix-3 detector visualizes the track of each individual particle and determines its time of interaction, spatial location and energy loss, see Fig. 2.

This experiment demonstrates the possibility of using low energy protons for radiography of very thin samples. Results have been visualized as images which show one of these distributions: cluster sizes, cluster energy and high. The reconstruction of proton radiography of Al stairs-like target can be seen in Fig. 3. Promising results were obtained based on the cluster area, Fig.3 b), and cluster energy, Fig. 3c). Further investigations of other targets are ongoing.

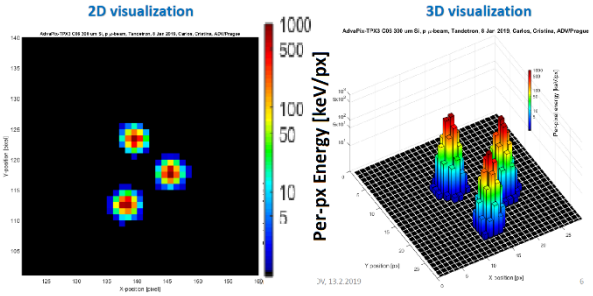

Figure 2 Position- and spectral-sensitive detection of single protons. a) 2D visualization and b) 3D visualization of per-pixel energy (displayed in color scale) of 3 events delivered in spot scanning beam mode [1].

<u>Vacuum measurements using ^{12}C scanning beams</u>

A Minipix Timepix detector was placed inside the vacuum chamber and the Time and spatial distribution of 10 MeV ^{12}C beam were studied. In Fig. 4 is sown the Time and spatial pattern of a scanning beam measured for 1 min. Other energies and scanning patterns were studied.

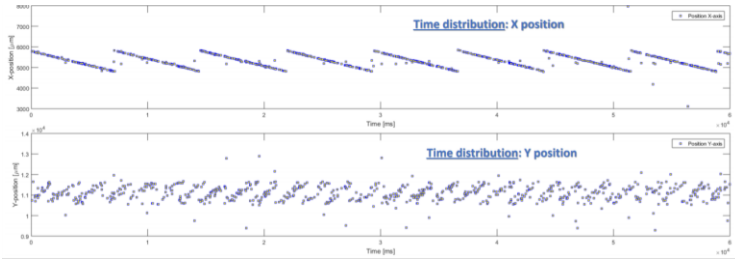

Figure 4 Time and spatial distribution of 10 MeV ^{12}C-ion beams.

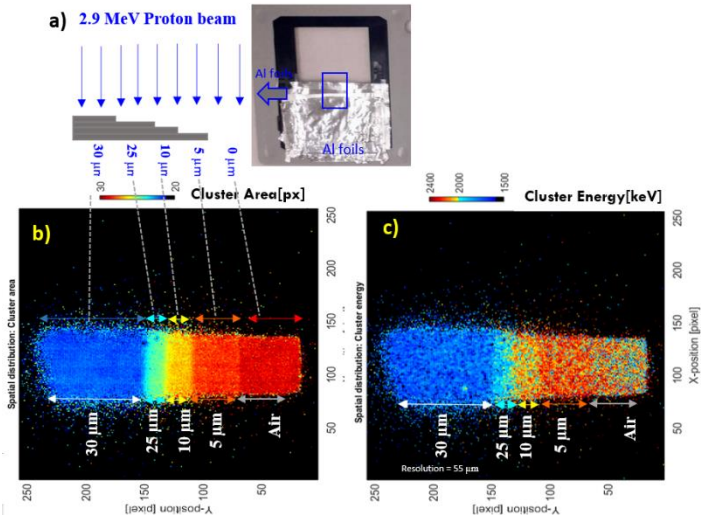

Figure 3 a) Al stair- like target, b) radiography reconstruction of the Al target using cluster area and c) reconstruction using the cluster energy.

Reference: C. Oancea, C. Granja, J. Jakubek, A. Mackova, V. Havranek, V. Olsansky *Charged particle imaging with Timepix a Timepix3 Pixel Detector*, 5th Annual LLU Workshop, USA 2019

In-situ V-SANS studies of WC grain growth in hard metals

Neutron Physics Laboratory - Neutron diffraction

Ahmet Bahadir Yildiz

Proposal ID

427

Experimental report

Proposal: In-situ V-SANS studies of WC grain growth in hard metals (ID: 427)

Ahmet Bahadir Yildiz, Peter Hedström: KTH Royal Institute of Technology, Stockholm

Beamline scientist: Vasyl Ryukhtin

The performance of a cemented carbide relies on the as-sintered composite microstructure consisting of the hard WC grains embedded in the ductile Co matrix. In order to tailor the properties of a cemented carbide, the understanding of the microstructure evolution concerning WC growth during the sintering has great importance. During our beamtime on the MAUD, we performed the first in-situ small angle scattering studies of cemented carbides. We studied WC grain growth as a function of the different type and amount of grain growth inhibitors, i.e. V and Ti, during the sintering at 1400 °C for 2 h using the high-temperature furnace. In order to eliminate the evaporation of Co, the furnace was filled by Ar. Due to the limited time, VSANS data were acquired only at high-resolution mode with 12 min intervals. However, this instrumental resolution was not sufficient to cover the desired Q-range to detect fine-grained WC especially at the beginning of the sintering.

Fig. 1 shows the VSANS curves of 0.15 wt.% Ti-doped sample. At the beginning of the sintering, VSANS curve consisted only of Porod-type scattering. On the other hand, due to the growth of WC, we observed a Guinier regime at the lower-Q region of VSANS curve after 2 h of sintering. Therefore, we would like to continue in-situ experiments with medium- and low-resolution modes to cover the entire size-range of WC grains. Furthermore, an oxide layer formation was observed on the sample surfaces (**Fig. 2**). We avoided such formation by trapping free O_2 inside the furnace using sacrificial Ti piece that, however, resulted in Co-layer formation (**Fig. 3**). We are currently working on possible solutions to avoid layer formation during the sintering.

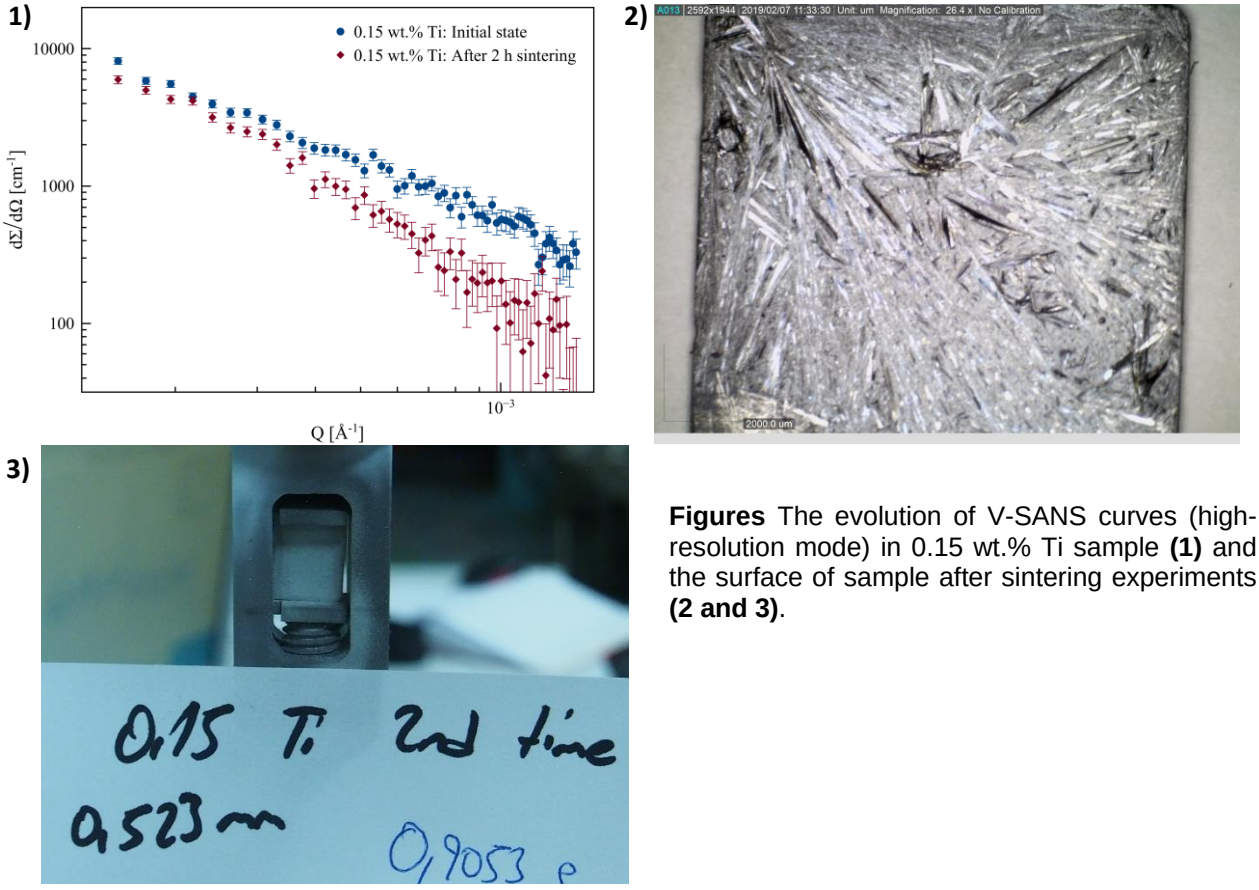

Figures The evolution of V-SANS curves (high-resolution mode) in 0.15 wt.% Ti sample **(1)** and the surface of sample after sintering experiments **(2 and 3)**.

Multielemental analysis of nutrients and pollutants in cultivated O. glaberrima and Sativa rices on

Neutron Physics Laboratory - Nuclear analytical methods with neutrons

Alassane Alassane

Proposal ID

428

Multi-elemental analysis of roots and leaves from Oryza glaberrima rice plants at vegetative stage of growth by combined PIGE, RBS, PIXE and GC-TDS methods

S. Fernandes[a,*], A. Traoré[b], O. Fleury[b], V. Havránek[a], J. Kučera[a], A. Ndao[b]
[a]Nuclear Physics Institute CAS, v.v.i., 250 68, Husinec - Řež, Czech Republic
[b]Institute for Applied Nuclear Technology, Cheikh Anta Diop University, Dakar, Senegal

This study aims at understanding the bioaccumulation and transport mechanisms of both micro- and macronutrients in the leaves and roots of African rice *Oryza glaberrima* Steud (OG) plants cultivated in Senegal during the wet season at the vegetative stage of growth to determine the translocation factors from roots to leaves and to evaluate the suitability of OG rice plants for phytoremediation. A comparative analysis of the elemental composition of roots and leaves of OG plants, provided information on the bioaccumulation of nutrients necessary for plant growth which can become detrimental if their toxicity level is reached. The elemental analysis of basic nutrients (C, H, O), macronutrients (N, P, K, Ca, Mg and S) and micronutrients (Cl, Fe, Cu, Mn, Ni and Zn) in the OG roots and leaves was made possible by several elemental analytical techniques (PIGE, RBS, PIXE and GC-TDS). All methods were validated by analysis of pure substances and certified reference materials. The high accumulation rate of Cu (5 x), Al (4 x) and Fe (~ 2 x) in the OG rice roots relative to the leaves indicates the existence of low translocation factors for these metals from root to leaves probably due to the existence of plant mechanisms to limit their transport and to preferentially accumulate Si (% mass: 5.2 ± 0.5) in the rice leaves. The high accumulation rates of Mn, Ni, Rb and Cr "heavy" metals in the OG leaves relative to the roots, shows that these can be partially removed from soil through phytoextraction processes by harvesting the shoot tissues.

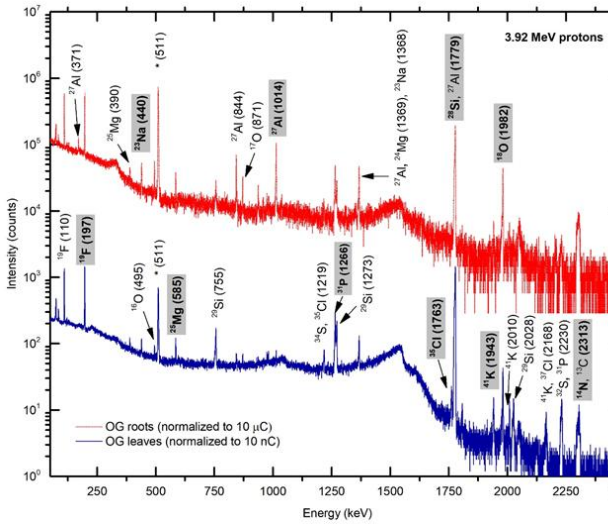

Figure 2 Normalized γ-ray spectrum for OG leaves and roots at 3.92 MeV protons. The γ-energy reference peak used for isotopic quantification is indicated inside grey boxes and highlighted in bold

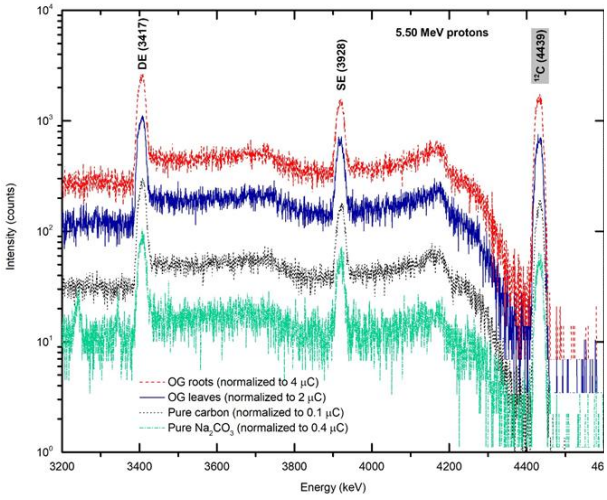

Figure 1 Detail of the normalized γ-ray spectrum of OG leaves and roots, and standard materials C and Na_2CO_3 at 5.5 MeV protons showing the reaction $^{12}C(p,p_1\gamma)^{12}C$ at 4439 keV and its single and double escape peaks.

The determination of the elemental composition of cultivated soil and OG rice stems and grains is necessary to obtain the translocation factors of nutrient and non-nutrient into different plant organs from soil to root and from leaves to grains for characterization of their transport into the plant cells. The analysis of the OG rice grains is needed to testify that all the potential toxic elements identified in this study, and other heavy metals such as As, Sb, Cd, Hg and Pb, known to be absorbed by the plant biomass, were not accumulated to toxic levels for human consumption to ensure food security in West Africa.

[1] S. Bado et al. NIM B 371 (2016) 407 - 412.

SINE2020 feasibility study - Determination of bulk residual stress in cold winding springs

Neutron Physics Laboratory - Neutron diffraction

Pavel Strunz

Proposal ID

433

Determination of difference bulk residual strains/stresses profile in cold winding springs and corresponding quenched/tempered wires

In order to fully understand **influence of the bulk residual strains/stresses** developed in steel spring from quenched/tempered ultrahigh strength wire (UTS is around 2000 MPa) after different cold forming/coiling processes followed by various stress relieving annealing **on the safe service life and final mechanical properties** characterized by fatigue strength, it is important to performed non-destructive Strain/Stress analysis by Neutron Diffraction on real Springs.

Two cold-winding springs, denoted “spring A” and “spring B” were scanned at the SPN-100 neutron diffractometer. They correspond to two different technological procedures used for their productions. Rods for d_0 (“stress-free”) determination were measured as well.

A suitable neutron wavelength λ = 2.13 Å and reflection from the examined material [α-Fe (110), lattice spacing a = 2.865 Å] were selected to reach the diffraction angle 2θ near 65°. This is not the geometrically optimum diffraction arrangement. Nevertheless, it ensures low background at the position-sensitive detector and the gauge volume is still of not too much of anisometric shape in this case. The strain (stress) determined in the diffraction experiment was averaged over the gauge volume of 2x2x2 mm^3. In order to determine three stress components, the different geometrical arrangement of the examined specimen with respect to the scattering vector were realized. The necessary configurations are shown in Fig. 1.

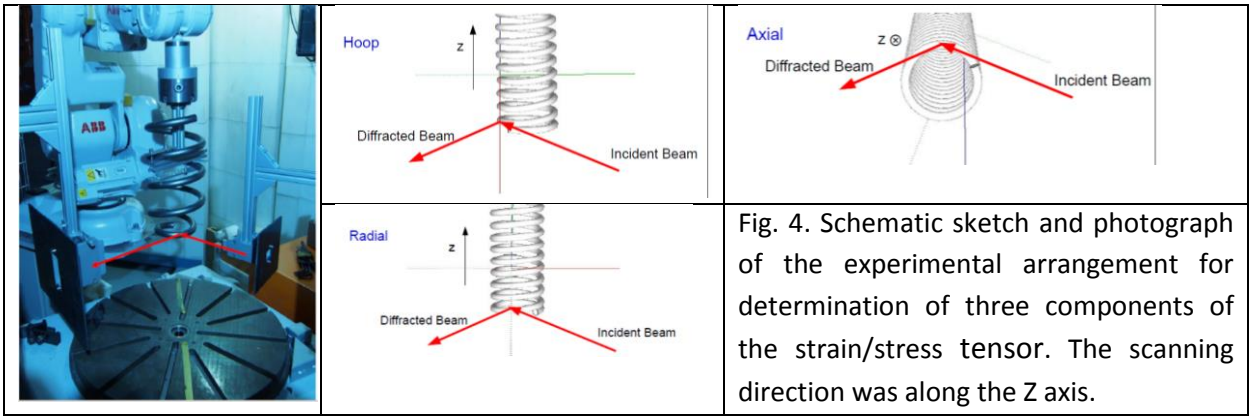

Fig. 4. Schematic sketch and photograph of the experimental arrangement for determination of three components of the strain/stress tensor. The scanning direction was along the Z axis.

The strains measured during through-wire scans are drawn in Fig. 5. For some components of the strain tensor, it was, however, not possible to obtain reasonable results due to attenuation in rather complex shape (spring).

It was found that it is possible to measure residual elastic strains in cold winding springs. The lattice strains were determined along two scans in two different springs. Three points should be, nevertheless, considered for possible further measurements:

1) Other scanning direction should be selected as the gradient of the effect of residual stress should be largest in in-out direction from the spring centre (i.e. not along Z direction).
2) Specimens are of a complex shape. Therefore, some points are hardly measurable in some geometries; consider use of alternative geometry of measurement or stronger neutron source.
3) Notation of direction should be with respect to wire axis, not with respect to spring axis, as these directions are in fact of largest interest for the producer.

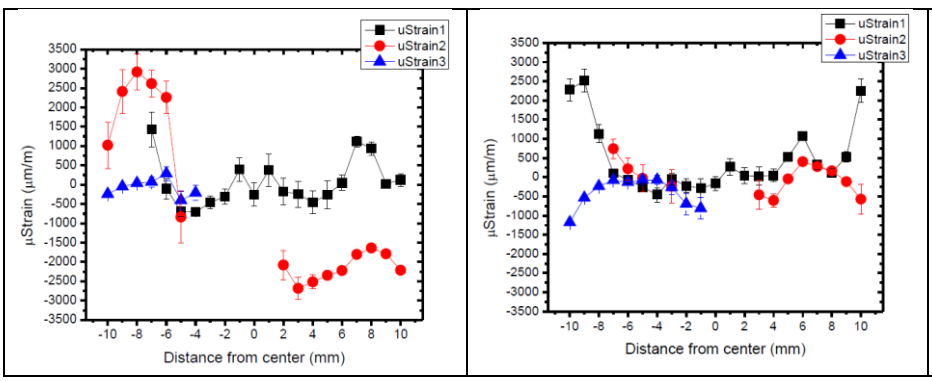

Fig. 5. Determination of the elastic strain in “spring A” (left) and “spring B” (right) springs. The notation used is: Radial = “uStrain1”, Hoop = “uStrain2”, Axial = “uStrain3”.

Detector proton and ion response characterization for field measurements in hadron radiotherapy

Laboratory of Cyclotron and Fast Neutron Generators

Olivier Van Hoey

Proposal ID

435

Detector proton and ion response characterization for field measurements in hadron radiotherapy

Racell Nabha[1], Olivier Van Hoey[1], Cristina Oancea[2], Carlos Granja[2,3]
[1]*Belgian Nuclear Research Center (SCK-CEN), Mol, Belgium*
[2]*Advacam, Prague, Czech Republic*
[3]*Nuclear Physics Institute, Czech Academy of Sciences, Prague, Czech Republic*

Accurate characterization of the radiation field in hadron therapy is an essential step towards unraveling the radiation-induced biological effects. The MiniPIX detector is suitable for this purpose but needs to be fully characterized. The purpose of these irradiations was to test and characterize the response of our MiniPIX detector and further optimize our data processing methods and algorithms. Figure 1 shows the deposited energy and LET spectra in the detector using 31 MeV and 22 MeV proton beams during a rotation scan. Protons of lower energy (12 MeV) and other angles were also tested, but are not shown here.

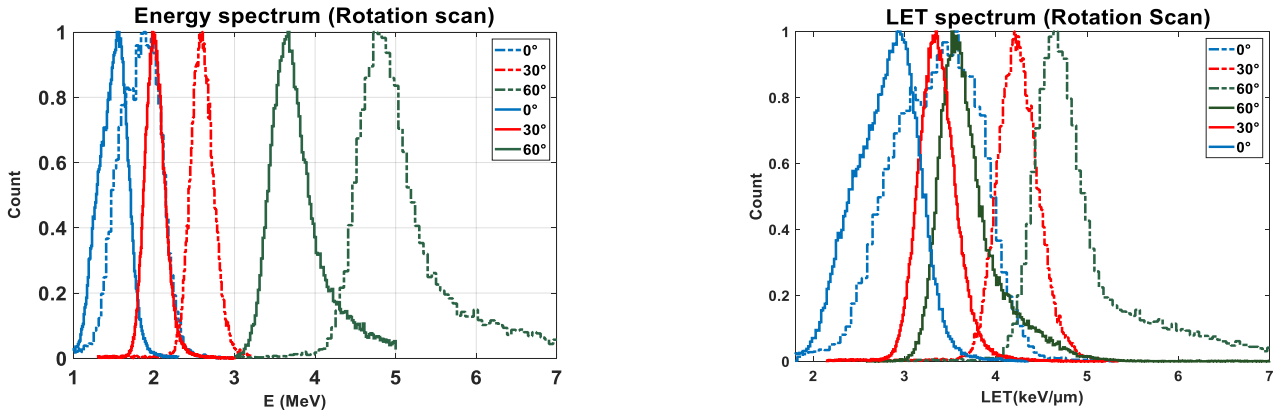

Figure 1. Deposited energy spectra (left) and LET spectra (right) for 31 MeV (solid line) 22 MeV (dashed) proton beams.

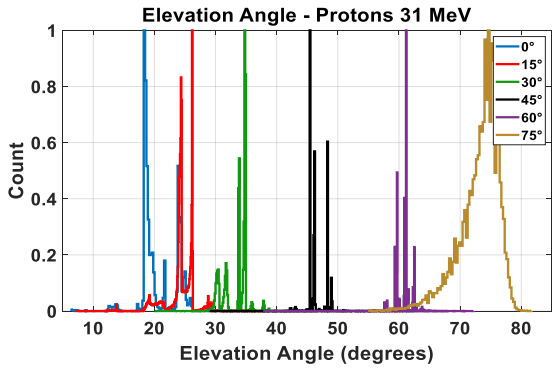

Figure 3. Reconstructed incident angle using track length and morphology.

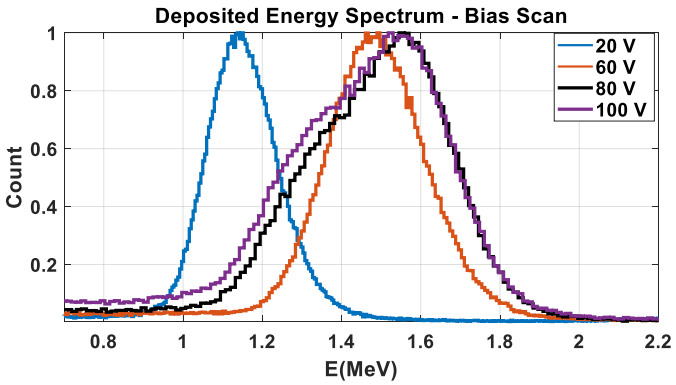

Figure 2. Energy deposition distribution for 31 MeV protons using different sensor bias at 0º incident angle.

Each particle hitting the pixelated detector will generate charge carriers along its track. Using the deposited energy and track length, the elevation angle of the incident particle can be reconstructed (figure 2). The charge sharing effect which spreads the deposited charge into adjacent pixels, depends on the sensor bias and therefore on the depleted volume. In the second part of this experiment, a bias scan was performed whereby the detector was irradiated with 31 MeV protons at the same angle and using different bias values (figure 3).

Beyond 80 V, saturation effects can be seen and signals can become strongly distorted. For our 500 um Si detector, keeping the bias at 80 V for such operations and exposures maintains the depleted volume and the charge sharing effect which lowers the per-pixel deposited charge. Monte Carlo simulations to compare and validate the results of the measurements are currently being performed.

MiniPIX neutron response characterisation for field measurements in hadron radiotherapy

Laboratory of Cyclotron and Fast Neutron Generators

Olivier Van Hoey

Proposal ID

436

MiniPIX neutron response characterization for field measurements in hadron radiotherapy

Racell Nabha[1], Olivier Van Hoey[1], Cristina Oancea[2], Carlos Granja[2,3]
[1]*Belgian Nuclear Research Center (SCK-CEN), Mol, Belgium*
[2]*Advacam, Prague, Czech Republic*
[3]*Nuclear Physics Institute, Czech Academy of Sciences, Prague, Czech Republic*

Despite the promising physical advantages of proton therapy, the dose deposited out-of-field is still unavoidable. This dose is associated with potential late effects including secondary cancers. Various particles (e.g. neutrons, photons, secondary protons, heavier ions and fragments) contribute to this dose with a wide range of physical properties and with the highest contribution coming from neutrons. The uncertainty in identifying, discriminating and characterizing these particles needs to be addressed in order to accurately estimate the physical dose delivered to normal tissues. Part of characterizing our MiniPIX detector for proton therapy applications requires assessing its response with neutrons and mixed fields.

Two sets of experiments were done during neutron irradiations. In the first one, two MiniPIX detectors (G01-500 µm Si, and I10-300 µm Si) were placed along the beam axis with different neutron converters. A neutron shield made of six PMMA targets and two aluminum targets was placed in between the detectors on a motorized shifter such that for each measurement, the beam axis, the two detectors and one of targets will be aligned. The setup is shown in figure 1a. In the second part, the PMMA and Al targets remained in place, and the two detectors were placed below the plane of the beam and 66 cm off axis , with one rotating detector and one fixed detector. The setup is shown in figure 1b.

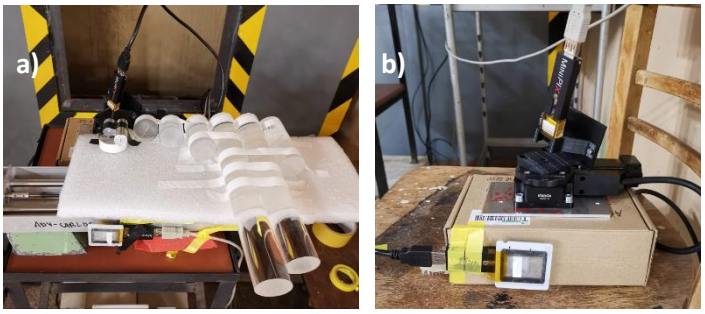

Figure 1. Setup (a) of part 1 shows MiniPIX G01 placed behind the shield and MiniPIX I10 placed in front of the shield. Setup (2) of part 2 of neutron irradiations in which G01 was rotating and I10 was fixed.

Preliminary data analysis for G01 detector shows that the total energy deposited in the detector did not significantly vary from one position (i.e. PMMA target) to the other (figure 2a). Protons having slowed down reach G01 with lower energy and hence deposit higher energy in the detector. Figure 2b shows the deposited energy spectra of recoiled protons in detector G01 compared with I10. The total number of events from recoiled protons was also reduced by a factor of 3 using the first PMMA target.

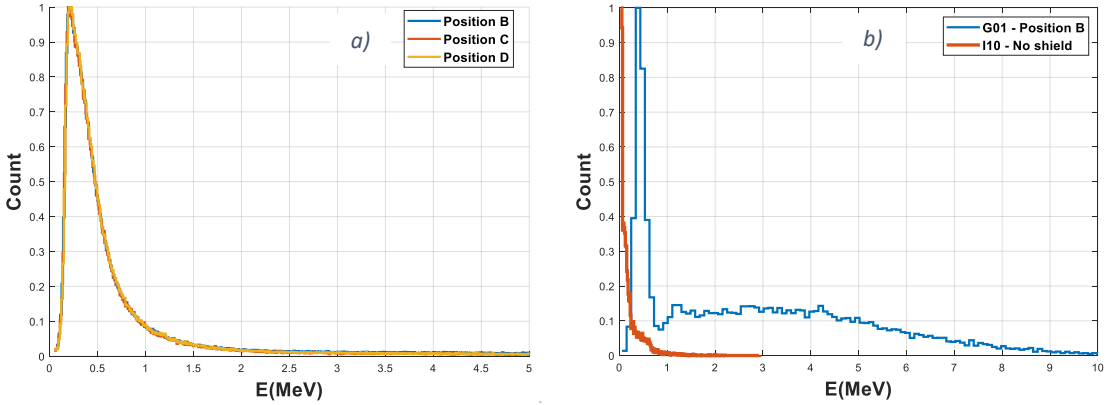

Figure 2. a) Total deposited energy spectra in G01 at 3 different positions behind the PMMA targets, and b) deposited energy spectra from recoiled protons in G01 (shielded) and I10 (unshielded).

In the majority of these measurements, the event rate and pixel occupancy were very high which led to overlapping clusters and challenging pattern recognition. The data is still being processed, and methods to improve cluster analysis and overcome the overlap are being investigated.

Crystal and magnetic structure of TbMgNi2Co2 and TbMgNiCo3

Neutron Physics Laboratory - Neutron diffraction

Vitalii Shtender

Proposal ID

438

Progress report of proposal 438

Proposal title: Crystal and magnetic structure of $TbMgNi_2Co_2$ and $TbMgNiCo_3$

Dates of experiment: 07.12.2018 - 12.12.2018

Main proposer: V. Shtender and coproposers : Martin Sahlberg and Charles Hervoches

Instrument responsible Charles Hervoches

The aim of this proposal was to study magnetic structure of the $TbMgNi_2Co_2$ and $TbMgNiCo_3$ compounds. Neutron powder diffractions have been measured at several temperatures for each sample according to magnetic curves M(T).

From the obtained results, it was found out the magnetic structure. By several tries, it seems that we have some nice ferimagnetic structure with Tb moments ferromagnetic and Ni/Co moments also ferromagnetic but opposite to the Tb once (Fig. 1).

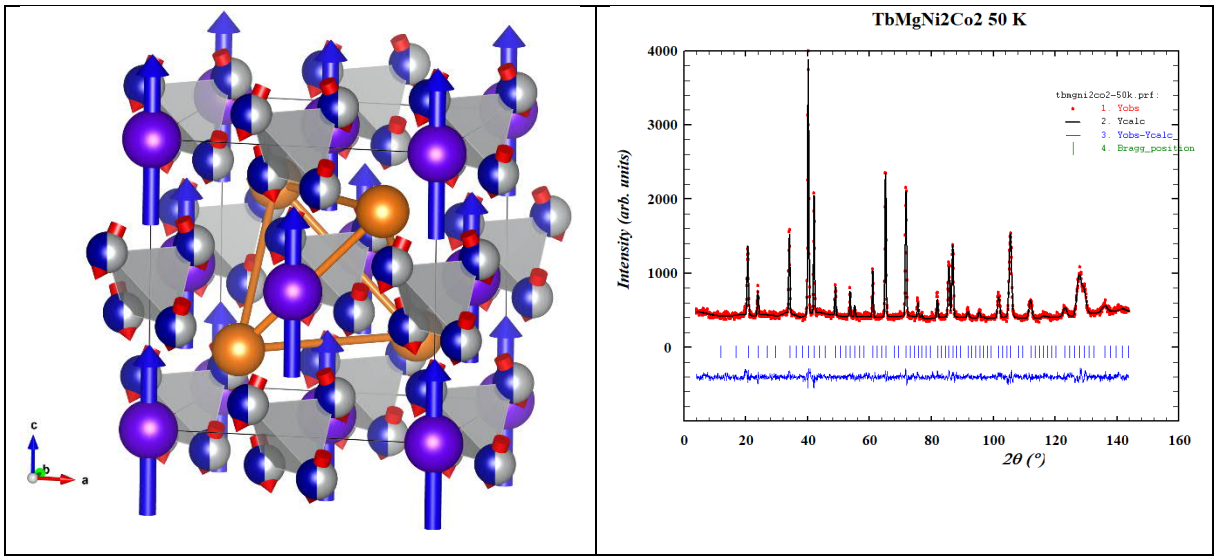

Fig. 1. Magnetic structure of the $TbMgNi_2Co_2$ compound and its refined NPD pattern at 50 K.

Study of Li ions transport in a solid electrolyte of the all-solid-state lithium ion battery

Neutron Physics Laboratory - Nuclear analytical methods with neutrons

Takane Kobayashi

Proposal ID

440

Study of Li ions transport in a solid electrolyte of the all-solid-state lithium ion battery

Takane Kobayashi, Ivo Tomandl, Jiri Vacik

In a path to a sustainable low-carbon society, conversion to renewable energy is steadily proceeding. However, the renewable energy from wind or photovoltaics fluctuates greatly, which makes it difficult to integrate it into the existing transfer grid. If an efficient electricity storage device (that would play a role of a buffer to compensate fluctuations of the energy) would exist, the speed of energy production conversion towards renewable energy would significantly accelerate. As a next generation key device for the electricity storage, a concept of all-solid-state lithium ion battery is promoted. Since the lithium ions move between the positive and negative electrodes in the active lithium ion battery, it is important for further development of the all-solid-state battery system to know how the lithium ions are distributed. It is especially important to understand how the lithium ions are behaving during the charging or discharging processes. Additionally, the issue of the interface resistance of a thin all-solid-state lithium ion battery is considered to be significant, as the resistance of the battery can be strongly affected by a lithium ion transfer.[1] We have recently investigated what happens in a separate solid electrolyte (of a thickness 150 micrometer) when a high voltage (< 15 V) is applied. The measurements were performed using the $^{6}Li(n, ^{4}He)^{3}T$ nuclear reaction. As a result, a lithium depletion layer (a considerable transfer of lithium ions between the sides of the biased thin electrolyte) has been observed (see Fig. 1). Evidently, the depletion of lithium concentration at the surface (and in a near-surface layer) is due to a delithiation process initiated by the biasing of the solid electrolyte.

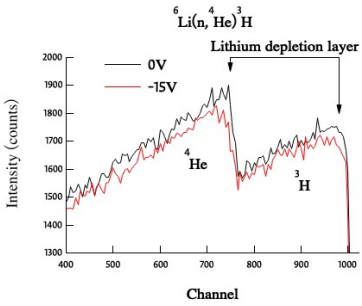

Fig. 1: ^{4}He and ^{3}T energy spectra from $^{6}Li(n, ^{4}He)^{3}T$ reaction obtained from a solid electrolyte with a thickness of 150 micrometer

Reference

1. J. Haruyama, K. Sodeyama, L. Han, K. Takada, and Y. Tateyama, Chem. Mater. 26, 4248-4255 (2014).

Use of Polycarbonate as an Alternative of Alanin Dosimetry [UPAAD]

Neutron Physics Laboratory - Nuclear analytical methods with neutrons

David Zoul

Proposal ID

441

Experimental Report

For irradiation in the LVR-15 research nuclear reactor can be used vertical channels H1, H5, H6 and H8, which are located on the periphery of AZ in Be reflector (H5, H6, H8) or in close proximity Be blocks (H1). The highest neutron fluence occurs in channels H5 and H6. For reactor power of 10 MW, are these values for thermal neutrons (0 – 0.501 eV) up to $7 \cdot 10^{13}$ cm^{-2} s^{-1}, for epithermal neutrons (0.501–100 eV) up to $8 \cdot 10^{13}$ cm^{-2} s^{-1} and for fast neutrons (> 0.1 MeV) to $6 \cdot 10^{13}$ cm^{-2} s^{-1}. In channels H1 and H8, neutron fluence is up to half lower. We use the H1 channel on the tube mail. It can be irradiated with the entire spectrum from the fast neutrons to the thermal neutrons, or epithermal neutrons, ie, by thermal cadmium wrapping.

On January 27, 2019, two samples of powdered polycarbonate were subjected to subsequent NMR spectrometric analysis using a magic angle spinning (MAS) method requiring powder form. One of the samples was irradiated with the entire neutron reactor spectrum plus gamma radiation, the other with epithermal and fast neutrons + gamma radiation. The resulting activities (higher in the whole reactor spectrum) were significantly higher than the release levels and will die out for several years due to the half-lives of the respective radionuclides (see Table 1).

Table 1. Concentration of long-term radionuclide activity in polycarbonate irradiated with reactor radiation at 84 kGy. Irradiation was performed in two modes: neutron reactor spectrum + gamma (RS + G) radiation and epitermal and fast neutrons + gamma radiation (EF + G)

Radionuclide	Half-life[a]	Activity[b], Bq · g^{-1}		Class of radionuclide[c]	Release level[c], Bq · g^{-1}
		RS+G	EF+G		
^{51}Cr	27,7 d	17185 ± 305	108 ± 13	3	30
^{58}Co (Ni)	70,9 d	< 30	19 ± 1	1	0,3
^{60}Co	5,27 a	108 ± 4	< 3	1	0,3
^{65}Zn	244,1 d	43 ± 6	< 10	1	0,3
^{110m}Ag	249,8 d	67 ± 4	7 ± 1	1	0,3
^{124}Sb	60,2 d	265 ± 8	37 ± 3	1	0,3

[a] - d: day; a: year
[b] - activity ± combined uncertainty (k = 1) at 21.1.2019
[c] - according to SÚJB Decree 422/2016 Coll. on radiation protection

Much of the activity generated was probably due to the contamination of the polycarbonate in the preparation of the powdered sample using metal tools. Therefore, for the next experiment, we have prepared 2 polycarbonate blocks of 10 x 10 mm and a thickness of 3 mm – see Fig. 1 – cut with a diamond disc and subsequently cleaned with an ultrasonic cleaner.

Figure 1: The polycarbonate blocks of 10 x 10 mm and a thickness of 3 mm cut with a diamond disc and subsequently cleaned with an ultrasonic cleaner

The samples prepared in this way were irradiated on February 18, 2019 in a similar manner as before the powder samples. No measurable activity of long-term radionuclides was found after irradiation. Under the law release level, both samples were recovered within two days of irradiation. The material itself is therefore very chemically pure, contains no measurable admixtures of heavier elements and its contamination occurred only when the powder form was prepared by contact with a metal tool.

On February 27, 2019, four samples were prepared in the same manner. The samples was irradiated with the entire reactor spectrum on 14/03/2019 on doses 14.77 kGy, 30.32 kGy, 66.87 kGy, 109.0 kGy what was measured by alanine dosimetry.

After irradiation, samples were stored in a freezer. After 3 days their activity dropped below the release level, the samples were transformed to powder form, and on March 11, 2019 analyzed by NMR spectroscopy at the Department of Low Temperature Physics of the Faculty of Mathematics and Physics of Charles University in Prague.

As with gamma irradiated specimens, the overall narrowing of the spectrum (or the decrease of the rotating bands, SSB, relative to the central line) is similar, as is the case with gamma irradiation. However, carbon resonance at 173 ppm (Fig. 2) is new. This could indicate the formation of some of the hitherto absent chemical groups (C = O with substitutions other than PC).

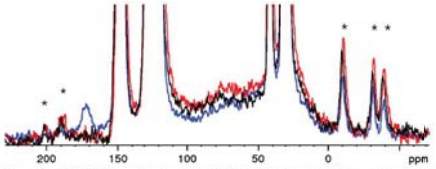

Figure 2 : ^{13}C MAS of neutron-irradiated (PCn4, blue) compared to non-irradiated (PC2, black; PC6, red) polycarbonate, scaled for matching the maximal intensities. Asterisks mark aromatic and carbonate SSB. Top: 7 kHz. Middle: 20 kHz. Bottom: 20 kHz with an expanded vertical scale

24.4. up to May 3, 2019, the final phase of research activities on the UPAAD project funded from Open Access and the CANAM project is currently underway. After completing this basic research we would like to move to applied research leading to commercial use. We are currently applying for a subsidy for this research within the IPNOP project.

Fifteen fully clear 10 x 10 x 10 mm organic samples are irradiated. Ten of these samples on gamma irradiation, doses of 15 kGy, 30 kGy, 45 kGy, 70 kGy, 110 kGy, 200 kGy, 400 kGy, 600 kGy, 800 kGy, 1000 kGy, five of these samples on LVR-15 reactor for doses of 15 kGy, 30 kGy, 45 kGy, 70 kGy, 110 kGy. Five samples from the reactor were accepted on the hot cells of object 254 (Radiochemistry II) on April 29, 2019 in a shielding container with appropriate documents, as weakly radioactive sources with a total activity of 1.5 kBq. All 15 samples (active and inactive) go first to a dosimetric laboratory where they are subjected to optical densitometry on a transmission scanner, then to a semi-hot cell where their microindentation takes place to determine changes in mechanical properties after irradiation, which may indicate structural changes in the polymer chains. The irradiation and subsequent measurements of samples take place throughout the week, according to a specific time schedule. The ultimate goal is to compare the physico-chemical effects of neutron and gamma radiation.

Changes in the compositional, structural, morphological, electrical and optical properties in elect

Laboratory of Tandetron

Mariapompea Cutroneo

Proposal ID

442

Report 442 Changes in the compositional, structural, morphological, electrical and optical properties in electrical insulator materials by ion beam**.**

Two well-established electrical insulators, graphene oxide and poly(methylmethacrylate) (PMMA) have been selectively exposed to controlled energy and fluence of ions. Ion micro beam has been proposed for processing of both graphene based material and polymeric foils for tailoring of their properties. In a single step, the mask-less production of circuit elements on graphene-oxide and poly(methylmethacrylate) was realized using a stream of 2.2 MeV alpha particles.

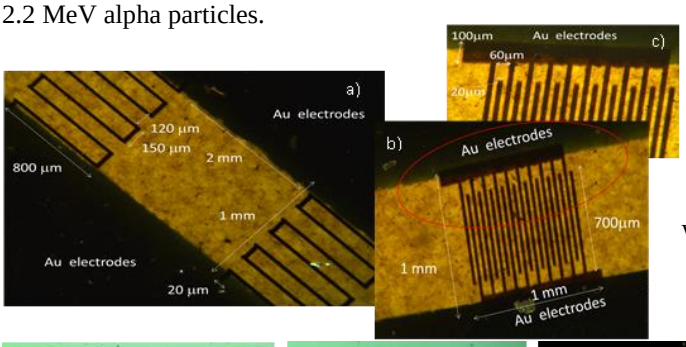

Fig. 1. Optical images 4x magnification of two resistors connected in parallel a) a large view of a capacitor b), a detail of the capacitor c) all written in graphene oxide (GO).

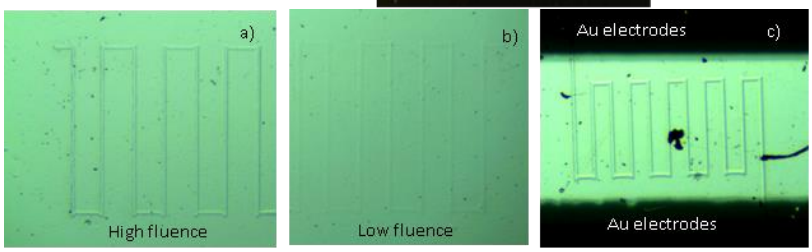

Fig. 2. Optical images resistors written at $3.8 \cdot 10^{13}$ ions/cm^2 a) at $3.7 \cdot 10^{14}$ ions/cm^2 b) a resistor written between two electrodes at $3.7 \cdot 10^{14}$ ions/cm^2 c) all written in PMMA.

Fig.2a reports swelling and shrinking and the contour have a glassy-appearance of the irradiated areas in PDMS. Since the glass transition of PMMA occurs at about 105° maybe the thermal degradation and deformation effects took place and the gas diffusion is not predominant any more. **Fig.2b** shows no swelling and shrinking maybe because as decreasing the size of the irradiated surface, the PMMA bears higher ion fluences because the related sheer stress will also be small and higher ion fluence can be applied.

The induced deoxygenation, and dehydrogenation change the compositional, structural and electrical properties in the exposed samples. The accuracy of the method has been investigated by Rutherford backscattering spectrometry, elastic recoil detection analysis as reported in Table I.

SAMPLE	*COMPOSITION OF THE FOILS (at %)*							
GO 7 µm	C	O	H	S	Mn	Ca	C/O	H/O
Pristine	52.5	27.1	19.7	0.65	0.05		1.94	0.73
Irradiated by 2.2 MeV He^{2+} ions at $6.4 \cdot 10^{14}$ ions/cm^2	56.7	23.8	16.0	0.65	0.05		2.14	0.60
Irradiated by 2.2 MeV He^{2+} ions at $1.1 \cdot 10^{15}$ ions/cm^2	60.4	26.9	14.9	0.65	0.05		2.54	0.63
PMMA 50 µm	C	O	H	S	Mn	Ca	C/O	H/O
Pristine	59.9	14.7	25.2			0.04	4.07	1.71
Irradiated by 2.2 MeV He^{2+} ions at $3.8 \cdot 10^{13}$ ions/cm^2	65.9	13.3	20.5			0.06	4.95	1.54
Irradiated by 2.2 MeV He^{2+} ions at $3.7 \cdot 10^{14}$ ions/cm^2	71.9	11.4	16.7			0.07	6.31	1.46

Table I Composition of GO foils un-irradiated and irradiated by 2.2 MeV Helium ions with 6.4 x 10^{14} ions/cm^2 and 1.15 x 10^{15} ions/cm^2 and of PMMA foils un-irradiated and irradiated by 2.2 MeV Helium ions with 3.8 x 10^{13} ions/cm^2 and 3.7 x 10^{14} ions/cm^2.

The shrinking is connected to the diffusion of gas during and after the ion irradiation. Shrinking decreases with the ion fluence because the incoming ions hit the already modified region and the amount of gas molecules decreases due to desorption in vacuum and the successive energy deposition occurs producing minor scission processes and cross-linking of radicals. Raman spectroscopy on GO indicated the generation of defects and structural modification as a consequence of the ion irradiation. Electrical measurements on the insulators indicated a significant reduction of resistivity on GO and a slight change in its electrical properties increasing the fluences of irradiating ions. In GO the deoxygenation of the foil induces a restoration of the electrical properties of graphene, while in PMMA the ion irradiation induces irreversible changes in its molecular structure by generation of chain scission, crosslinking and carbonization.

The present work is addressed to a design of direct–patterning of circuits or optical guides which are extensively used in soft electronic for the realization of flexible and stretchable electronics and in microelectronics.

Ion modification of GaN crystalline structures

Laboratory of Tandetron

Romana Mikšová

Proposal ID

317

Report regarding proposal "Ion modification of GaN crystalline structures."

A. Macková, A. Jagerová, P. Malinský, Nuclear Physics Institute of the Czech Academy of Sciences, v. v. i., Rez, Czech Republic
Z. Sofer, D. Sedmidubský, K. Klímová, Department of Inorganic Chemistry, Institute of Chemical Technology, Prague, Czech Republic
R. Böttger, S. Akhmadaliev, Institute of Ion Beam Physics and Materials Research, Helmholtz Zentrum Dresden-Rossendorf, Dresden, Germany

In our results, we have carried out a study of a GaN epitaxial layer (of c-plane and a-plane) implanted with Gd, Kr and Au ions at energy of 400 keV and and 5 MeV Au ions using implantation fluences ranging from 5×10^{14} cm^{-2} to 5×10^{15} cm^{-2}. The damage accumulation in the buried layer is much more pronounced in c-plane (0001) GaN than in a-plane (11–20) GaN for both ion species used. More pronounced differences in damage accumulation between a-plane and c-plane GaN are observed in the fluence range 0.5×10^{14}–1×10^{15} cm^{-2} for Gd implanted GaN and 1×10^{15}–5×10^{15} cm^{-2} in the Kr implanted GaN.

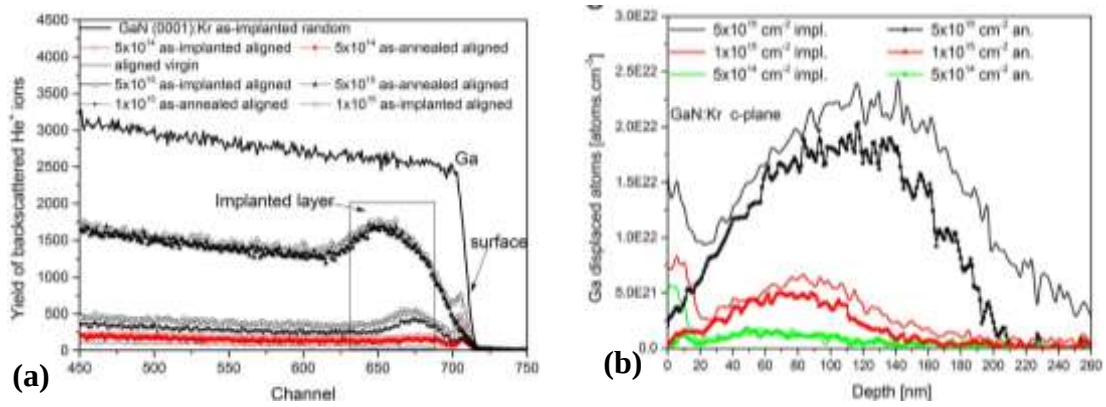

Figure 1. The RBS-channelling aligned spectra for as-implanted and as-annealed samples implanted with Kr ion in c-plane GaN (a) . The density–depth profile of displacement Ga atoms in GaN as-implanted with Kr ions: as-implanted and as-annealed c-plane GaN b).

Lower surface disorder is evident in Kr-implanted GaN than in Gd-implanted GaN for the same implantation fluence. Annealing has caused a progressive decline in the disorder preferably in the surface layer and also in the bulk implanted the latter one mainly for c-plane GaN for both ion species.

Gallium nitride implanted with 400-keV Au ions shows the bimodal depth profiles at a fluence of 5×10^{15} cm^{-2} in as-implanted samples. More damage accumulation was observed in the buried layer in the case of c-plane GaN than in a-plane for 400-keV ion implantation energy, in case the nuclear stopping prevails (Figure 2). In case of 5-MeV Au ions modified surface GaN, where electronic stopping prevails the surface damage is significantly lower comparing to 400-keV Au implantation and the long range defect.

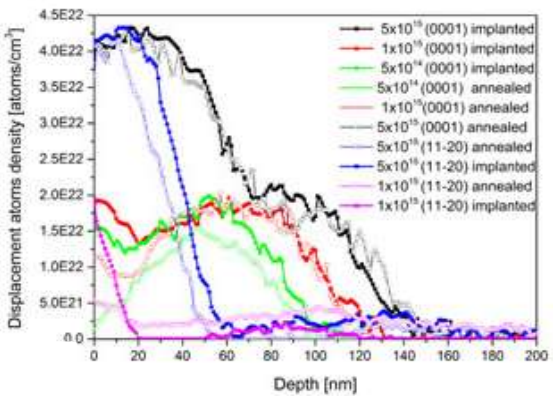

Figure 2. The density-depth profile of displacement atoms in gallium nitride as-implanted with Au at ion-implantation energy of 400 keV in as-implanted and as-annealed c-plane and a-plane GaN.

The results were published in Surface and Coatings Technology, Surface and Interface Analysis, Thin Solids Films and Nuclear Instruments and Methods in Physics Research B.

Study of structural properties of MAX/MX phase thin films synthetized by ion beam sputtering

Laboratory of Tandetron

Giovanni Ceccio

Proposal ID

445

Report regarding the proposal "Study of structural properties of MAX/MX phase thin films synthetized by ion beam sputtering"

G. Ceccio, P. Horak, A. Cannavò

Nucl. Physics Inst., Rez, Czech Republic

MAX phases are ternary carbides or nitrides with the formal stoichiometry formula of Mn+1AXn (n = 1, 2, 3), where M is representative of an early-transition d metal (i.e., Sc, Ti, V, Cr, Zr, Nb, Mo, Hf, and Ta), A is an element from (mainly) the IIIA or IVA group (i.e., Al, Si, P, S, In, Sn, and Pb), and X is either carbon or nitrogen. The properties of the MAX and MXene systems are based on combination of the best attributes of the metals and ceramics. For example, MAX phases are resistant to radiation, thermal shock or corrosion and exhibit high electrical conductivity. Thin films of MAX and MXene phases were prepared by ion beam sputtering followed by thermal annealing in vacuum. The thickness, composition and stoichiometry of the films were analyzed by the Rutherford Back-scattering method (RBS) and Nuclear Resonance Analysis (NRA) using α-particles with an energy of 2000 keV and 3.046, 4.280 keV for RBS and NRA, respectively. The measurements were carried out at the Tandetron 4230 MC accelerator at NPI (CANAM infrastructures). Important results were obtained studied the MAX phases: Ti_3InC_2 and Ti_2SnC (see Fig. 1)

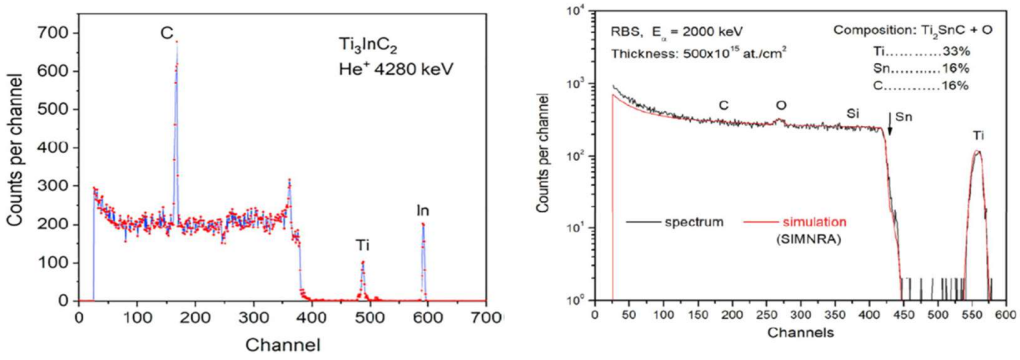

Figure 1 The NRA spectra of the Ti3InC2 film showing the C resonance analysis at 4280 keV(left) IBA analysis of the Ti2SnC thin film: RBS using 2 MeV alpha particles (right)

The data concerning the preparation of the MAX phase thin films by ion sputtering were partially published [1,2], but other results concerning the modification of the thin films by ion implantation are still under evaluation for future publications.

[1] Surface and Coatings Technology Volume 394, 25 July 2020, 12583
[2] RADIATION EFFECTS & DEFECTS IN SOLIDS 2020, VOL. 175, NOS. 1–2, 177–189

Testing and calibration of MIRAM spacecraft radiation monitor for ESA

Laboratory of Cyclotron and Fast Neutron Generators

Adam Smetana

Proposal ID

446

MIRAM at proton beams in CANAM

CANAM Cyklotron Report experiment LPC MIRAM, Sept. and Dec. 2019, Milan Malich – IEAP CTU Prague

We have performed measurements in two stages in September and in December 2019. The spectrometric response and SEU analog processing chain was tested of the MIRAM device and his LPC part. Miram LPC device is small, low-power radiation monitor for Space. It is composed from 300um 4xSi diodes (in tested device only one was assambled).

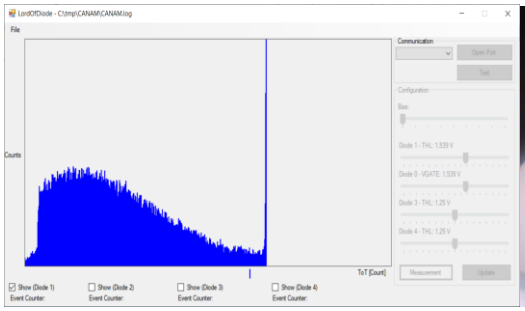

Figure 1: Histogram of Time over Threshold from Diode

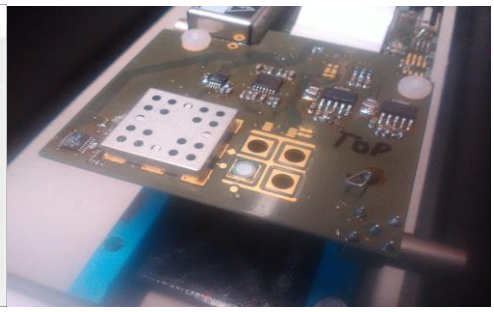

Figure 2: Analog Front End V

Device was tested in energy range 8 to 31MeV. Energy deponed by particle is converted to Time over Threshold (ToT) value. Result is histogram Time over Threshold values. Broad peak is energy of Beam 8MeV due pile up effect on Si diode and second thin peak is saturation peak of ADC. During Beam proton test no mallfunction caused by SEU was not observed.

Report z měření na cyklotronu Peter Rubovič, ÚTEF ČVUT v Praze

Dne 10.12.2019 proběhlo měření v cyklotronové laboratoři ÚJF AV ČR v Řeži. Měřili jsme úhlovou závislost odezvy 3D trasovače částic vyvinutého firmou Advacam ve spolupráci s ÚTEF ČVUT v Praze, který sestává z čtveřice hybridních pixelových detektorů Timepix s 300 µm tlustými křemíkovými sensormi a ztenčeními readout chipmi o tloušťce 100 µm, které jsou na sebe nalepeny. Měření proběhlo s protony o energii 35 MeV. Výstupem měření je ověření funkčnosti detektoru a vytvoření ukázky pro akademické a obchodné partnery. Na měřených datech lze pozorovat profil depozice energie protonů v sensoru. Tato informace může být využita například pro monitorování toku primárních i sekundárních částic v hadronové terapii při kalibraci generátoru částic.

CANAM Cyklotron Report experiment ACQP MIRAM, Dec. 2019, Carlos Granja, Cristina Oancea- ADVACAM Prague

The spectrometric and particle tracking response of the MIRAM ACQP BB Timepix-3 hybrid semiconductor Si sensor 500 µm for charged particle detection was tested with proton beams with energies ranging from 12 to 31 MeV, see Fig 1. Bias and rotation and scans were performed, see Fig. 2. The purpose was to examine the LET-response and tracking resolving power to high-LET particles (protons near the Bragg peak).

The pixel detector TPX3 ASIC chip provides quantum–imaging sensitivity and visualizes the track of each individual particle and its 3D direction, allowing LET determination over a wide LET range (0.1 – 100 keV/µm) for incoming particles under various angles. Results include per-pixel energy deposition (loss) and linear energy transfer (LET) at varying incident directions, see Fig.3.

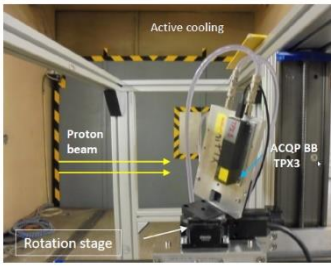

Figure 1. Experimental setup at the Cyklotron U-120 NPI, Rez. The ACQP BB TPX3 device was placed on a rotation stage and irradiated under several angles with tunable protons.

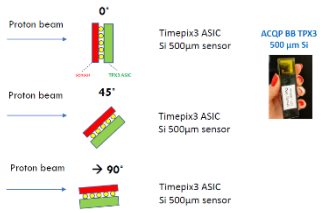

Figure 2. Schematic representation of the rotation scan using ACQP BB TPX3.

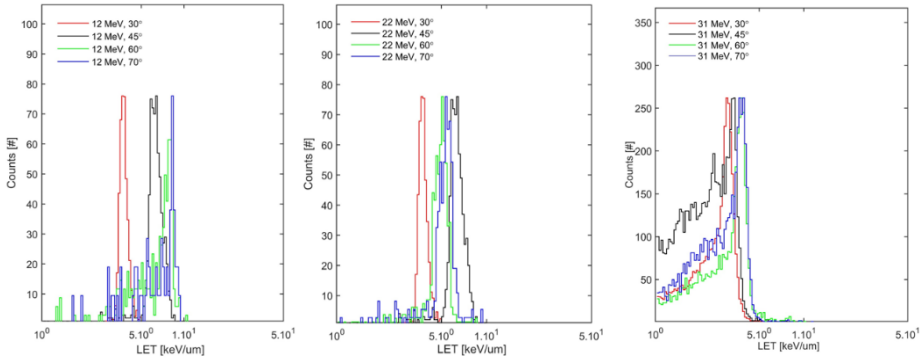

Figure 3. LET spectra measured with the Timepix–3 ACQP for a) 12 MeV, b) 22 MeV and c) 31 MeV proton beam. The data are displayed for measurements in air at: 30° (red), 45° (black), 60° (green) and 70° (blue) incident directions. The deposited energy, and LET, vary, namely near the Bragg peak.

SINE2020 feasibility study - DED sample residual stress measurement

Neutron Physics Laboratory - Neutron diffraction

Pavel Strunz

Proposal ID

449

Measurements in Direct Energy Deposition (DED) sample for FEM method check

Residual stress is a side effect of a Direct Energy Deposition (DED) processes. Understanding the phenomena allows choosing suitable deposition strategy to reduce residual stress and shape distortion. A FEM modelling of the DED process and other experimental method can evaluate residual stress distribution but those methods needs to be compared to known reference to provide correct results.

A cubic sample from stainless steel 316L deposited on InssTek MX600 DED device is investigated and residual stress and porosity are evaluated by software and lab technique usually available.

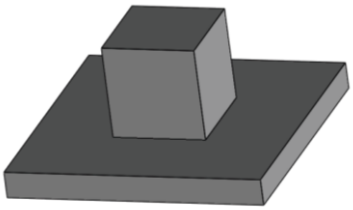

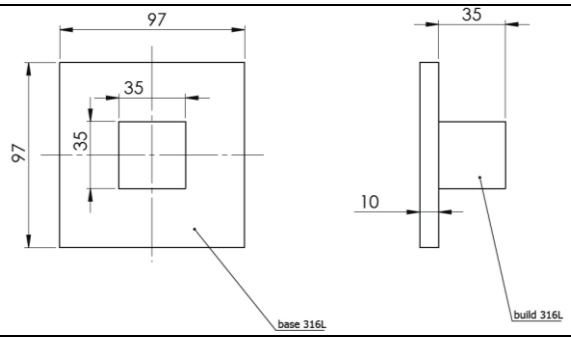

Scheme of the cubic sample made of stainless steel 316L

The incident and diffracted beam are formed by 5×5 mm^2 and 5 × open cadmium slits, respectively. To determine the three strain components, different geometrical arrangements of the examined specimen with respect to the scattering vector were performed.

The measured maximum compressive stresses correspond always to the z direction, being close to -400 MPa. A maximum tensile stress of ~ 100 MPa is found close to the top surface at line x=10 in y direction. The central region around the symmetry axis and around the z=12 line undergo compressive stresses.

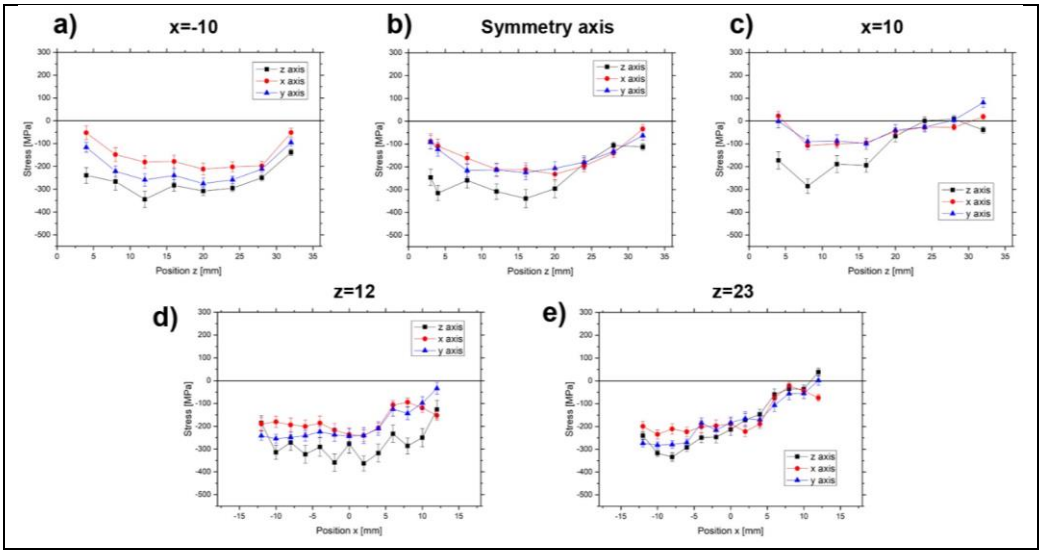

Residual stresses for the vertical lines at a) x=-10, b) x=0 and c) x=10 and for the horizontal lines at d) z=12 and e) z=23.

Residual stress measurement has shown that

- Maximum compression and tensile stresses are ~ -400 MPa and 100 MPa, respectively.
- Central region is confirmed to be under compression.
- Stresses do not mirror around the symmetry axis.
- Regions close to the top surface exhibit more asymmetry in the residual stresses, probably as a consequence of the distorted sample.

SINE2020 feasibility study - DED sample porosity measurement

Neutron Physics Laboratory - Neutron diffraction

Pavel Strunz

Proposal ID

450

Measurements in Direct Energy Deposition (DED) sample for FEM method check - porosity measurement

Residual stress is a side effect of a Direct Energy Deposition (DED) processes. Understanding the phenomena allows choosing suitable deposition strategy to reduce residual stress and shape distortion. A FEM modelling of the DED process and other experimental method can evaluate residual stress distribution but those methods needs to be compared to known reference to provide correct results. Porosity can influence the microstructure of the material and correspondingly also the modelling parameters.

A 2 mm slices cut from the original DAD cubic sample from stainless steel 316L deposited on InssTek MX600 DED device were investigated by SANS, and porosity was evaluated.

Measured data

The sample and its subsrate of the same material were scanned in several points. Some of the measured data are shown in the figure Fig. SANS5:

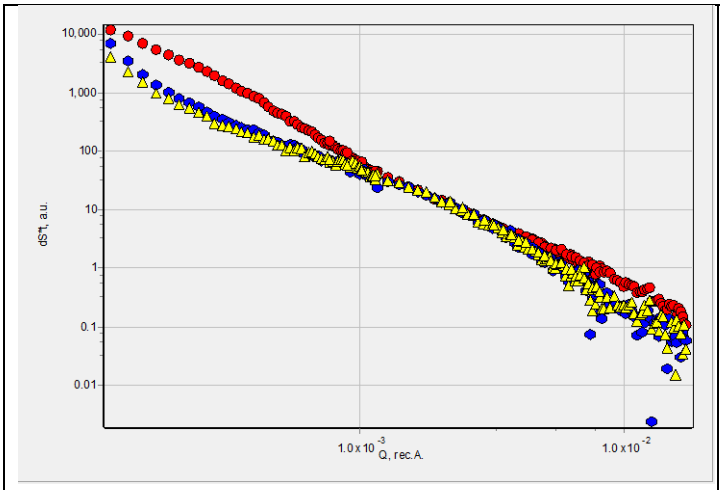

Fig. SANS5. Scattering for studied areas F (red spheres), H (blue hexagons) and L (yellow triangles).

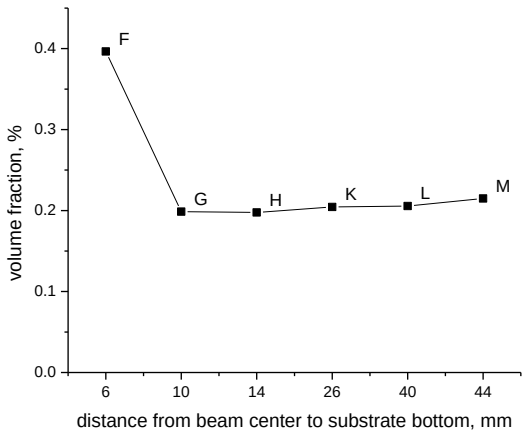

Fig. SANS6. Porosity volume fractions (small particles) as function of distance from sample side (area F – is substrate, G – partially substrate and studied material, K – is center of the sample).

For evaluation, model of spheres was used, using 2 log-normal size distributions – for small and large particles.

Although, SANS data for the locations H, K, K and M are alike, locations H and G showed rather higher intensity mostly in low Q ($<10^{-3}$ Å^{-1}) region (see Fig. SANS5). The SANS results showed that porosity (or other scattering objects) in substrate (point F) has about twice larger fraction (0.4%) for small particles model in comparison with deposited material (0.19-0.21%) (Fig. SANS6).

Conclusions

SANS measurement led to the conclusions:

- Scattering curves measured in deposited part of the sample are alike within statistical error. These data were fitted by spherical model assuming that scattering objects are pores. Fitted volume fraction of porosity (small particles model part) is about 0.2%, mean radius of pores ≈100 nm.
- Azimuthal scan didn't show any anisotropy in plane of the sample.

SINE2020 feasibility study - DED sample texture measurement

Neutron Physics Laboratory - Neutron diffraction

Pavel Strunz

Proposal ID

451

Measurements in Direct Energy Deposition (DED) sample for FEM method check

Residual stress is a side effect of a Direct Energy Deposition (DED) processes. Understanding the phenomena allows choosing suitable deposition strategy to reduce residual stress and shape distortion. A FEM modelling of the DED process and other experimental method can evaluate residual stress distribution but those methods needs to be compared to known reference to provide correct results. Important part of the microstructural modelling is the texture.

A cubic sample from stainless steel 316L deposited on InssTek MX600 DED device was investigated and texture was evaluated by software available in the lab.

Experimental Pole Figures

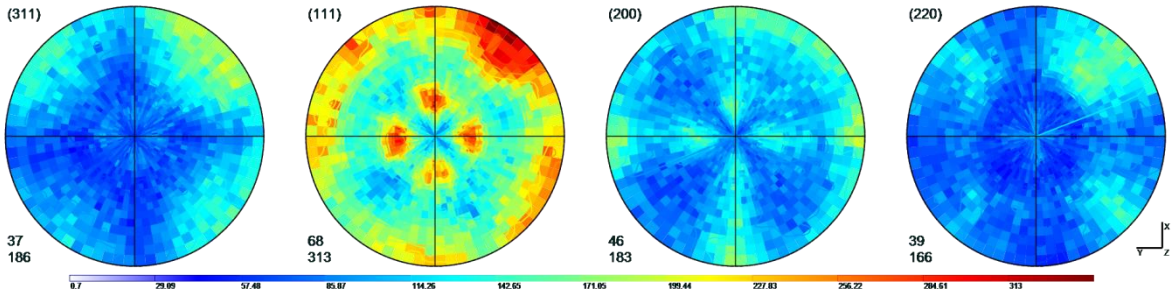

Calculated Pole Figures

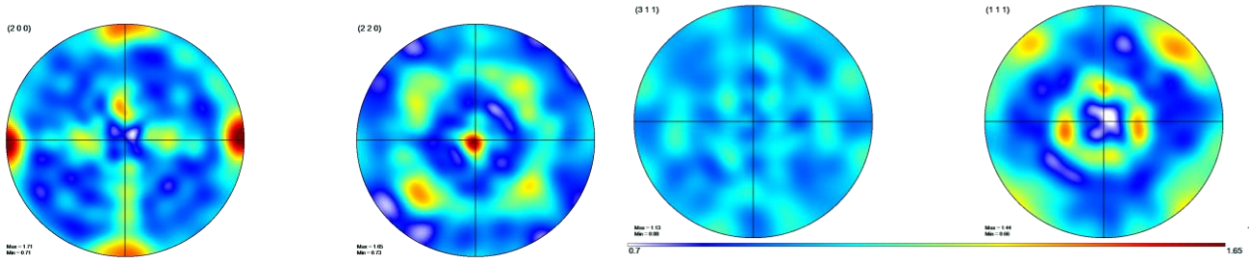

Inverse Pole Figures

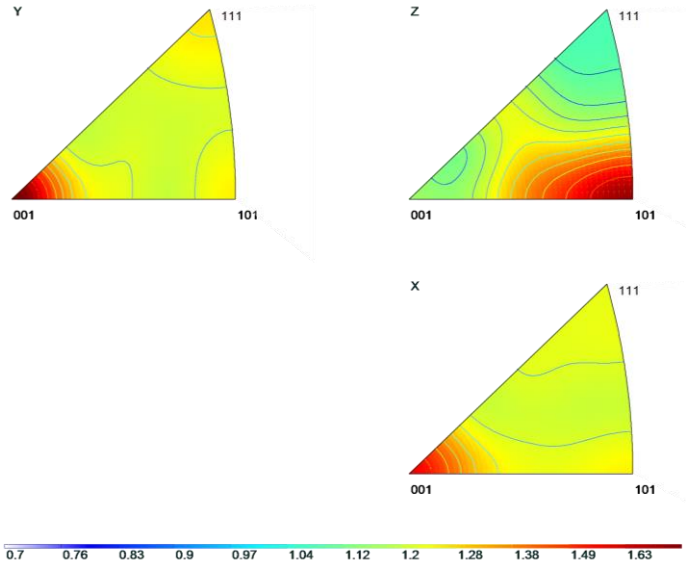

Conclusions

Texture measurement using neutron diffraction revealed that

- 110 crystallographic direction is preferably in Z direction (i.e. perpendicular to base plate)
- X and Y direction are qualitatively the same: 100 directions of crystallites are preferably parallel to them
- However, X direction texture is weaker (max. 1.44, min 0.94 in the inverse pole figure), Y direction is stronger (max. 1.68, min 0.94)

Characterisation of detectors response in heavy charged particle beams

Laboratory of Cyclotron and Fast Neutron Generators

Iva Ambrožová

Proposal ID

453

Report regarding proposal “Characterisation of detectors response in heavy charged particle beams”

Iva Ambrožová and Martin Kákona
Nuclear Physics Institute, Czech Academy of Sciences, Czech Republic

Si-diode based detectors have been used for measurements onboard aircraft and spacecraft for many years. Recently at our department, new open source Si-diode based spectrometers Airdos and Spacedos have been developed. Airdos is used for long-term measurements onboard aircraft, Spacedos is intended for measurements onboard spacecraft and satellites. To determine dosimetric characteristics such as absorbed dose, proper calibration is needed, which is usually based on the irradiation of detectors in various radiation beams.
Using the cyclotron proton beam with initial energy of about 35 MeV together with Al degraders, we obtained several calibration points. Spectra of deposited energy measured with Spacedos is shown in Figure 1, an example of a calibration curve for Spacedos is shown in Figure 2.

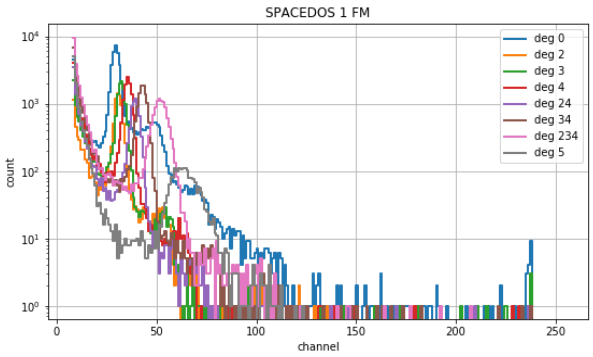

Fig. 1. Energy deposited spectra measured with Spacedos

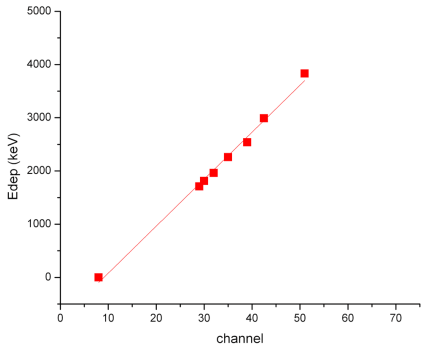

Fig. 2. Calibration curve for Spacedos

Reference

M. Kákona, Research on cosmic rays on board aircraft using a newly developed PIN diode detector, PhD thesis, CTU in Prague, 2020.
M. Kákona et al. AIRDOS - open source PIN diode airborne dosimeter, to be submitted to JINST, 2020.

Ex-situ & in-situ neutron diffraction study of deformation mechanism in Ti modfiied with trace B

Neutron Physics Laboratory - Neutron diffraction

Gergely Németh

Proposal ID

455

Report regarding proposal “Ex-situ & in-situ neutron diffraction study of deformation mechanism in Ti modfiied with trace B”

Gergely Németh, Faculty of Mathematics and Physics, Charles University

Ex-situ and in-situ neutron diffraction experiments were performed on 6x, 8x and 12x hot rolled commercially pure titanium grade 2 specimens modified by 0.1, 0.2 and 0.5 wt. % boron. The additional boron forms TiB monocrystal whiskers in pure Ti and the prepared material can be considered as discontinuously-reinforced metal matrix composite (DRMMC) which can have a relatively large to a moderate effect on mechanical properties depending on the elastic properties, shape, spatial arrangement and volume fraction of the reinforcement phase.

During the ex-situ measurement, neutron diffraction line scanning technique was used to study the residual stress (RS) distribution across the thickness of the rolled samples. First, the residual strain distribution was studied in three mutually perpendicular directions, denoted as LD (Longitudinal or rolling direction), TD (Transversal dir.) and ND (Normal dir.), corresponding to the main directions of the rolled plates. To increase the resolution (modification of the original proposal) and to have almost the same step-density, the step sizes were 0.5 mm, 0.45 mm and 0.3 mm for 6x, 8x and 12x rolled samples, respectively. Exposure times to collect the neutron diffraction signals from 0.1% B - 0.2% B and 0.5%B were 75 minutes and 100 minutes, respectively. Pseudo strains near the edge of the samples were treated according to [1].

The effect of the increased boron content on the RS distribution is most obvious after 12x rolling, as can be seen from Fig. 1. 0.1% B shows almost typical RS distribution for rolled monolithic material with local minimum in the center while in the case of 0.5% B, RS has local maximum in the same position.

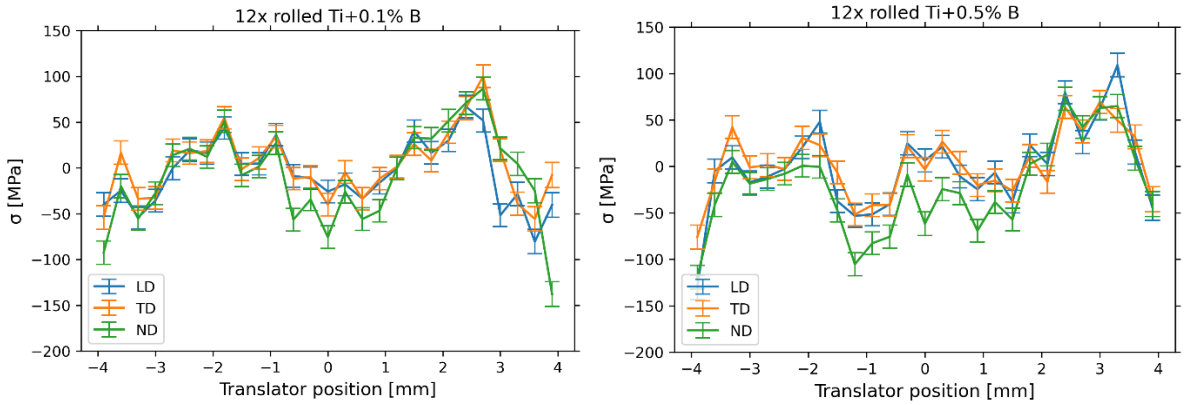

Fig. 1. Residual stress distribution in samples 12x hot rolled with B contents 0.1 wt. % and 0.5 wt. %

In-situ measurements were carried out only on 5 samples, since the deformation rig and the whole system had shown instability and many experiments had to be repeated several times without any reasonable outcome.

On the other hand, ex-situ measurements show valuable results and their publication is expected within a few months.

References:

[1] J. Šaroun, J. Rebelo-Kornmeier, J. Gibmeier, M. Hofmann, Treatment of spatial resolution effects in neutron residual strain scanning, Phys./B. 551 (2018) 468–471, https://doi.org/10.1016/J.PHYSB.2018.01.013.

Texture analyses in 3D printed steel products

Neutron Physics Laboratory - Neutron diffraction

Lenka Kuncicka

Proposal ID

458

Final report to the proposal „Texture analyses in 3D printed steel products“

L. Kunčická, R. Kocich VŠB TU Ostrava, 17. Listopadu 15, Ostrava 8, CZ

Ch. Hervoches, Nuclear Physics Institute, ASCR, Řež 130, Husinec, CZ

Aim

The aim of this project was to determine possible differences between the structure arrangement of cast and additively manufactured steel bars.

Experimental

- sample shape and measured location

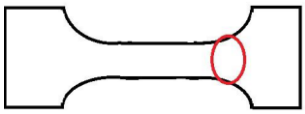

Results

➢ Textures of cast bar

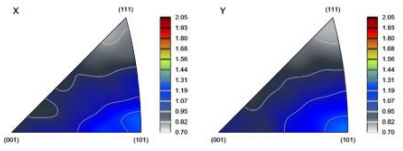

Textures of powder-based bar

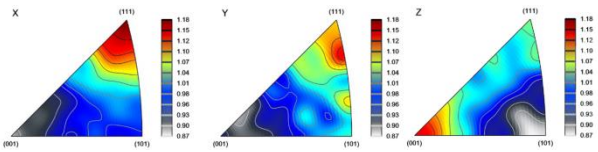

As can be seen from the results, preferential textures of both the investigated materials featured relatively low intensities, although the maximum intensity was slightly higher for the cast bar. Nevertheless, mutual comparison of both the structures revealed differences as regards the individual grains' preferential orientations. Whereas the cast bar exhibited quite a symmetrical texture across its cross-section, the powder-based bar exhibited more or less random grains orientations; this can clearly be seen especially in the inverse pole figures. The cast bar featured the texture formed by (200) planes, the dominant texture fibre was <100> oriented parallel to the rolling direction (<110> II RD). On the other hand, the powder-based bar only exhibited a slight tendency to form the (100) II RD preferential orientation (maximum intensity of 1.18).

Conclusions

The differences in the textures were primarily imparted by the processing technologies. Whereas the size and orientations of grains within the cast and subsequently rolled bars were influenced by several processing parameters (rolling direction, rolling time and speed of rolls, deformation history, etc.), the grains within the powder-based bar were formed during solidification of the structure after jet cladding and were not affected by any subsequent treatment.

Based on these results, processing steps can be optimized and possible heat treatment application can be considered to enhance the structure of the cast product.

Calibration of dosimeters and particle trackers for atmosphere and space radiation research

Laboratory of Cyclotron and Fast Neutron Generators

Carlos Granja

Proposal ID

331

Report for experimental proposal "**Calibration of dosimeters and particle trackers for atmosphere and space radiation research**"

C. Granja, *M. Sommer, M. Kakona, V. Stepan, I. Ambrozova,* et al., ODZ-UJF/CRREAT*

V. Zach, T. Matlocha, J. Stursa, et al., OU-UJF/CANAM

Summary: Measurements were carried out using proton beams from the UJF-CANAM Cyklotron on various types of radiation detectors selected for studies of radiation phenomena in the atmosphere in frame of the running OP3V project CRREAT. Performed tasks consisted of testing and calibration of detection response as well as intercomparison of different detector technologies (see Fig. top row) including passive devices such as TLDs and track detectors, and active devices such as single diode devices (LIULIN dosemeter, single pad diode CANDY) as well as position-sensitive imaging devices semiconductor pixel detectors. Timepix' resolving power and track visualization of single particles to a given radiation component (protons) of varying energy is shown (see Fig. middle row). Work included measurements on customized instrumentation for air-crew and space radiation dosimetry such as TEPC (Tissue Equivalent Proportional Counters – see Fig. bottom row). Data is presently under evaluation. Results will be subject of presentation/contribution at 1-2 conferences and 1-2 scientific journal articles.

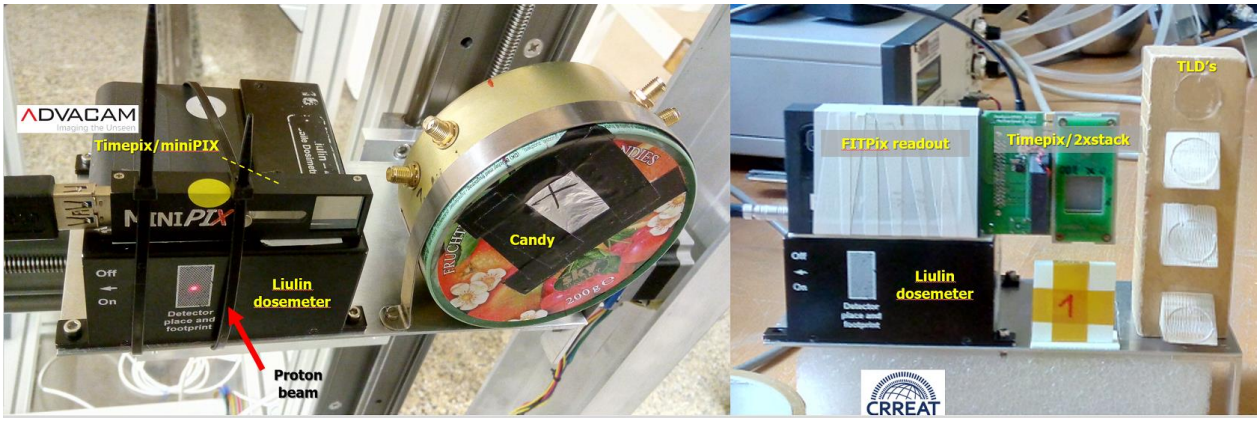

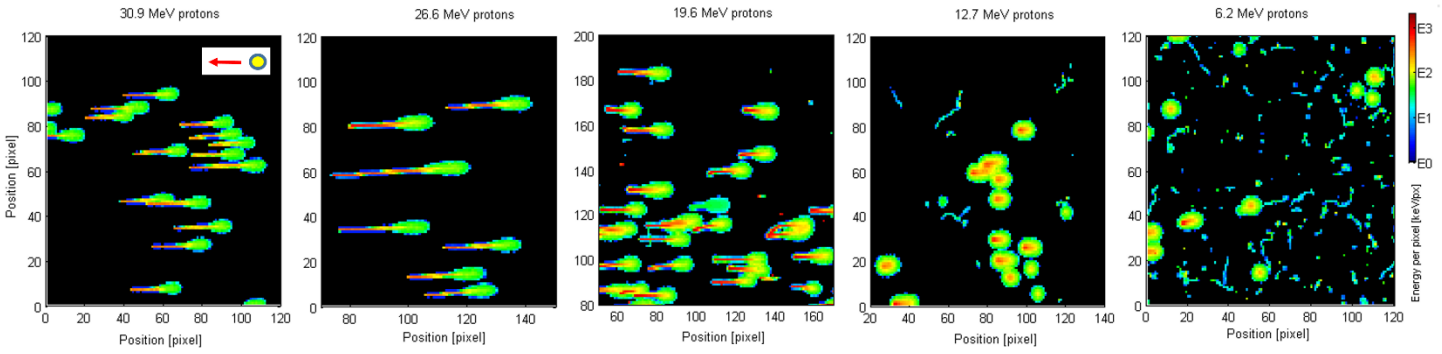

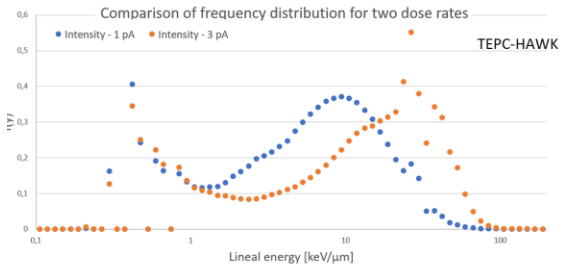

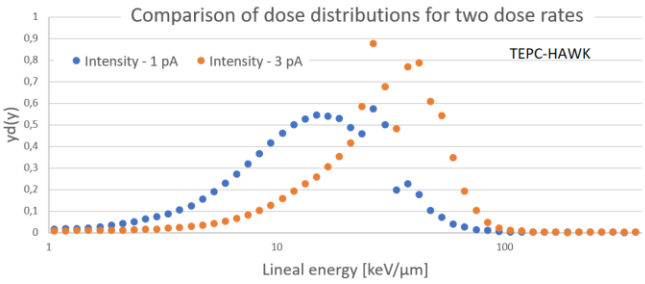

(*) Research performed in frame of the CRREAT project (Research Centre of Cosmic Rays and Radiation Events in the Atmosphere) supported by European Regional Development Fund-Project CZ.02.1.01/0.0/0.0/15_003/0000481.

Identification of microscopic uranium particles using fission tracks in solid detectors

Neutron Physics Laboratory - Nuclear analytical methods with neutrons

Jan Lorincik

Proposal ID

332

Report regarding proposal " **Identification of microscopic uranium particles using fission tracks in solid detectors"**

J. Lorinčík, K. Sihelská, K. Řezanková, F. Sus, Vl. Strunga, J. Kučera

The goals of this project were (A) the study of the number of fission tracks as a function of enrichment and size of U-particles, (B) the optimization of the fission track (FT) procedure for higher reproducibility, robustness, and accuracy.

A quantitative relation between the U-particle enrichment, size, and the number of FTs was used in the following form *[1]*: $N_T = N_{235} \cdot \sigma_f \cdot \varepsilon \cdot t \cdot \phi_{therm}$ … (1) , where N_T denotes the number of fission tracks; N_{235}, the number of ^{235}U atoms in a particle; σ_f, the fission cross section for ^{235}U [586 b]; ε, the registration efficiency (0,4); t, the irradiation time [120 s]; Φ_{therm}, the flux of thermal neutrons [3,2 x 10^{13} $cm^{-2}s^{-1}$]. Then, N_{235} can be obtained from $N_{235} = 3 \cdot (\rho_{U3O8} \cdot V_P)/M_{U3O8} \cdot N_A \cdot A_{235}/100$ … (2), where ρ_{U3O8} is U_3O_8 particle density [8,3 g/cm^3], V_P volume of the particle [cm^3], M_{U3O8} the molar mass of U_3O_8 [842,1 g/mol], N_A the Avogadro's constant, A_{235} the enrichment [%]. Constant 3 in eq. (2) corresponds to the number of U atoms in U_3O_8 molecule. Since SEM images can provide only areas of 2D projections (characterized by equivalent circle diameter – d_{ECD}) of 3D shapes of particles, the geometry models, e.g. sphere, cylinder, cube must be used for *Vp* estimation.

For experimental work, standard reference materials of U_3O_8 were used: CRM 129-A (NU), CRM 010 (1% ^{235}U enriched), CRM 030-A (3% ^{235}U enriched). Then FT sample assemblies (see more detail in reports of project CANAM:ID241) were prepared and irradiated in the reactor LVR-15 with irradiation parameters specified above. After etching of the Lexan detectors, optical images were made (see Fig. 1 a-c) and the FTs manually counted. The comparison of theoretical estimates and experimental data (lines vs. data points) is in Fig. 1 d.

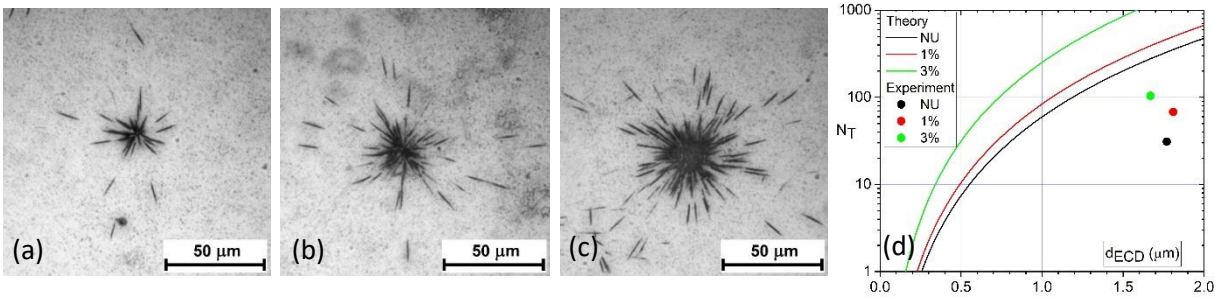

Figure 1.Optical images of FTs corresponding to U_3O_8 particles of NU (a),1 %U (b),and 3%U (c) [2]. Number of registered FTs in the images (a)-(c) for NU, 1%U, 3%U is 31, 68, 104, resp. (d) Comparison of experimental values (circle symbols) and theoretical estimates (full lines) based on equations (1) and (2) for spherical geometry model ($V_P = \pi/6 \cdot d_{ECD}^3$).

In parallel to the above study, large effort has been spent on improvement of the FT procedure. This goal has been achieved by (i) reconfiguration of the fiducial marks for better particle position precision, (ii) addition of sticky collodion for better particle adhesion, (iii) redesigning of the FT sample assembly for simpler and more reliable manipulation, (iv) employing new optical microscope with motorized stage for automated creation of compound photos of large areas of the Lexan detector, and (v) implementing efficient coordinate transformation algorithm for transfer of particle coordinates between instruments.

In summary, the dependence of the number of FTs on the particle enrichment and size has been investigated both theoretically and experimentally. There is a discrepancy between the theoretically predicted numbers of FTs and the counts of FTs obtained from the experiment. A combined effect of overestimated values of neutron fluences, material density, and FT registration efficiency could have been responsible for that. More experiments are needed to support that explanation and to provide more accurate data for theoretical predictions.

The main outcome of this project is substantial improvement of the FT procedure, which achieved the readiness level that allowed for the proficiency testing for nuclear safeguards.

[1] O. Stetzer, et al, . Nucl. Instr. Meth. Phys. Res. A525 (2004), pp. 582-592.
[2] S. Konegger-Kappel, et al https://www.iaea.org/sites/default/files/19/07/cn-267-book-of-abstracts.pdf, CN267-226, pp.228.

Testing of the Chamber for Light Ion Detection

Laboratory of Cyclotron and Fast Neutron Generators

Martin Ansorge

Proposal ID

460

Final report regarding the proposal „Testing of the Chamber for Light Ion Detection“

M. Ansorge, J. Novák, M. Majerle, Nuclear Physics Institute of the CAS, Rez, Czech Republic

Motivated by gas production in construction materials of future fusion-related facilities as well by the basic research of nuclear reactions new detection system is under development at NPI of the CAS in recent years. The chamber is equipped with dE-E Si-detector telescopes for distinguishing between charged particle types. The CAEN V1730 digitizer is used for data acquisition. In figure 1 the vacuum chamber is shown during the preparations on the on-beam tests of electronics.

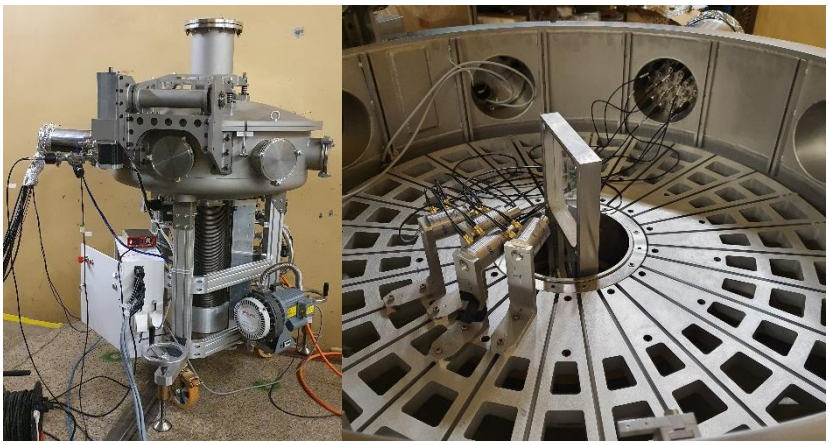

Figure 1 shows the typical experimental setup during the on-beam tests. Telescopes with Si-detectors are placed around the central sample-holder.

Days-lasting measurements with several irradiations of PE, C, Al samples were successfully performed, and the acquisition chain was finalized. The signal-noise ratio of detectors was suppressed by additional electro-magnetic shielding of preamplifiers. The detection system exhibited a good ability to measure the energy distribution of charged particles and the reasonable separation of particle types was achieved, see figure 2. It was shown that the time resolution of detected events is sufficient for usage the ToF technique and ToF method was successfully implemented.

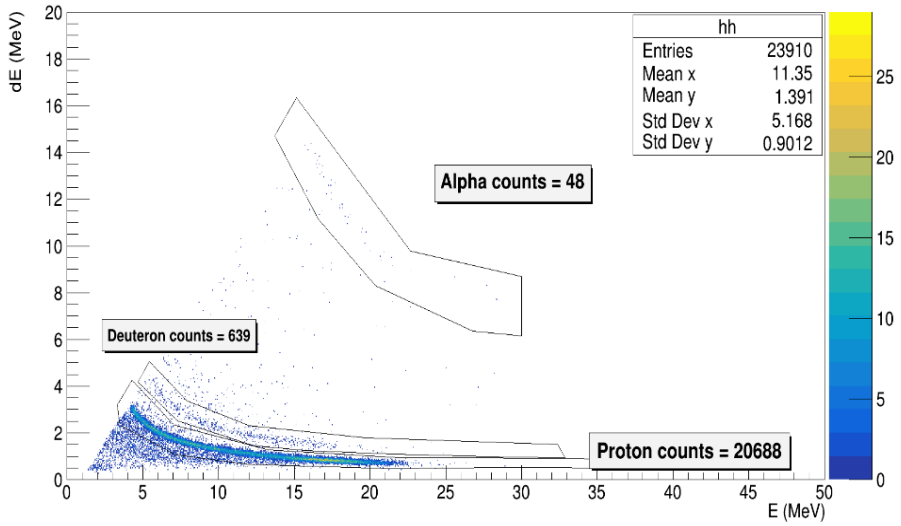

Figure 2 shows the dE-E plot of detected charged-particle-events from the six hours long irradiation of the PE target foil (thickness of 180 um, diam 3 cm) which was mounted into the central position of the vacuum chamber.

Many challenges are still ahead of us but the measurements that have been made provided us with very useful data which are used as feedback for detection electronics enhancements as well as for the development of a comprehensive software framework for data analysis in measurements of double-differential cross-sections for reactions (n, cp) induced by fast neutrons.

Characterization of Residual Stresses Distribution in Laser Cladded H13 tool steel

Neutron Physics Laboratory - Neutron diffraction

Karel Trojan

Proposal ID

461

Report regarding proposal "Characterization of Residual Stresses Distribution in Laser Cladded H13 Tool Steel"

K. Trojan [1,a], D. Canelo-Yubero[2], J. Čapek [1], N. Ganev [1]

[1] Department of Solid State Engineering, Faculty of Nuclear Sciences and Physical Engineering, CTU in Prague, Trojanova 13, 120 00 Prague 2, Czech Republic
[2] Department of Neutron Physics, Nuclear Physics Institute, ASCR, v.v.i., 25068 Řež, Czech Republic
[a] karel.trojan@fjfi.cvut.cz

Laser cladding was carried using a IPG 3kW Yt:YAG fibre laser and powder of the AISI H13 tool steel. Five-layer sample was formed from six and seven overlapping beads on the substrate made from AISI H11 tool steel. The state of residual stress and the dependence of the FWHM parameter were described using neutron diffraction in the middle of the sample in the plane perpendicular to cladding.

It was found from the measured residual stresses in three different sample orientations (see Fig. 1) that the greatest gradient of residual stresses (RS) is in the direction normal to the surface (N – normal direction). According to the literature study [1, 2], the maximum residual stresses are located 4 mm below the surface and compressive stresses prevail in the T direction. The substrate, on the other hand, exhibits tensile residual stresses. According to our results in the clad itself in the T direction, tensile RS predominate, on the contrary, in the substrate compressive RS with one maximum of tensile RS approximately 3 mm below the surface of the substrate were determined.

Laser deposition of the H13 tool steel showed a great application potential. The obtained results will help to understand the development of residual stresses within the thickness of the newly formed material. This knowledge can be used to design a procedure for laser beam deposition of larger volumes.

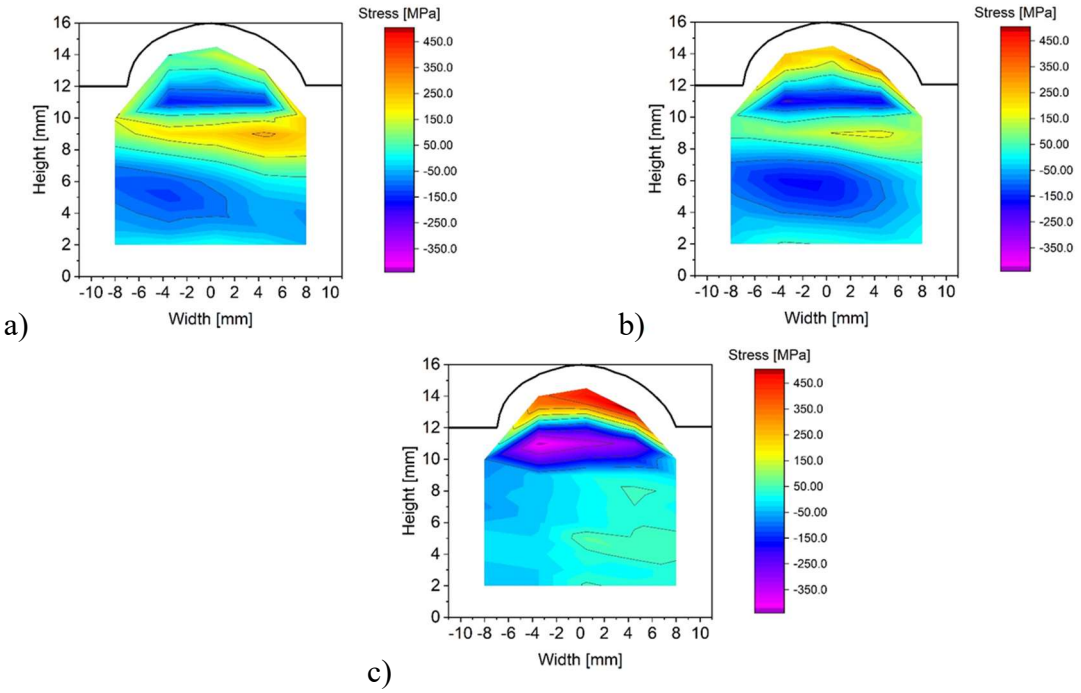

Fig. 1: Map of bulk residual stresses in the cross section of the clad in a) L, b) T and c) N direction.

Reference

[1] Cottam, R., Wang, J., & Luzin, V. (2014). Characterization of microstructure and residual stress in a 3D H13 tool steel component produced by additive manufacturing. Journal of Materials Research, 29(17), 1978-1986. doi:10.1557/jmr.2014.190

[2] Bailey, N., Katinas, C., & Shin, Y. (2017). Laser direct deposition of AISI H13 tool steel powder with numerical modeling of solid phase transformation, hardness, and residual stresses. Journal of Materials Processing Technology, 247, 223-233.

Measurement of retained austenite in inductive treated spring steel

Neutron Physics Laboratory - Neutron diffraction

Charles Hervoches

Proposal ID

462

Report on CANAM proposal: „Measurement of retained austenite in inductive treated spring steel“

Anna Olina, Miroslav Píška, Martin Petrenec, Brno University of Technology, Czech Republic
Charles Hervoches, Premysl Beran, Nucl. Physics Inst., Rez, Czech Republic
Jirí Pechoušek, Palacky University in Olomouc, Czech Republic
Petr Král, Institute of Physics of Materials, Czech Academy of Sciences, Brno, Czech Republic

In this study, four different inductive heat treatments were applied to fine grain vanadium micro-alloyed spring steel in order to obtain the best combination of high strength and sufficient ductility. All samples were studied by means of three analytical methods (neutron powder diffraction, Mössbauer spectroscopy, and EBSD) with the main focus on the assessment of retained austenite (RA).

Table 1: Parameters of the induction heat treatment.

Specimen	Austenitization Temp., ^{O}C	Temp. after Quenching, ^{O}C	Tempering Temp., ^{O}C
Q1	850	40	-
Q2	850	40	-
Q3	850	180	-
Q4	850	180	-
QT1	850	40	460
QT2	850	40	420
QT3	850	180	460
QT4	850	180	300

Neutron diffraction provided the results from the bulk of the material. It was demonstrated that RA distributed mostly in the core area of the specimens due to the fast inductive heat treatment, which provides a lower transformation speed in the core area of the specimens in comparison with the surface layer.

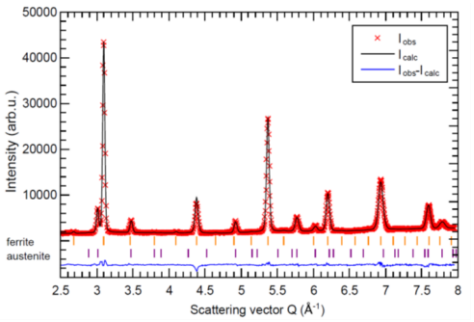

Fig 1. Neutron diffraction profile of specimen QT3. Bragg positions for ferrite and austenite are shown

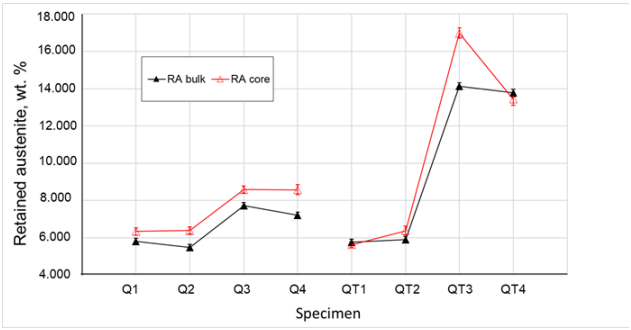

Fig. 2. Weight fraction of retained austenite in (%).

The influence of RA on the mechanical properties of the material has also been evaluated by comparing specimens QT1 and QT3. The amount of RA in the bulk of the specimen QT1 is 2.4 times lower than in QT3, but both samples showed reduction of the area >35%. It indicates that ductility is not affected by the higher amount of stabilized RA in the QT3 specimen. In contrast UTS and hardness exhibit a significant decrease for QT3, the specimen with the higher amount of soft FCC (RA) phase.

Results from the experiment have recently been published [1]

[1] Assessment of Retained Austenite in Fine Grained Inductive Heat Treated Spring Steel, A. Olina, M. Píška, M. Petrenec, Ch. Hervoches, P. Beran, J. Pechoušek, P. Král, *Materials* ***2019****, 12, 4063; doi:10.3390/ma12244063*

USANS investigation of 100Cr6 double row ball bearings for automotive power transmission

Neutron Physics Laboratory - Neutron diffraction

Massimo Rogante

Proposal ID

465

Report regarding proposal "USANS investigation of 100Cr6 double row ball bearings for automotive power transmission".

Massimo Rogante, Rogante Engineering Office

The two (new and old) double row ball bearings were preliminarily cut to obtain 3 mm samples suitable to carry out the experiment, see Figure 1.

Fig. 1.

The steel samples scatter excessively. In low Q region the strong multiple scattering appeared, which significantly distorted SANS curves. It caused by to high scattering contrast (mainly – magnetic difference of scattering length densities between large austenite/martensite and ferrite grains) and large thickness of the samples. This scattering forms intense scattering background for high Q part, and it makes not possible to detect signs of degradation in the material. The small difference in intensity is due to slightly different thickness (the old sample is a little thinner than the new one), see Figure 2.

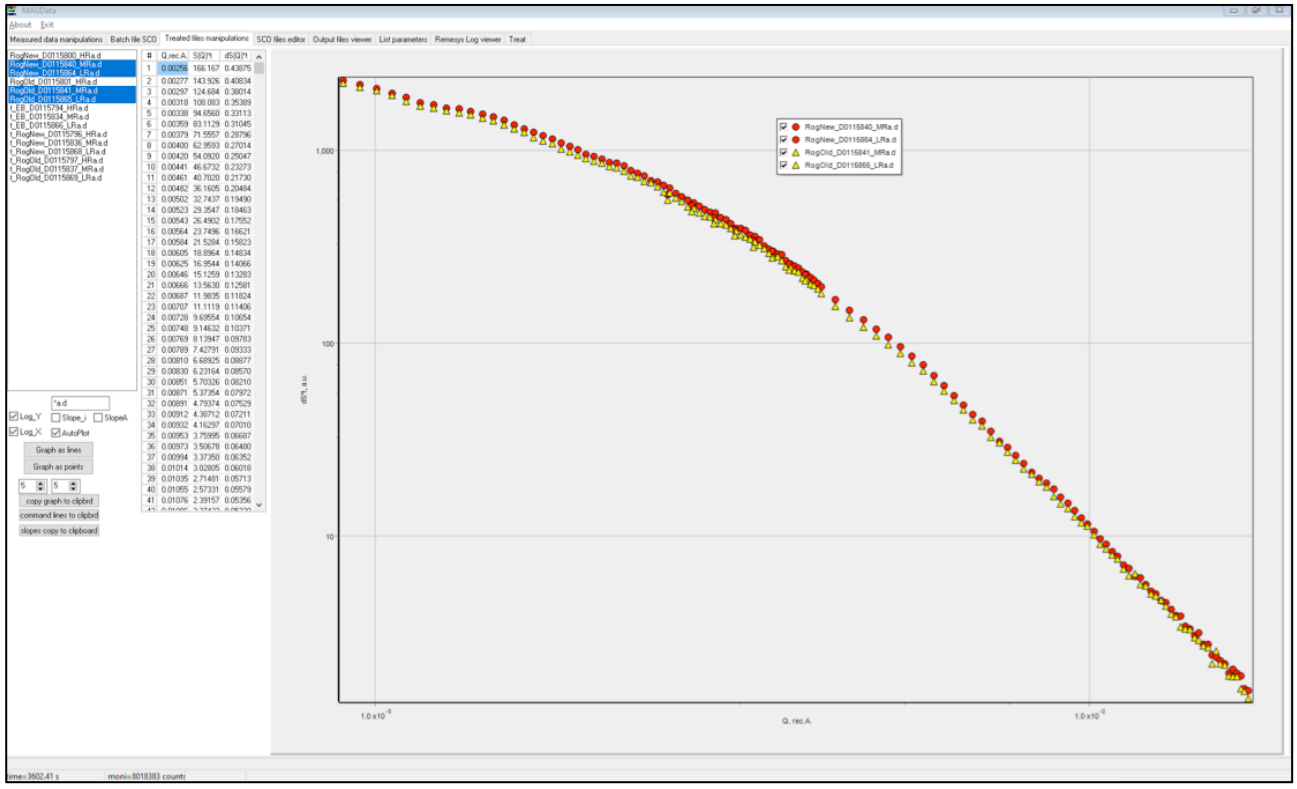

Fig. 2. (new sample – red, old sample – yellow).

Advanced organic-inorganic nanostructures

Laboratory of Tandetron

Vladimir Cech

Proposal ID

466

Report on the project "Advanced organic-inorganic nanostructures"

V. Cech, Inst. Mater. Chem., Brno Univ. Technol., Brno, Czech Republic
A. Romanenko, A. Mackova, Nucl. Physics Inst., Rez, Czech Republic

The main task of the proposed experiment was to provide an elemental analysis of polymer-like hydrogenated amorphous carbon-silicon (a-CSi:H) films using RBS and ERDA. The polymer-like a-CSi:H films were deposited from the tetravinylsilane (TVS) precursor by continuous wave (low-pressure plasma-enhanced chemical vapor deposition, LP PECVD) at an extremely low RF power of 0.2 W. These films were found to be unstable under ambient conditions and subject to post-deposition oxidation. The polymer-like film must therefore be overcoated with a 6-8 nm thick barrier layer to protect it and prevent degradation. A compact a-CSi:H film with a density of 2.0 g/cm^3 was successfully used as a barrier (XPS depth profiling), which was deposited from the TVS/Ar mixture by pulsed plasma at 25 W. To optimize the elemental analysis and increase the sensitivity to light elements, the films were deposited only on glassy carbon as a substrate. Further ERDA measurements showed a problem with the sputtering of polymer-like film and therefore it was necessary to optimize the ERDA charge per measurement. The areas affected by irradiation are visible to the eye as the charge was gradually reduced by 7.4, 3.7, 1.48, and 0.74 μC per measurement, see Fig. 1.

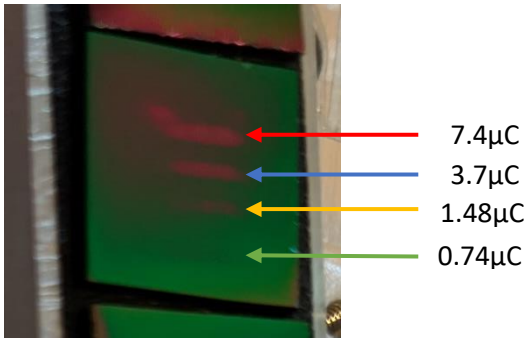

Fig. 1. Photo of the polymer-like film after testing in (a) ERDA geometry and (b) RBS measurements.

Although the ERDA charge was only 0.37 μC per measurement and 20 consecutive measurements were made at one location (the angle of incidence was 75°), the film on the surface is subject to changes during irradiation. It was found that both the thickness and the hydrogen concentration are reduced. Using an RBS charge of 0.74 μC per measurement (the angle of incidence was 7°), 10 measurements in a row were performed at one location. The final ERDA and RBS spectra corresponding to a charge of 0.74 μC can be seen in Fig. 2. The composition of the film (atomic [mass] concentration) is as follows: Si 7[28.2]%, C 37[63.8]%, H 56[8]%. The film thickness of 6200×10^{15} at/cm^2 corresponds to a thickness of 591 nm (measured by spectrometric ellipsometry) when a density of 1.2 g/cm^3 is used (GISA program).

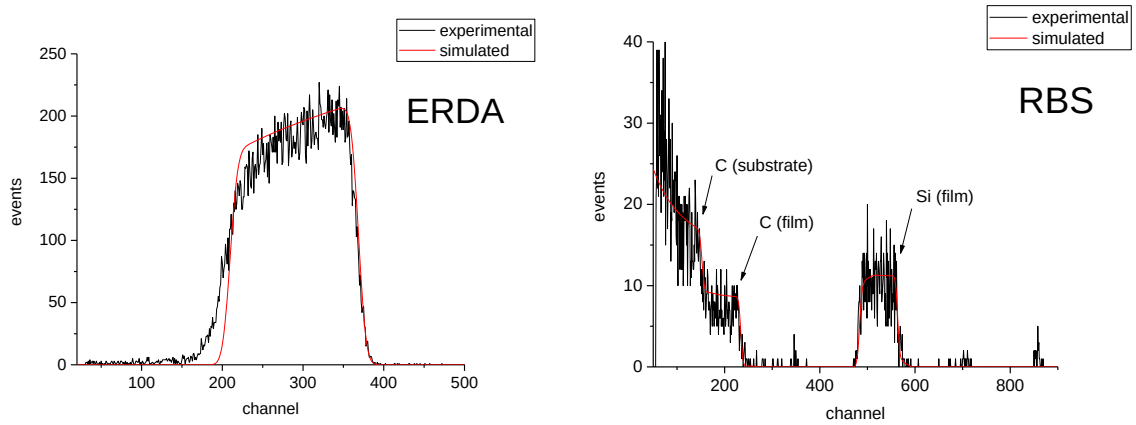

Fig. 2. ERDA and RBS spectra of polymer-like film corresponding to a charge of 0.74 μC.

Careful analysis of polymer-like a-CSi:H films is important for the further construction of layered nanostructures combining the polymer-like and oxygen bound a-CSiO:H films.

Crystal and magnetic structure of La18M3Co28 (M=Mg,In,Cd)

Neutron Physics Laboratory - Neutron diffraction

Vitalii Shtender

Proposal ID

467

Report regarding proposal “Crystal and magnetic structure of $La_{18}M_3Co_{28}$ (M=Mg,In,Cd)”

V. Shtender, M. Sahlberg, Uppsala University, Sweden
Instrument responsible: C. Hervoches P. Beran, Nucl. Physics Inst., Rez, Czech Republic

The aim was to investigate crystal as well as magnetic structures of the $La_{18}M_3Co_{28}$ (M = Mg, Cd and In) compounds. There was need to confirm the XRD first results on incommensaturate crystal structures and resolve their different magnetic properties.

Neutron powder diffraction experiments were performed on different samples of general $La_{18}Mg_3Co_{28}$ composition at 298 K using the MEREDIT instrument. The motivation for the experiments was to investigate the possible large displacement of Mg.

The extracted data is still under evaluation but preliminary results propose modulated structure of the $La_{18}Mg_3Co_{28}$. Observed and calculated neutron powder diffraction profiles are shown in fig. 1. The preliminary proposed incomensurated structure which is along the c-axis with a Mg atom inside the tunnel. The maximum entropy method (MEM) was applied to calculate nuclear density of the unit cell. The output of the calculation is shown in Fig 1. The cut-off intensity was set to 0.5 fm. The area of disordered space where Mg atoms could be located is clearly visible. Other atoms don’t show anisotropy behavior.

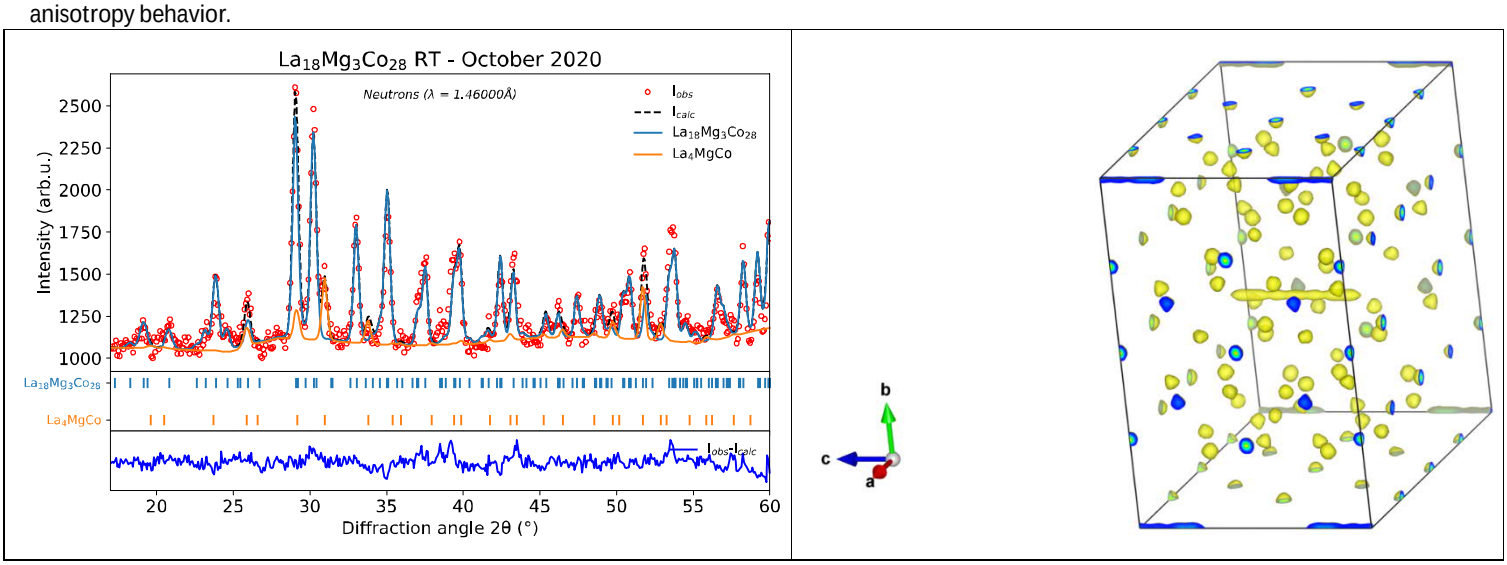

Fig 1. Refinement of the NPD for $La_{18}Mg_3Co_{28}$ at 298K and proposed structure with the nuclear density.

Comparative study of performance of Silicon and Silicon Carbide detectors during RBS and ERDA.

Laboratory of Tandetron

Lorenzo Torrisi

Proposal ID

348

Comparative study of performance of Silicon and Silicon Carbide detectors during RBS and ERDA

L. Torrisi[1], V. Havranek[2], M. Cutroneo[2], A. Mackova[2] and A. Torrisi[2]

[1]Dipartimento di Scienze Fisiche MIFT, Università di Messina, Italy
[2]Nuclear Physics Institute, AS CR, Rez, Czech Republic

SiC are able to detect radiation at low and high energy, due to the controllable active region depth using adapt inverse bias of the Schottky barrier in presence of a thin surface metallization of contact. We have demonstrated that it is possible to use SiC diodes to detect helium ions with energy in the range of about 0.1–6.0 MeV with a sufficient energy resolution, similar to that of silicon detectors, capable to be employed for qualitative and quantitative RBS analyses. The experiment was performed using a prototype diode with a surface metalized semiconductor, 200 nm thickness in Ni_2Si alloy, with up to 80 μm active region depth, using a bias of −200 V at which this active region is reduced to about 20 μm active region. Such devices permit to distinguish ions of different energy, i.e. atomic numbers of different targets using RBS analysis and ion currents. Results demonstrated that the SiC energy resolution is comparable to that of Si, although worse. Si-barrier detector show higher energy resolution that permits to acquire significant RBS spectra using 1–6 MeV helium beam and SiC can be tailored designed to have a similar energy resolution. In this way, the surface metallization thickness must be reduced in order to reduce the ion energy loss and straggling in this passive absorber. The detection electronic line has been optimized to improve the impedance matching of the devices with the preamplifier, in order to improve the signal-to-noise ratio.

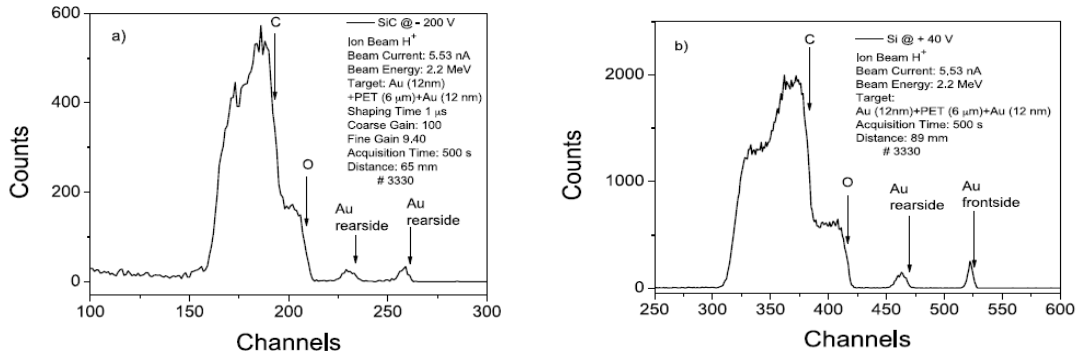

Fig.1: RBS comparison analysis obtained using 2.2 MeV proton energy, 5.5 nA current, with 500 s acquisition time, irradiating a thin polymeric (PET) film with 6 μm thickness, covered in front and back by 12 nm Au gold film acquired using SiC (a) and Si (b) detectors.

It is important to remind that SiC is superior to Si for some advantages, such as the higher energy gap that permits to be transparent to visible radiation and to be used to detect ions also in presence of high visible radiation, such as in plasmas ion emission or during ion irradiations of insulators, such as oxides and ceramics, emitting high fluorescent light intensity. SiC shows a lower reverse current, of about 10 pA at room temperature, two order magnitude lower with respect to Si, conferring higher sensitivity to the device. SiC is radiation resistant due to the higher bonding energy Si-C with respect to Si-Si, making it possible to use even in harsh conditions, such as plasmas and high temperatures, giving rise to a damage threshold due to absorbed doses much higher than that in silicon. Thus, SiC can be employed also to monitor on-line ion beams and lasers interacting with solids, to detect the radiations emitted from low and high temperature plasmas and to observe ion scattering processes from many materials. Their use can be optimized not only at low ion energy but also at high ion energy, increasing the active depth of the sensible detector region. Moreover their optimization can be performed also to detect UV, soft and hard X-rays and electrons generated by different sources, such as pulsed plasmas and particle beams.

References:

1) L. Torrisi, V. Havranek, M. Cutroneo, A. Mackova, L. Calcagno, A. Cannavò and A. Torrisi, "SiC detector for high helium energy spectroscopy", *NIM A* 903 (2018) 309–316.
2) A. Sciuto , G. D'Arrigo, S. Di Franco, M. Mazzillo , G. Franzò, L. Torrisi, and L. Calcagno, "4H-SiC Detector in High Photons and Ions Irradiation Regime", *IEEE Trans. on Electron Devices* 65(2), 2018, 599-604.
3) A. Torrisi, P.W. Wachulak, H. Fiedorowicz, and L.Torrisi, "SiC detectors for evaluation of laser-plasma dynamics employing gas-puff targets", *Nucl. Instr. and Meth. A*, 922 (2019) 250–256.

Fabrication of ion implanted integrated optical elements

Laboratory of Tandetron

István Bányász

Proposal ID

351

Report on project "Fabrication ion implanted integrated optical elements"

I. Bányász, Wigner Research Centre for Physics, Budapest, Hungary

I. Rajta, G.U.L. Nagy, Atomki, Institute for Nuclear Research, Debrecen, Hungary

V. Vosecek, V. Havránek, Nucl. Physics Inst., Řež, Czech Republic

1.
2. **Channel waveguides and Mach-Zehnder microinterferometers**

We planned to fabricate the channel waveguides and Mach-Zehnder interferometers with tapering, coupling gratings and with improved lateral confinement.

Experiments completed

The following structures have been fabricated:

1. Single channel waveguides in a KTP crystal, 5 MeV N^{3+} microbeam, fluence = $5\cdot10^{14}$ -$8\cdot10^{15}$ ions/cm^2.
2. Mach-Zehnder microinterferometres in a KTP crystal, 5 MeV N^{3+} microbeam, fluence = $5\cdot10^{14}$ -$8\cdot10^{15}$ ions/cm^2.
3. Single channel waveguides in a RTP crystal, 5 MeV N^{3+} microbeam, fluence = $5\cdot10^{14}$ -$8\cdot10^{15}$ ions/cm^2.
4. Mach-Zehnder microinterferometres in a RTP crystal, 5 MeV N^{3+} microbeam, fluence = five$\cdot10^{14}$ -$8\cdot10^{15}$ ions/cm^2.
5. Single channel waveguides in an Yb: KYW crystal, 5 MeV N^{3+} microbeam, fluence = $5\cdot10^{14}$ -$8\cdot10^{15}$ ions/cm^2.
6. Mach-Zehnder microinterferometres with grating couplers at both ends in an Yb: KYW crystal, 5 MeV N^{3+} microbeam, fluence = $5\cdot10^{14}$ -$8\cdot10^{15}$ ions/cm^2.
7. Single channel waveguides in a KTP crystal, 5 MeV N^{3+} microbeam, fluence = $5\cdot10^{14}$ -$8\cdot10^{15}$ ions/cm^2.
8. Single channel waveguides in a KTP crystal, 10.5 MeV N^{4+} microbeam, fluence = $1.25\cdot10^{14}$ - $4\cdot10^{15}$ ions/cm^2. Side-walled channel waveguides were also fabricated.
9. Mach-Zehnder microinterferometres in a KTP crystal, 10.eV N^{4+}microbeam, fluence = $6.25\cdot10^{13}$ -$4\cdot10^{15}$ ions/cm^2. Side-walled Mach-Zehnder microinterferometers were also fabricated.
10. Single channel waveguides in a RTP crystal, 10.5 MeV N^{4+} microbeam, fluence = $2.5\cdot10^{14}$ - $4\cdot10^{15}$ ions/cm^2. Side-walled channel waveguides were also fabricated.
11. Mach-Zehnder microinterferometres in a RTP crystal, 10.5 MeV N^{4+}microbeam, fluence = $1.25\cdot10^{14}$ - $2\cdot10^{15}$ ions/cm^2. Side-walled Mach-Zehnder microinterferometers were also fabricated.
12. Single channel waveguides in an Yb: KYW crystal, 10.5 MeV N^{3+} microbeam, fluence = $2\cdot10^{14}$ -$4\cdot10^{15}$ ions/cm^2. Side-walled channel waveguides and side-walled channel waveguides were also fabricated.

Tests completed

1. All the structures were measured with a confocal microscope to determine the profiles of the surface relief structures created.
2. Micro-Raman measurements, performed at the polished edges of the channel waveguides, revealed their depth profile.
3. Measurements showed that some of the as implanted single channel waveguides and Mach-Zehnder microinterferometres written in an Yb: KYW crystal had low propagation losses at a wavelength of 1450 nm.

3. **Microwells**

We tried to fabricate microwell arrays for biochemical sensors in a polymer (Zeonor) and a special glass (Gold Seal).

Experiments completed

1. **Zeonor Polymer**

Microwells were written in a Zeonor sample with 10.5 MeV N^{3+} microbeam, at fluences = $1\cdot10^{13}$ - $1\cdot10^{14}$ ions/cm^2.

2. **Gold Seal Glass**

Microwells were written in a Gold Seal sample with 10.5 MeV N^{3+} microbeam, at fluences = $1\cdot10^{14}$ - $4\cdot10^{14}$ ions/cm^2.

Tests completed

Preliminary AFM tests showed that some microwell groups in the Zeonor sample are good for use in sensors. The experiment has to be repeated with the same materials so that optimum geometrical parameters and fluences could be determined.

4. **Planar waveguides implanted with Ag ions**

Experiments completed

Planar optical waveguides were implanted in KTP and RTP crystals, using 11 MeV Ag^{3+} ions. Eight waveguides were fabricated in the two samples, with the fluences from $3\cdot10^{15}$ ions/cm^2 to $1\cdot10^{14}$ ions/cm^2.

Tests completed

Spectral ellipsometric tests of all the planar waveguides were performed. Even the raw ellipsometric spectra showed that the refractive index modulation induced in the samples by the Ag^{3+} ion implantation was rather low. Consequently, we plan to repeat this experiment with higher fluences up to $5\cdot10^{16}$ ions/cm^2.

Ion beam modification of carbon allotropes

Laboratory of Tandetron

Petr Malinsky

Proposal ID

352

Report regarding proposal “Ion beam modification of carbon allotropes”

P. Malinský, A. Macková. M. Cutroneo, V. Hnatowicz, K. Szökölová, M. Boháčová,
R. Böttger, J. Luxa, Z. Sofer

The proposal was denoted to the study of light and heavy ion irradiation of graphene oxide (GO) with the aim of GO reducing to the graphene like structure and simultaneously change its electrical properties. The GO is a carbon allotrope that is highly studied due to its excellent properties and potential in the field of nano-composites, solar cells, super-capacitors, micro- and nano-electronic [1–3]. GO is the single mono-molecular layer of graphene with various oxygen containing functionalities at edges and basal planes, due to the carbon atoms in the GO structure having a mixture of sp^2 and sp^3 hybridization. [2,4] Non-modified GO is an insulator due to the disruption in the sp^2 bonded graphitic structures and can be converted to semi- conductivity or conductivity state by changing the sp^2/sp^3 ratio. [5,6].

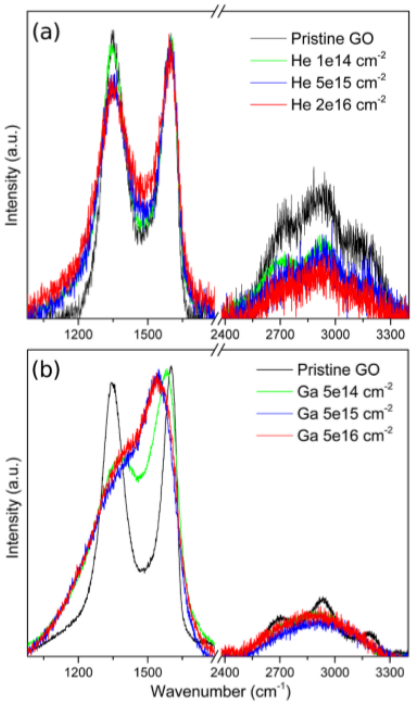

Figure 1: Raman spectra of GO film irradiated using various fluencies of 500 keV He ions (up) and Ga ions (down) compared to pristine GO film.

The GO foils were irradiated using He, H, Au and Ga ions with energies in the range from 500 keV to 5.1 MeV to the different fluencies and subsequently analyzed by ERDA, RBS, XPS, SEM and Raman spectroscopy to characterize the elemental composition, elemental depth profiles, subsurface chemical bonds and chemical composition modification as well as the surface morphology. The electrical properties of pristine and irradiated GO foils were measured by the standard two points method.

It can be concluded that the irradiation using heavy ions (Au, Ga) leads to strong changes in GO film structure and to the significant elemental composition modification, deoxygenation and dehydrogenation, which are connected to significant energy transfer from the heavy ions to the atoms in irradiated material via mostly non-elastic nuclear stopping. The irradiation using heavier ions causes the GO amorphization connected with disruption of the carbon bonds, with atom displacements, and also creation of new non-benzene carbon structures and vacancy types of defects. Contrary, irradiation using light ions (He, H), with dominant elastic electronic stopping, results in lower degree of GO deoxygenation and less pronounced structural changes when comparing with ions with higher mass. Moreover, the light ions irradiation leads to the formation of sp^2 graphene domains.

The irradiation with heavy as well as light ion species reduces the oxygen chemical bonds, generates new carbon bonds and causes the conductivity enhancement that is in accordance with observed compositional and structural modifications. The recovery of electrical conductivity is more pronounced for the light ions due the restoration of graphene like structure and can be concluded that GO irradiation using light ions provides relatively simple method of producing reduced graphene oxide with enhanced electrical conductivity.

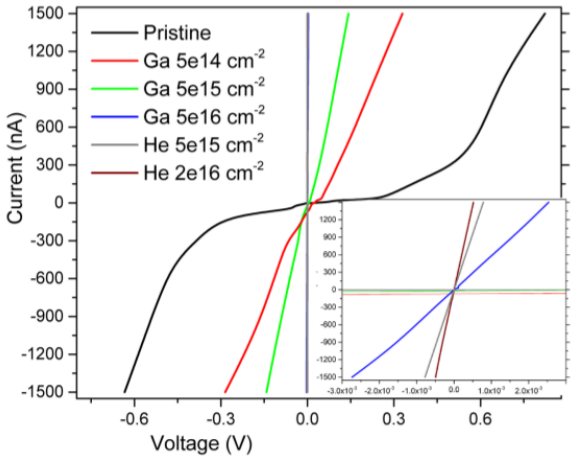

Figure 2: The I–V characteristic curves of pristine GO film and GO film irradiated with 500 keV He and Ga ions at various fluencies. The detailed I–Vcharacteristic for voltage range from $3.0x10^{-3}$ to $3.0x10^{-3}$ V is shown in inset figure

[1] P. Gulia, et all., AIP Conf. Proc. 2017, 1832, 140023.
[2] D. R. Dreyer, et all., Chem. Soc. Rev. 2010, 39, 228.
[3] V. Mazánek,et all., Nanoscale 2015, 7, 13646.
[4] O. C. Compton, Small 2010, 6, 11.
[5] S. Park, Carbon 2009, 50, 217.
[6] Ch. Punckt, et all., Appl. Phys. Lett. 2013, 102, 023114.

Structural and optical properties in yttria-stabilized zirconia modified by Si-implanted ions

Laboratory of Tandetron

Romana Mikšová

Proposal ID

357

Report regarding proposal "Structural and optical properties in yttria-stabilized zirconia modified by Si-implanted ions."

R. Mikšová, A. Macková, A. Jagerová, P. Malinský, Nucl. Physics Inst., Rez, Czech Republic
Z. Sofer, Department of Inorganic Chemistry, Institute of Chemical Technology, Prague, Czech Republic
V. Holý, Department of Condensed Matter, Faculty of Mathematics and Physics, Prague, Czech Republic
CEITEC at Masaryk University, Brno, Czech Republic

In our results, we observed Zr signal increase in the appropriate depth of Si implanted in yttria-stabilized zirconia (YSZ) with the enhanced ion fluence in Figure 1a simultaneously with the shift of the damaged region closer to the surface. YSZ implanted with medium-energy heavy ions exhibits the accumulation of damage with the increasing ion implantation fluence (see Figure 1b). The multi-damage step was shown.

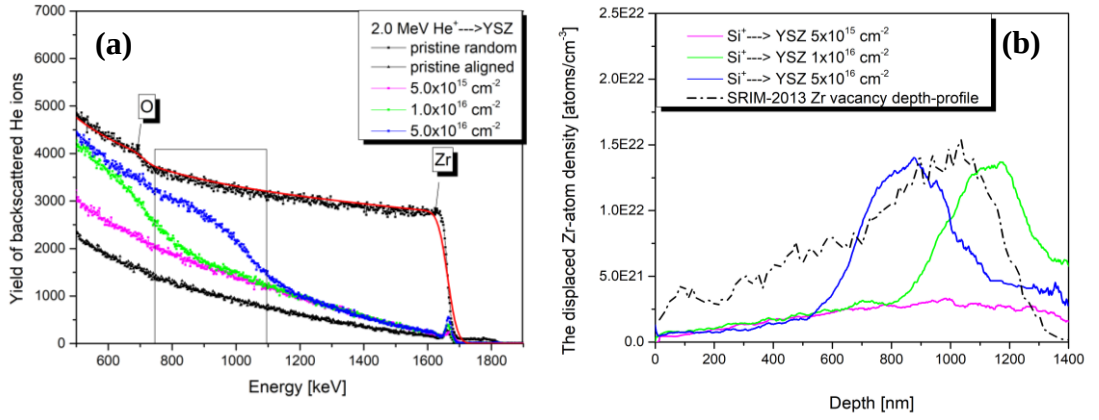

Figure 1. The RBS-C measurement of random and aligned spectra of pristine and implanted YSZ at ion fluence of 5×10^{15}-5×10^{16} cm^{-2} measured by energy 2.0 MeV (a) using He^+ ions. The depth profile of the displaced Zr-atom density in YSZ implanted by 2.0 MeV Si^+ ions at ion fluences of 5×10^{15}-5×10^{16} cm^{-2} extracted from the RBS-C spectra (b).

The XRD measurement indicates specific features as the positive vertical strain which is induced by the interstitial-type defects during ion implantation; the damaged layer is vertically expanded (Figure 2b). These facts agree with the RBS-C measurement where the axial-channel narrowing as a function of the increased ion-implantation fluence was observed. The axial-channel narrowing is a consequence of the gradually enhanced vertical expansion in YSZ (Figure 2a). The Raman spectroscopy confirms changes in the Raman spectra (peak broadening and peak shift) connected with the presence of the strain.

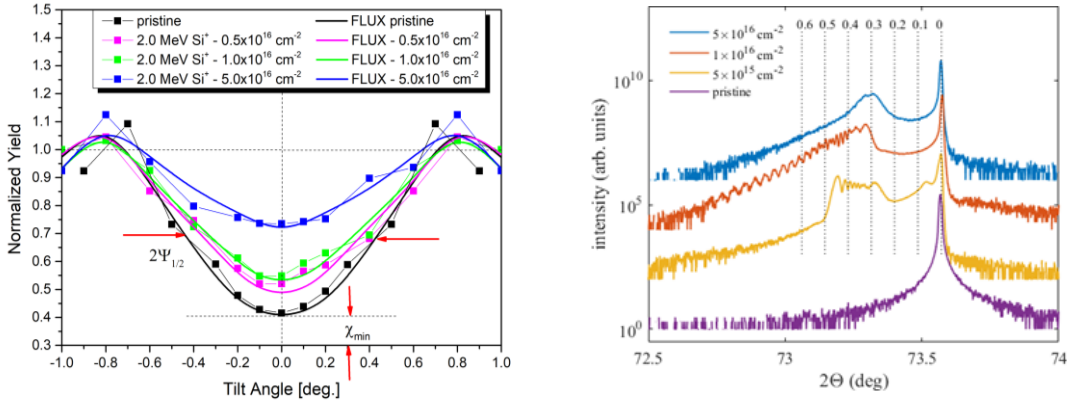

Figure 2. The angular (Zr sublattice) scans using 2.0 MeV He^+ ions penetrating (100) YSZ implanted with 2 MeV Si^+ ions at the fluences of 5×10^{15}-5×10^{16} cm^{-2}. Measured symmetric 2 Θ/Ω scans of a pristine sample and samples implanted with various doses (parameter of the curves).

The results were sent into NIMB.

Neutron scattering studies of nanostructured cemented carbides

Neutron Physics Laboratory - Neutron diffraction

Ahmet Bahadir Yildiz

Proposal ID

358

Experimental report

Proposal: Neutron scattering studies of nanostructured cemented carbides (ID: 358)

Ahmet Bahadir Yildiz, Peter Hedström: KTH Royal Institute of Technology, Stockholm

Vasyl Ryukhtin: Nuclear Physics Institute, Rez

Fine-grained cemented carbides are demanded in cutting applications requiring higher hardness. During our beamtime on the MAUD, we performed ex-situ V-SANS experiments for the investigation of WC grain growth in WC-Co-V_x system as a function of V addition.

V-SANS data were acquired at three different instrumental resolutions. To eliminate the magnetic scattering contribution, specimens were placed between two Neodymium magnets perpendicular to the neutron beam. The measured V-SANS data were corrected for electronic noise background using Cd, normalized by the transmission and scaled to absolute units dΣ/dΩ [cm^{-1}].

Fig. 1 shows the evolution of nuclear V-SANS intensities as a function of V addition. Upon V addition, the scattering intensity decreased at low-Q region, and increased at high-Q region. This development trend in scattering curves gave initial insight to the refinement in WC grain size. In order to calculate radius of gyration, R_g, we used Beaucage model [1] (solid lines in Fig. 1) and Kratky representation [2] (**Fig. 2**), i.e. dΣ/dΩ×Q^2 versus Q plots. Assuming spherical WC grains, the size of WC grains, D_{WC}, can be calculated by: $D_{WC} = 2 * \sqrt{\frac{5}{3}} R_g$

Fig. 3 shows the size evolution of WC grains together with the average grain size measured by EBSD. Consistency in the evolution trend was found in the grain size values determined by V-SANS and EBSD. Kratky plots gave significantly smaller D_{WC} than that of Beaucage model fit. Good agreement was found between D_{WC} values calculated by EBSD and V-SANS using Beaucage model and spherical grain assumption. Currently, we are working on a manuscript.

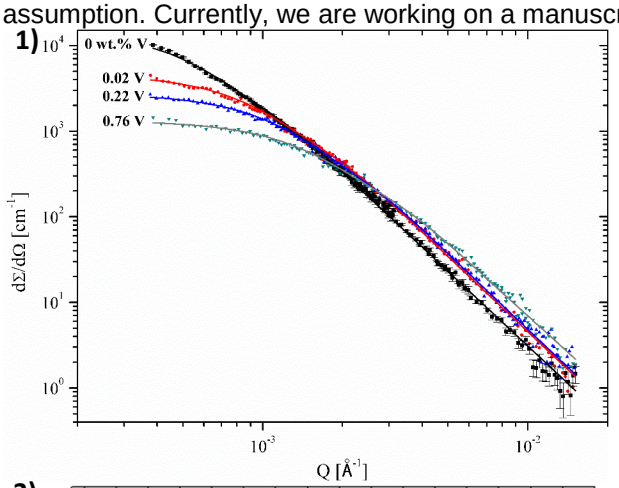

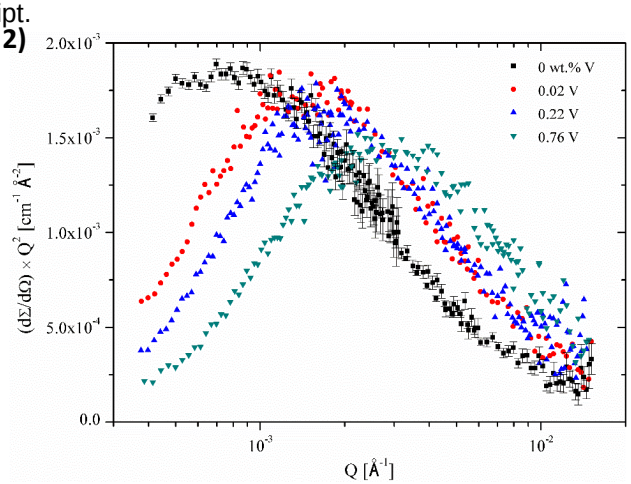

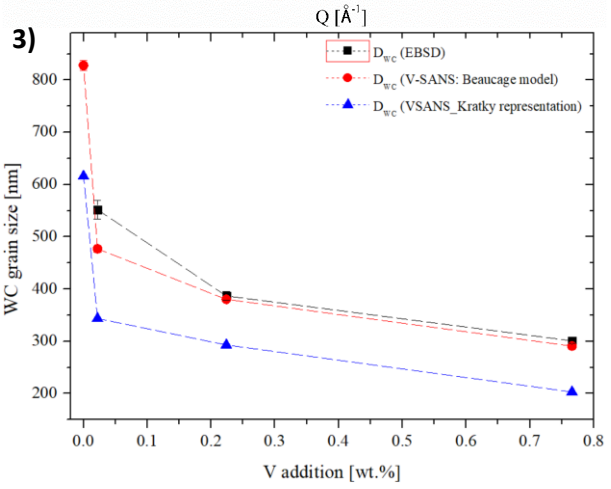

Figures The evolution of V-SANS curves log-log scale **(1)** and Kratky plots **(2)** as a function of V addition in liquid-phase sintered WC-Co-Vx (x=0 to 0.765 wt.% V) cemented carbides. The solid lines in Fig. 1 correspond to Beaucage model fit. The average WC grain size calculated for spherical WC grains plotted together with EBSD results **(3)**.

References

[1] G. Beaucage, J. Appl. Crystallogr. 28 (n.d.) 717–728.

[2] A. Deschamps, F. De Geuser, J. Appl. Crystallogr. 44 (2011) 343–352.

Simulation of alpha radiation-induced alterations in uraniferous fossil organic matter.

Laboratory of Tandetron

Vladimir Strunga

Proposal ID

360

Report regarding proposal "Simulation of alpha radiation-induced alterations in uraniferous fossil organic matter"

V. Strunga, V. Havránek, J. Mizera, Nucl. Physics Inst., Rez, Czech Republic
V. Goliáš, Inst. of Geochem., Mineral. and Min. Res., Charles University, Prague.

Polished sections of Baltic amber were prepared in two series of three samples each. Irradiation was carried on Tandetron accelerator at Nuclear Physics Institute, ASCR, Řež using a 4.8 MeV alpha-particle beam at three various doses, 5E13, 2E14, and 8E14 α/cm2, respectively. Samples were subjected to IR microspectroscopy (ATR-FTIR) afterward.

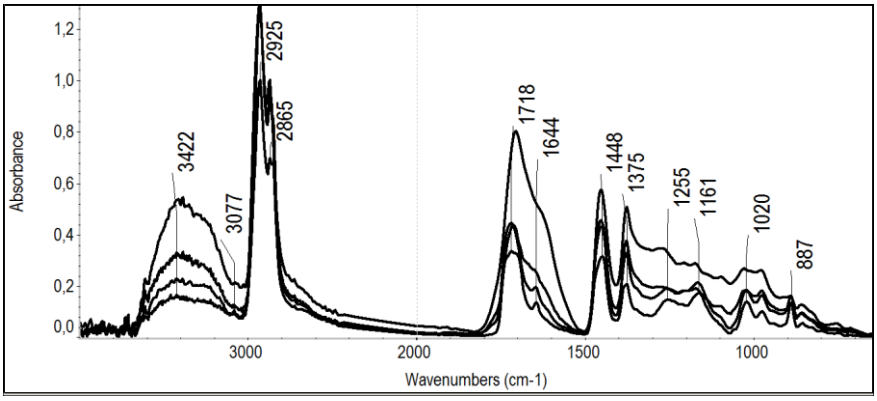

Fig. 1 Infrared spectra of analyzed ambers including non-irradiated sample (analysis by Vladimír Machovič).

Spectra exhibit broadening of O-H band at 3422 cm^{-1} as well as a decrease in double bond band intensities at 3100-3000, 1644 and 887 cm^{-1}. There is also distinguishable vanishing of the Baltic amber characteristic feature, so-called 'Baltic shoulder' assigned to the absorption of succinic acid ester bonds of polyester-like structures between 1255 and 1161 cm^{-1}.

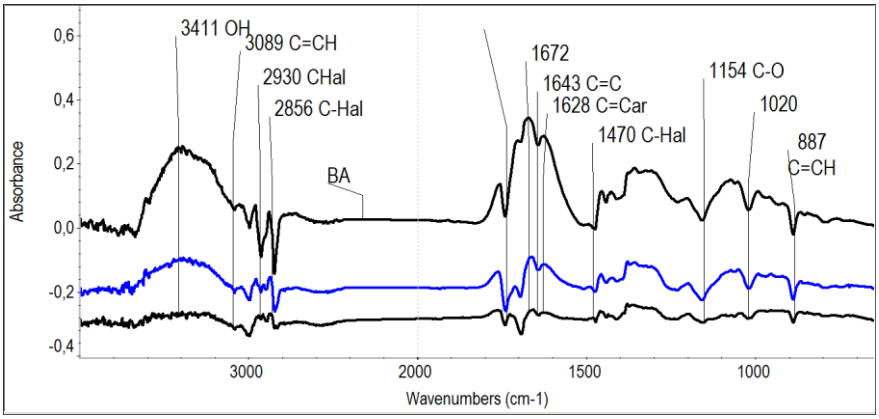

Fig. 2 Differential spectra obtained by subtraction of non-irradiated sample spectral values from irradiated ones (analysis by Vladimír Machovič).

Differential spectra reveal a considerable decrease of C-H band intensities at 2930, 2856, 1470 cm^{-1}, O-H band intensity increase at 3411 cm^{-1}, 1705 cm^{-1}, COOH band at 1672 cm^{-1}, highly conjugated C=O and aromatic C=C band at 1628 cm^{-1}.

Reference

Havelcová, M., Machovič, V., Linhartová, M. Lapčák, L., Přichystal, A., Dvořák, Z. (2016)
Vibrational spectroscopy with chromatographic methods in molecular analyses of Moravian amber samples (Czech Republic). Microchemical Journal, 128, 153-160.

SEE study of SoI radiation detection ASICs

Laboratory of Tandetron

Maria Marcisovska

Proposal ID

362

Report regarding proposal "SEE study of SoI radiation detection ASICs"

M. Marcisovska, A. Kabatova, L. Tomasek, M. Marcisovsky, V. Kafka, Czech Technical University in Prague

The measurements were focused on the study of single-event effect (SEE) response of microelectronic structures to highly ionizing radiation, which simulates the space environment. Radiation testing was focused mainly on the soft SEE, specifically on bit-flips. Bit-flip is the change of binary information in a memory cell, caused by charged particles impinging on this component. Our goal was to measure the cross section of bit-flips depending on the particle LET.

The highest probability of bit-flip occurrence is given by particles which deposit most of their energy in the chip's shift registers, which consist of D flip-flops. For the measurement purposes, a data pattern (OxAAAA) was periodically written into the shift register, which was followed by data readout (once per second) and comparison with the entering data pattern.

The ASIC under study was irradiated on air by a 1-MeV proton beam. The particle energy was determined by Geant4 and SRIM simulations. During the irradiation, an integral flux of 10^{12} protons/mm^2 was reached with no SEE being observed. Other used ions were $^{4}_{2}$He with the energy of 3,7 MeV and $^{12}_{6}$C with the energy of 17,5 MeV. This experiment was focused on the specific area of the detection chip containing the shift registers. This increased the probability of the SEE occurrence. An integral flux of 10^{12} ions/mm^2 was reached. The upper limit of the SEU cross section was inferred from the measurement as a function of particle LET.

In the following experiment, the detection chip was placed in the vacuum chamber and irradiated by carbon and oxygen ions. The simulations show, that the ideal initial ion energies used for this irradiation are 17 MeV and 24 MeV, respectively. Irradiation with the carbon ions resulted in the expected radiation damage. However, irradiation with the oxygen ions showed no observable radiation damage.

After that, a maximum ion energy was used in order for the ions to pass through the whole active area of the detector. These data were complemented by the data taken at JINR at the U400M cyclotron. This lead to extraction of the dependence of the bit-flip cross-section on the LET of the particle.

Radiation Hardness of Si Pixel Chips and Components for ALICE Inner Tracker System Upgrade Project

Laboratory of Cyclotron and Fast Neutron Generators

Filip Krizek

Proposal ID

365

Radiation Hardness of Si Pixel Chips and Components for ALICE Inner Tracker System Upgrade Project

In the CANAM 365 project, we tested radiation hardness of monolithic active pixel sensors which are going to be used in the upgraded Inner Tracking System (ITS) of the ALICE experiment. The sensors are called ALPIDEs and their radiation hardness was probed using a 30 MeV proton beam provided by the U-120M cyclotron. According to the Conceptual Design Report of the ITS project, the ALPIDE sensors must withstand 2.7 Mrad of Total ionization dose (TID) and 1.7 x 10^13 1 MeV n_eq/cm^2 of Nonionizing energy loss (NIEL) throughout the whole lifetime of the detector. Therefore in 2018, we continued in irradiations of two ALPIDE sensors which in previous years accumulated 1.8 Mrad and 1.4 Mrad TID and 1.8x10^13 and 1.4x10^13 1 MeV n_eq/cm^2 NIEL, respectively. Both ALPIDEs were irradiated on 12.1., 12.2., 28.3, 19.4, 17.5., 20.6., 16.7. and 10.10. At the end of the year, the chips accumulated 2.8 Mrad and 2.3 Mrad TID and 2.8x10^13 and 2.3x10^13 1 MeV n_eq/cm^2 NIEL, respectively. For both chips, we studied a mean charge threshold for signal detection in pixels and a mean temporal noise as a function of the accumulated TID. After retuning of the charge threshold in November 2017, both chips continue to exhibit significant annealing of their threshold levels after irradiations. The mean temporal noise, however, continues to grow and annealing shows a minor effect.

The interim results from these measurements were reported on several ITS upgrade characterization meetings, ALPIDE Qualification Task Force meetings (Work Package 5) on 24.1, 25.4. and 25.7.

The chip that got 2.8 Mrad was further brought to CERN where it was characterized using a 6 GeV/c pion beam from the CERN PS. The chip was characterized in terms of detection efficiency and fake hit rate. Important outcome from these measurements is that the highly irradiated sensor still meets requirements of the technical design report. Results from this measurement were presented at two international conferences:

[1] S. Kushpil et al. (ALICE collaboration), "Recent results from beam tests of the ALPIDE pixel chip for the upgrade of the ALICE Inner Tracker", 2018 IEEE Nuclear Science Symposium and Medical Imaging Conference, 10-17.11.2018, Sydney Australia.

[2] Valentina Raskina et al. (ALICE collaboration): "Characterization of silicon sensors for ALICE ITS upgrade", 18th Zimányi school and worshop, 3.-7.12. Budapest, Hungary.

A detailed description of the methodology of our measurements and of our irradiation setup that is being used for the tests of radiation hardness at the U-120M cyclotron facility were published in two papers:

[3] F. Křížek et al., Irradiation setup at the U-120M cyclotron facility, Nucl Instr. Meth. Phys. Res. A 894 (2018) 87-95.

[4] T. Matlocha and F. Křížek, Ultra-low intensity proton beams for radiation response related experiments at the U-120M cyclotron, Acta Polytechnica CTU Proceedings 14 (2018) 21-26.

Rb-83 for calibrations in the KATRIN continuing experiment

Laboratory of Cyclotron and Fast Neutron Generators

Drahoslav Venos

Proposal ID

366

Final report regarding proposal 366:

Rb-83 for calibration in the KATRIN, continuing experiment

D. Vénos

In the period 3.1.2018 - 20.12.2019 we have produced 83Rb in 5 irradiations at the cyclotron U-120M (the achieved activities of 340, 1500, 130, 1500 and 200 MBq) and in 1 irradiation at the cyclotron TR24 (the activity of 1600 MBq) using gas target filled with the natural krypton. For the irradiation at TR24 a newly designed gas target was used. The production rate at TR4, of 130 MBq of 83Rb per one hour irradiation time, was by a factor of 2.6 larger (mainly due to the larger current of the bombarding protons) in comparison with U-120M which has allowed us to reduce the irradiation time significantly.

From the 83Rb activities were prepared for the KATRIN project a 3 types of the 83Rb/83mKr sources of the monoenergetic electrons. The 2 sources were produced in NPI by vacuum evaporation of the 83Rb onto the amorphous graphite and Highly Oriented Pyrolytic Graphite (HOPG) substrates, respectively. Both these sources were transported to the Max Planck Institute for Physics (München). The sources were used for the test of the detector which is newly developed for KATRIN. Further, the 83Rb activity (deposited in the mass-separator tungsten furnace) was sent 2 times to Bonn University where altogether 4 83Rb/83mKr sources were prepared by the implantation of the 83Rb ions into the HOPG substrate. The 3 sources were installed at the Monitor Spectrometer which has watched the stability of the KATRIN High Voltage. One implanted source was installed at the Condensed Krypton Source (constructed at the Muenster University) which was used for the systematic measurement at the KATRIN. The main portions of the produced activity, 3 times of ~ 1.2 GBq of 83Rb, were deposited in the NPI into the zeolite beads. These 3 sources were regularly transported to KATRIN and installed into the Gaseous Krypton Source attached to the Windowless Gaseous Tritium Source (WGTS). The sources were used for the systematic studies of the WGTS plasma which has direct influence on the tritium beta spectra measured at KATRIN and subsequently on the deduced neutrino mass.

In the period 2018-2019 the KATRIN has started with the measurements of the neutrino mass gradually increasing the amount of the tritium in the WGTS. The first KATRIN limit on the neutrino mass, by factor of 2 better in comparison with the previous many years measurements, was obtained after 20 measurement days only. The result was published in the journal Physical Review Letters.

Articles in journals related to the use of Rb-83:

1) O. Dragoun, D. Vénos, ČS. Čas. Fyz. 69(2019)318, (in Czech).
2) M. Aker, K. Altenmüller, ... O. Dragoun, A. Kovalík, O. Lebeda, M. Ryšavý, D. Vénos, ... (KATRIN coll.), Phys. Rev. Lett. 123, 221802 (2019).
3) M. Aker, K. Altenmüller, ... O. Dragoun, A. Kovalík, O. Lebeda, M. Ryšavý, D. Vénos, ... (KATRIN coll.), arXiv:1909.06069v1 13 Sep 2019, submitted to Eur. Phys. J.
4) K. Altenmüller, M. Arenz, ... O. Dragoun, A. Kovalík, O. Lebeda, M. Ryšavý, D. Vénos, ... (KATRIN coll.), arXiv:1903.06452v2 18 Mar 2019.
5) A. Kovalík, A.Kh. Inoyatov, D. Vénos, M. Zbořil, O. Dragoun, D.V. Filosofov, L.L. Perevoshchikov, M. Ryšavý, Physics of Particles and Nuclei, 2019, Vol. 50 No. 6.
6) D. Vénos, J. Sentkerestiová, O. Dragoun, M. Slezák, M. Ryšavý, A. Špalek, 2018 JINST 13 T02012.
7) J. Sentkerestiová, O. Dragoun, O. Lebeda, M. Ryšavý, M. Sturm, D. Vénos, 2018 JINST 13 P04018.
8) M. Arenz, W.J. Baek, … O. Dragoun, A. Kovalík, O. Lebeda, M. Ryšavý, M. Slezák, M. Suchopár, J. Sentkerestiová, D. Vénos … (KATRIN coll.), 2018 JINST 13 P04020.
9) M. Arenz, W.J. Baek, … O. Dragoun, A. Kovalík, O. Lebeda, M. Ryšavý, M. Slezák, M. Suchopár, J. Sentkerestiová, D. Vénos … (KATRIN coll.), Eur. Phys. J. C (2018) 78:368.

Cross-section measurements of the 16O(n,tot) reaction in the neutron energy range 20-35 MeV

Laboratory of Cyclotron and Fast Neutron Generators

Mitja Majerle

Proposal ID

368

Final report regarding proposal 'Cross-section measurements of the ^{16}O(n,tot) reaction in the neutron energy range 20-35 MeV'

The series of transmission experiments with liquid oxygen was performed using Quasi-monoenergetic collimated beams of neutrons produced at U-120M cyclotron. The absolute values of the cross-section ^{nat}O(n,tot) were successfully extracted for four different energies ranging from 18 to 30 MeV. Overall uncertainties were evaluated for each measurement and regarding one sigma interval derived for normal distribution, the precision better than 3 % was achieved.

Exact results were presented at '2019 International Conference on Nuclear Data for Science and Technology' and subsequent paper named 'Total neutron cross-section extracted from transmission experiments with liquid oxygen using neutron energies from 18 to 34 MeV' is about to be published under 'EPJ Web of Conferences' in 2020.

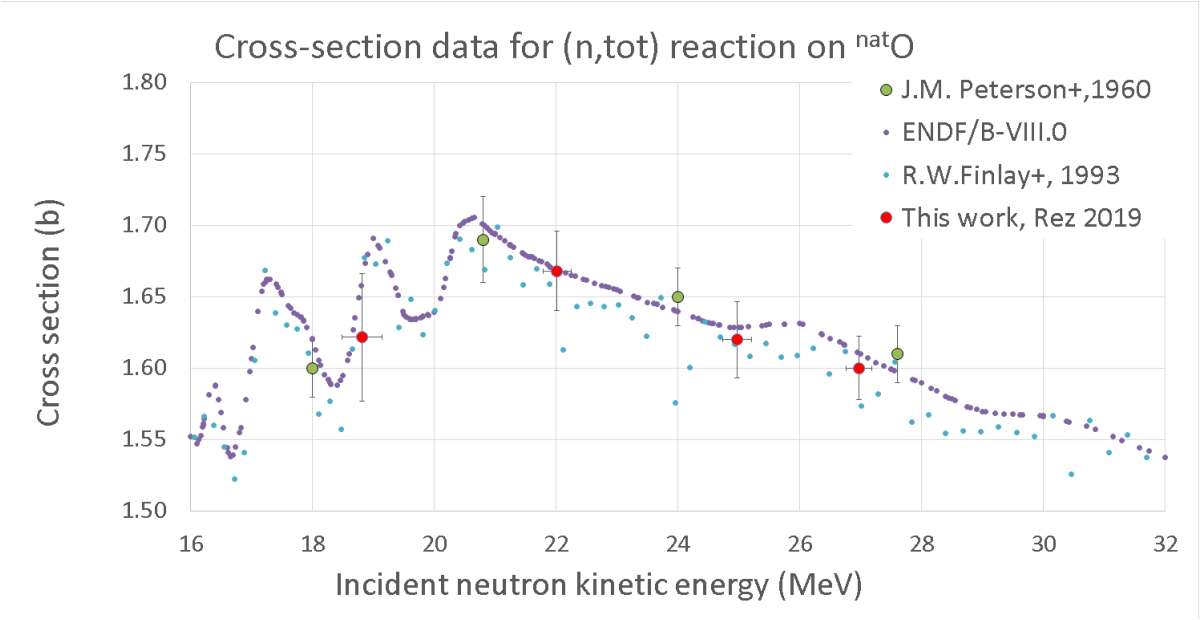

Figure 1. Present data of total neutron cross-section for ^{nat}O are shown (red points). For comparison data of Peterson [1] and Finlay [2] together with ENDF/B-VIII.0 evaluation for 16O(n, tot) reaction [3] are shown.

Present results (figure 1) should improve the correctness of data evaluations and contribute to all projects and researches where cross-section ^{nat}O(n,tot) is not a negligible factor. The Accelerator Driven Systems (ADS) and future fusion-based facilities are relevant examples.

References:

[1] J.M. Peterson, A. Bratenahl, J.P. Stoering, Phys. Rev.120, 521 (1960)

[2] R.W. Finlay et al., Neutron Total Cross Section Measurements at Intermediate Energy, in Nuclear Data for Science and Technology (1992), pp. 720–722, ISBN 978-3-642-58113-7

[3] D. Brown et al., Nuclear Data Sheets 148, 1 (2018), special Issue on Nuclear Reaction Data

Reactions of organometallic complexes relevant for the ion beam cancer therapy

Laboratory of Cyclotron and Fast Neutron Generators

Marie Davidkova

Proposal ID

370

Report regarding proposal "Reactions of organometallic complexes relevant for the ion beam cancer therapy"

J. Kočiček, D. Reimitz, Institute of Physical Chemistry of the CAS, Prague, Czech Republic
M. Davídková, Nuclear Physics Institute of the CAS, Řež, Czech Republic

An important challenge of radiation oncology is reduction of the side effects of the treatment. Such reduction can be achieved by effective targeting of tumors by radiation using the novel ion beam techniques or by lowering the dose delivered in concomitant chemo-radiotherapy. The main advantage of such treatments is in the so-called synergistic effect, which is the enhancement of the damage delivered to the tumor over the effect of the individual chemotherapy and radiotherapy treatments.
Experimental study is exploring combined effect of organometallic compounds and ionizing radiation. Performed experiments have been focused to cisdiamminedichloridoplatinum(II) (cisP or CDDP). When irradiating plasmid DNA in solution with free molecules by ^{60}Co gamma rays, no combined effect has been observed, indicating that the contribution to DNA damage caused by products of CDDP radiolysis is negligible in comparison to the damage caused by products of radiolysis of water. After binding to DNA, CDDP adducts with DNA strongly enhance the damage in a good agreement with the results of previous studies.
To reveal potential enhancement of DNA damage induction by radiation of different quality, Tris solutions containing pBR322 plasmids have been irradiated by 30 MeV protons. Different conformations of DNA plasmid corresponding to induced DNA single and double strand breaks have been analyzed using agarose gel electrophoresis. Relative proportion of relaxed form of pBR322 corresponding to single strand break yields as a function of absorbed dose is presented in Figure 1. No modifications of DNA damage induction have been detected in samples containing cisdiamminedichloridoplatinum(II) either for low (5 mM Tris) or high (200 mM Tris) radical scavenging conditions.

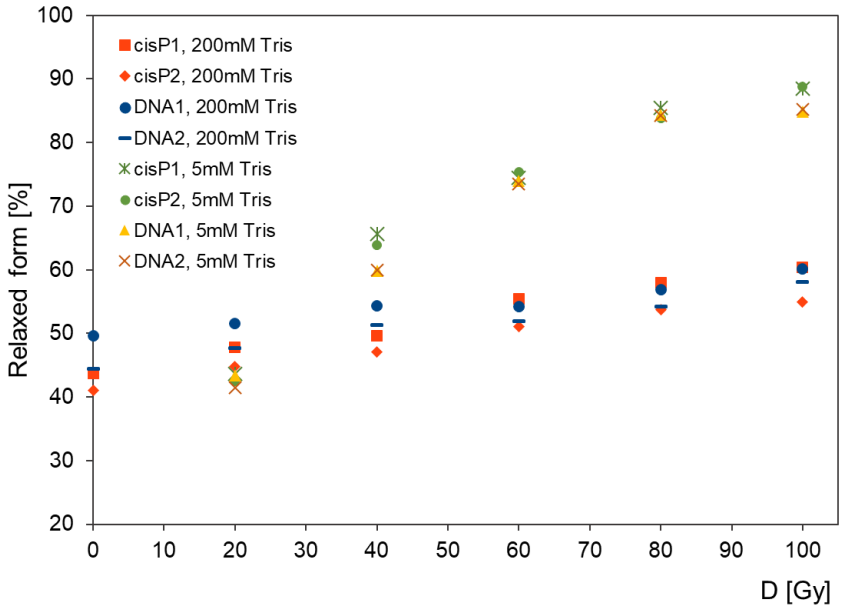

Figure 1: Proportion of relaxed form of pBR322 DNA plasmid irradiated by 30 MeV protons in presence or in absence of cisdiamminedichloridoplatinum(II) (cisP).

The work was supported by the Czech Science Foundation grant no. 16-10995Y.

Patterning and characterization of graphene oxide foil irradiated by Ion micro beam

Laboratory of Tandetron

Mariapompea Cutroneo

Proposal ID

371

Report

In the present proposal, the ion beam lithography technique has been used to write a line on graphene-oxide foil using the microbeam system and ions produced by a Tandetron accelerator. The depletion/enhancement of the GO components was precisely evaluated by irradiating progressively the foil and monitoring online its structural and compositional changes by RBS analysis (Figure 1).

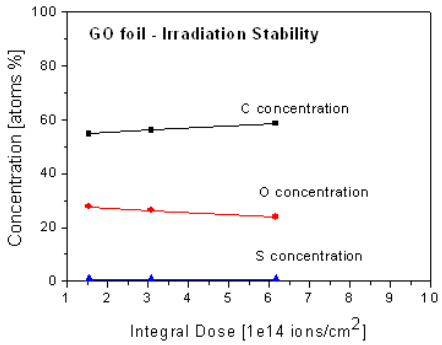

FIGURE 1. Changing of the C, O and S concentrations during the ion irradiation of the GO foils.

The agreement between RBS and SEM-EDX measurements suggests a relation between ion-irradiation fluence and oxygen reduction in GO foil and provides an essential clue that the reduction of GO can be a key factor for mobility enhancement (Figure 2).

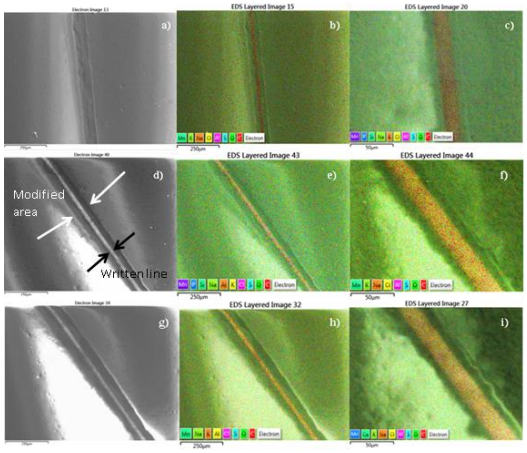

FIGURE 2. SEM images of a written line in GO foil magnified x296 and irradiated at $1.87 \cdot 10^{14}$ ions/cm^2 (a);SEM –EDX maps of the line magnified x1500 after the irradiation by$1.87 \cdot 10^{14}$ ions/cm^2 (b) and $3.75 \cdot 10^{14}$ ions/cm^2 c)

The published results reaffirm the potential of the ion- beam lithography as a promising technique for the processing of large-scale GO foil and the development of micrometric devices such as diodes and Schottky barriers as well as for other application. Further improvement of the quality along with the control of the ion-fluence irradiation to obtain the desired surface functionalisation are important challenges for the materials community but the oxidation/reduction processes need to be more fully understood to create and to tune the band gap in GO by varying the oxygen concentration.

Calibration of SSNTD for light ions

Laboratory of Tandetron

Antonino Cannavó

Proposal ID

382

Report regarding proposal "Calibration of SSNTD for light ions"

A. Cannavò, V. Havránek, J. Vacík

Solid State Nuclear Track Detectors (SSNTD) of the Poly-Allyl-Diglycol Carbonate type (PADC) have been exposed to proton, helium, carbon and copper ion beams provided by the Tandetron 4130 MC accelerator. After the chemical etching of the PADC sheets, consisting in a chemical bath of 2 hours at 70° in a 6.25 N NaOH solution, the etch-tracks have been studied by optical microscopy (OM). A typical OM picture is depicted in Fig.1a showing ion-etch pits as almost dark circles (due to the normal incidence of ions on the PADC surface) on a bright background. In particular such picture has been obtained after the irradiation with 5.8 MeV Cu ions.

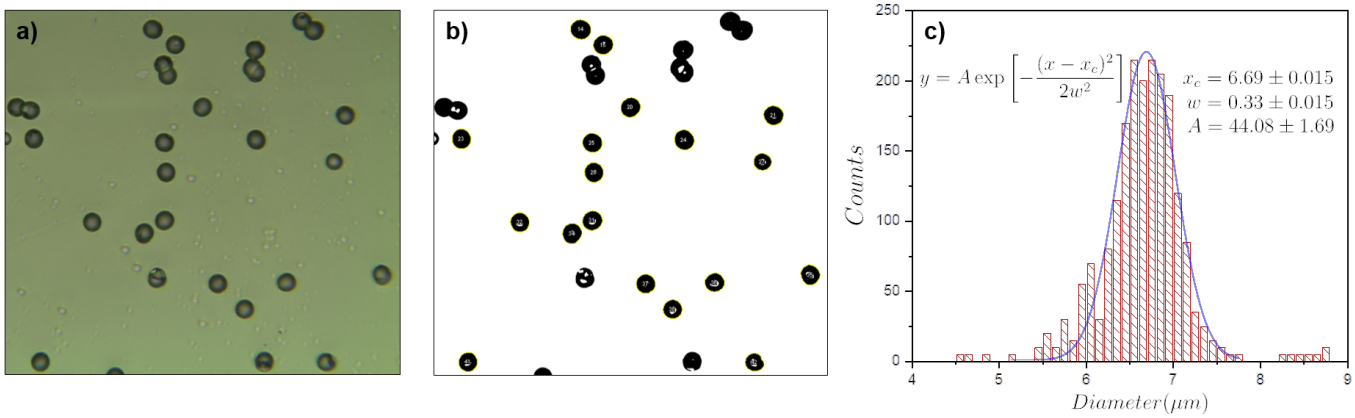

Figure 1: *A typical OM picture obtainable after the chemical etching of a PADC sheet exposed to ion beam a) and its tracks identification b); a typical result of diameter distribution of detected ion-etch pits c).*

OM pictures have been processed through a semi-automatic script developed under ImageJ software. This code identifies and classifies the tracks according to their shape and diameter. An example of its operation is illustrated in Fig.1b where it is shown how the script selects individual tracks (labeled with an increasing number) avoiding the overlapped tracks to be taken into account. The script's output, listing the geometrical characteristics of each detected etch-pits (area, minor and major axis), have been treated with a commercial data analysis software in order to get general information such as the diameter distribution (Fig.1c).

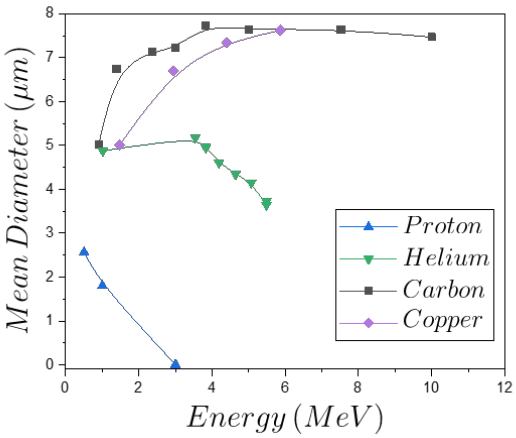

Figure 2: *Dependence of the tracks diameter on the ions energy.*

The results, summarized in the graph of Fig.2, put in evidence a strong correlation between the mean tracks' diameter and the different ions species: the heavier is the irradiating ions the larger is the diameter of the produced tracks, in agreement with previous data reported in literature, e.g., Ref.[1]. Another outcome arising from the Fig.2 is the influence of the ions energy on the tracks development. In the investigated energy ranges, except for the protons, the obtained trends seem not to be a monotonous functions of the ions energy, as also reported in Ref.[2]. This means that two different energies may have the same track diameter. Therefore, with the aim to use such materials for spectroscopic purposes, further analysis of the OM pictures are now being performed to study how the grayness of the ion-etch pits changes as proposed in Ref.[1].

Reference

[1] Malinowska A, Jaskóła M, Korman A, Szydłowski A, Malinowski K, Kuk M. Charged projectile spectrometry using solid-state nuclear track detector of the PM-355 type. Nukleonika. 2015; 60(3):591-6.
[2] El Ghazaly M. On alpha particle spectroscopy based on the over-etched track length in PADC (CR-39 detector). Radiation Effects and Defects in Solids. 2012; 167(6):421-7.

Study of crystal structure of the UO2/Fe3O4 thin films

Laboratory of Tandetron

Evgenia Chitrova

Proposal ID

386

Report regarding proposal "Study of crystal structure of the UO_2/Fe_3O_4 thin films"

Evgenia Chitrova, Ladislav Havela, Faculty of Mathematics and Physics, Charles University in Prague.

Exchange interaction through interface between a ferrimagnetic (F) magnetite Fe_3O_4 and an antiferromagnetic (AF) UO_2 results in the large magnetic exchange bias (EB) effect [1] (shift of the magnetic hysteresis loop along the field axis) (Fig.1). The magnetism of thin magnetic films and multilayers depends crucially on the structure and interface characteristics. In this work, we studied the crystal structure of Mg-capped UO_2/Fe_3O_4 bilayers (their chemical composition, layers thickness, etc.) deposited on the CaF_2 substrates.

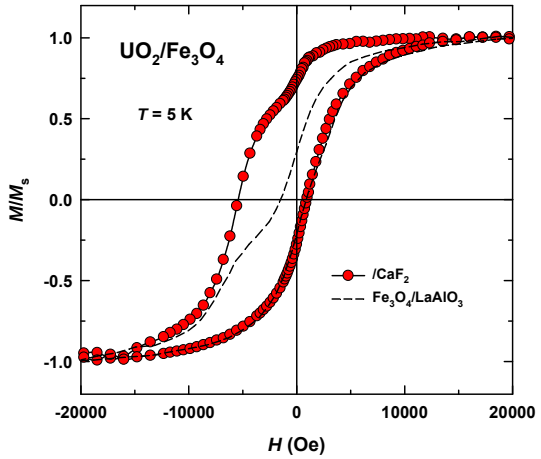

Fig. 1. The *H-M* magnetization loop at 5 K for the UO_2/Fe_3O_4 bilayer after field cooling in the 10 kOe field. The thicknesses for UO_2 and Fe_3O_4 in the bilayer are 280 and 250 Å. Data for a single layer of Fe_3O_4 (270 Å) (broken line) is shown for comparison.

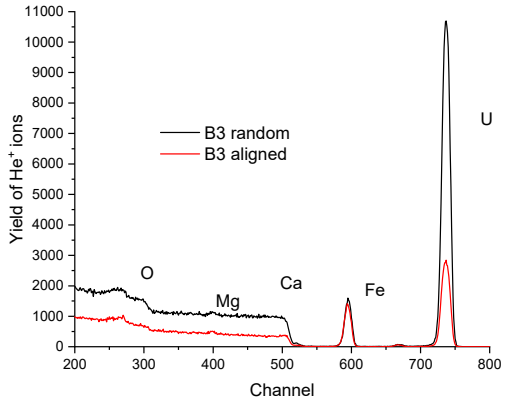

Fig. 2. Yield of back-scattered He ions for the incident beam along the [100] crystallographic direction of the UO_2 crystal (aligned) and at a random orientation (random) for the UO_2/Fe_3O_4 sample deposited on a CaF_2 substrate and capped with Mg.

Rutherford Back-Scattering Spectrometry (RBS) revealed a pronounced ion channelling in UO_2 thus showing low defect concentration in the layer. The spectra obtained showed well-separated signals from UO_2 and magnetite (Fig. 2). Nearly no channelling was observed for the Fe_3O_4 layer. This suggests that the layer is not single-crystalline and/or large concentration of defects/disorder is present in magnetite. The complimentary XRD study on the contrary revealed strong preferential orientation of Fe_3O_4 in the [111] out-of-plane direction and a presence of twins (similar to the results of Ref. 2). Presence of an impurity was found in the spectrum (does not exhibit channeling effect), which was attributed to some contamination of the Fe target by Zr. Since Zr is non-magnetic it should not influence the magnetic properties of magnetite. Thickness of magnetite found from RBS is close to that from the XRD study.

1) W. H. Meiklejohn and C. P. Bean, "New magnetic anisotropy", Phys. Rev. B, 102 1413, (1956).
2) E. A. Tereshina et al, Appl. Phys. Lett., 105 122405 (2014).

The role of water in the formation of the crystal structure of bacterial cellulose (BC)

Neutron Physics Laboratory - Neutron diffraction

Ruslan Smyslov

Proposal ID

387

Report regarding proposal “The role of water in the formation of the crystal structure of bacterial cellulose (BC)”

Ruslan Smyslov, Institute of Macromolecular Compounds of RAS, Saint Petersburg, Russia,
Aleksei Sokolov, Gennady Kopitsa, Anna Kulminskaya, Petersburg Nuclear Physics Institute named by B.P. Konstantinov of National Research Centre «Kurchatov Institute»,
Natalia Tsvigun, FSRC “Crystallography and Photonics” of RAS

Using the diffractometer MEREDIT, one registered a neutron diffraction pattern for deuterated bacterial cellulose (**dBC**). Nano-gel-film of bacterial cellulose (**BC**) was preliminary synthesized using *Komagataeibacter xylinus* strain in Research Center KI 'PNPI'. The specimens of the BC are obtained by the synthesis in the heavy water-based medium directly. The chemical gross formula of BC is $C_{12}H_{14}D_6O_{10}$.

The project is aimed to determine the availability for deuteration of hydroxyl groups in the crystalline lattice of BC during biosynthesis and self-assembly of supramolecular structure.

The Rietveld refinement was carried out using MAUD software [1] on the basis of the crystalline cell of cellulose Iα according the CIF data file 4114382 [2] from Crystallography Open Database [3]. In Figure 1, d-spacing is shown for a ND pattern of the dBC under investigation. Cellulose Iα has the triclinic crystal system with space group P1.

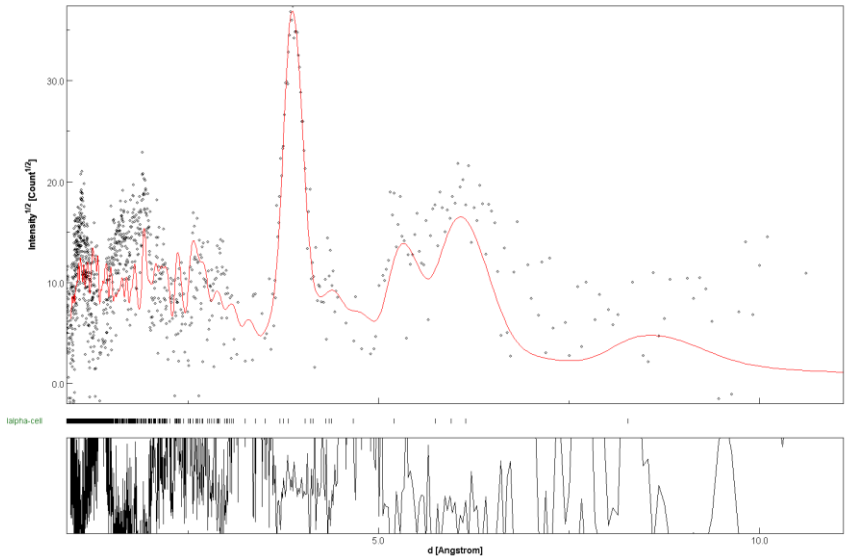

Figure 1. Neutron diffraction pattern for deuterated bacterial cellulose

Table 1. Comparison of Experimental Details

Data Collection		
diffractometer	MEREDIT	D19 [2]
Crystal Data		
chemical formula	$C_{12}H_{14}D_6O_{10}$	
cell setting, space group	triclinic, P1	triclinic, P1
a (Å)	10,270	10,400(6)
b (Å)	6,581	6,717(7)
c (Å)	5,925	5,962(6)
α (°)	81,052	80,37(5)
β (°)	118,39	118,08(5)
γ (°)	115,07	114,80(5)
V (Å^3)	318,6	333,3(6)
radiation type	neutron	neutron
λ (Å)	1,4600	1,3058

The preliminary comparing of the data obtained using the MEREDIT instruments and the D19 diffractometer [2] shows the concordance between them (Table 1). However, the cell for bacterial cellulose occurs less than for cellulose from the cell wall of the freshwater alga *Glaucocystis nostochinearum*.

References

[1] L. Lutterotti, Total pattern fitting for the combined size-strain-stress-texture determination in thin film diffraction, Nuclear Inst. and Methods in Physics Research, B, 268, 334-340, 2010.
[2] Nishiyama Y. at al. J. AM. CHEM. SOC. 2003, 125, 14300-14306 – DOI: 10.1021/ja037055w
[3] http://www.crystallography.net/cod/

RBS characterisation of ScN thin films compositions

Laboratory of Tandetron

Jan Lancok

Proposal ID

389

Joris More Chevaliet, RNDr. Anna Macková, Ph.D. **at all.**
Institute of Physics AV CR, Na Slovance 2, 182 21 Prague 8, Czech Republic, Nuclear Physics Institute of the ASCR, v. v. i., Rez 130, 250 68, Rez near Prague, Czech Republic

ScN/MgO

The ScN layers were deposited on double-side polished MgO (001) substrate in an ultra-high-vacuum (UHV) system (10-8 Pa) by DC reactive magnetron sputtering using a 99.9999% pure N2 discharge. The sample holder was electrically heated to reach the temperature of 700 °C. The working pressure of 3.5 Pa was used to sputter ScN from 99.9% pure Sc target of one inch diameter with a detectable contaminant of Ta at 0.1%. The thickness was measured using a Profilometer and confirmed by spectroscopic ellipsometry.

Experimental details

The measurements were performed by using the ion beam provided by the tandem accelerator, Tandetron MC 4130, at the Nuclear Physics Institute in Rez near Prague. A typical RBS spectrum you can see in Figure 2.

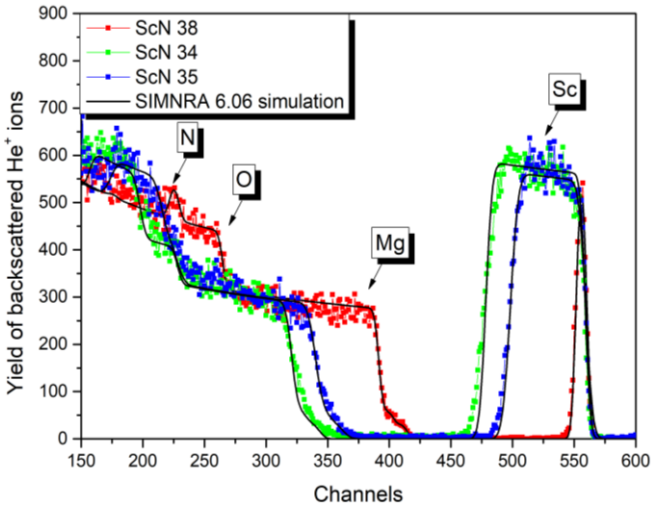

Figure 2: The RBS-C measurement of ScN/MgO measured by energy 2.0 MeV using He^+ ions.

Results

In Table 1 you can see in the second column name of the sample, third – thickness *t* from elipsomentry (in nm unit). In columns 4 and 5, there are *t* of each samples from RBS mentioned in 1e15at./cm^2 unit and nm (calculated at density 4.28(2) g/cm^3). In columns 6-10, there are concetrations of Sc, N, C Mg and O (mentioned in atomic percent) determined using the RBS method.

Table 1: Samples concentration

n.	sample	*t* (elipsometry) [nm]	*t* (RBS) [1e15at./cm^2]	*t* (RBS) [nm]	Sc [at.%]	N [at.%]	C [at.%]	Mg [at.%]	O [at.%]
1.	ScN 38	32	230	24	42.0	52.0	6.0	50	50
2.	ScN 34 700°C	248	2100	217	41.0	53.5	5.5	50	50
3.	ScN 35 700°C	190	1620	169	39.5	57.0	3.5	50	50

The received data will be used for publication concerning ScN thin films and compare with those obtained from EDX, XPS and XRF

Damage formation and optical activation of dopants in ZnO

Laboratory of Tandetron

Romana Mikšová

Proposal ID

393

Report regarding proposal "Damage formation and optical activation of dopants in ZnO."

A.Macková, P.Malinský, A.Jagerová, R.Mikšová, Nuclear Physics Institute of the Czech Academy of Sciences, v. v. i., Rez, Czech Republic
P.Nekvindová, J.Cajzl, Department of Inorganic Chemistry, Institute of Chemical Technology, Prague, Czech Republic
R. Böttger, S. Akhmadaliev, Institute of Ion Beam Physics and Materials Research, Helmholtz Zentrum Dresden-Rossendorf, Dresden, Germany

In our results, the structural modification of ZnO in c-plane (0001), a-plane (11–20) and m-plane (10-10) ZnO – implanted with Au^+ ions using the energy of 400 keV and fluences of 5×10^{14} and 1×10^{15} cm^{-2} and subsequently annealed at 600°C in O_2 was investigated. Deep structural damage grew with increased Au-ion fluence and Au did not exhibit strong out-diffusion from the depth to the surface during the post-implantation annealing. RBS measurements during ion implantation revealed more progressive deep-damage formation in the c- and m-planes than in the a-plane ZnO. Simultaneously, the smallest Zn sub-lattice disorder deduced from RBS/C measurements was observed in the a-plane ZnO. During post-implantation annealing, a slight structure recovery (about 4%) was observed in all orientations.

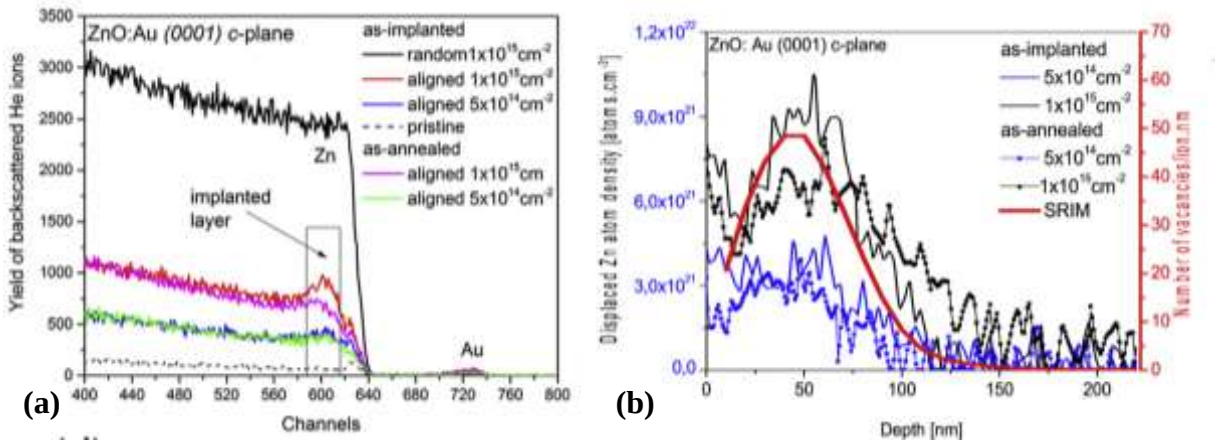

Figure 1. The RBS/channelling spectra for as-implanted and as-annealed samples: (a) c-plane ZnO. The region of interest appropriate to the ion-implanted layer is indicated in the black rectangle. The density profiles of the displaced Zn atom for various ion-implantation fluences determined from RBS/C spectra for as-implanted and as-annealed samples for the c-plane (b). SRIM-predicted Zn vacancy depth-distribution profiles are shown.

Raman spectroscopy confirmed the increasing structure disorder with the enhanced ion fluence for all as-implanted ZnO orientations and a partial reconstruction of the ZnO structure during annealing when the intensity of E_2 phonons was increased and that of longitudinal optical (LO) phonons was suppressed because of the disorder recovery. E_2(high) and E_1(LO) Raman phonon modes show a significant modification mainly in the m-plane.

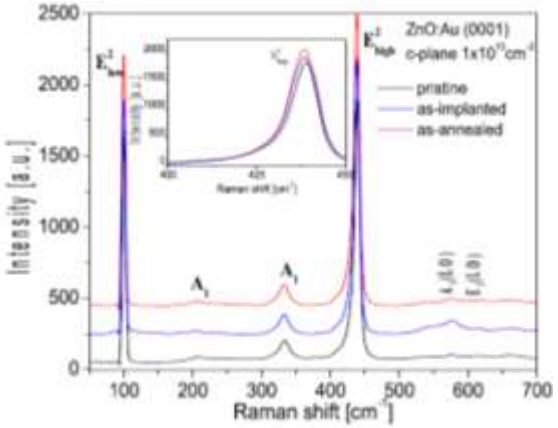

Figure 2. The Raman spectra of as-implanted (blue curves) and as-annealed (red curves) samples implanted using the ion-implantation fluence of 1×10^{15} cm−2 for c-plane ZnO.

All results from experiments on ZnO were published in Vacuum, Nuclear Instruments and Methods in Physics Research B and Journal of Alloys and Compounds.